

Electromagnetic waves under nonstationary conditions, the connection with parity-time symmetry and studies on resonant systems

Présentée le 7 juin 2021

Faculté des sciences et techniques de l'ingénieur
Laboratoire d'ingénierie des ondes
Programme doctoral en génie électrique

pour l'obtention du grade de Docteur ès Sciences

par

Theodoros KOUTSERIMPAS

Acceptée sur proposition du jury

Prof. A. Skrivervik Favre, présidente du jury
Prof. R. C. R. Fleury, directeur de thèse
Prof. J. Pendry, rapporteur
Prof. K. Makris, rapporteur
Prof. J. Mosig, rapporteur

Abstract

In this thesis, the electromagnetic wave propagation is studied in nonstationary–medium scenarios. The electromagnetic fields under material time–modulation are shown to conserve their momentum but not their energy. The mathematical foundations and analysis to treat wave propagation in time–Floquet media are given additionally to the related parametric amplification phenomena, which are mapped to the stability analysis of the corresponding hypergeometric equations. Assuming a time–variation of permittivity, permeability and conductivity the appropriate time–domain solutions are derived, based on an observation of the fields in the past. The formulation of a time–transitioning state matrix connects the unusual energy transitions of electromagnetic fields in time–varying media with the exceptional point theory, a theory strongly connected with parity–time symmetry. Consequently, the state–matrix approach of this thesis allows the analysis of the electromagnetic waves in terms of parity and time–reversal symmetries and signify parity–time symmetric wave–states without the presence of a spatially symmetric distribution of gain and loss, or any inhomogeneities and material periodicity. The parametric amplification phenomena of time–Floquet media and more precisely those that generate a Mathieu equation at the first momentum gap are theoretically studied and numerically compared with simulations using FDTD and connected with the parity–time scattering conventional characteristics. In the last part of this thesis, studies regarding resonant acoustic and electromagnetic systems are exhibited. The theoretical foundation to treat both acoustic and electromagnetic resonant phenomena is given based on the coupled mode theory and the appropriate Hilbert space. Two examples of interest are shown leveraging the time–dynamics of a temporal resonant system. The first example is related to the design of an artificial resonant acoustic lattice with

the appropriate time–modulation leading to an effective zero index of refraction. The second example is related to resonant systems with temporal coupling and the possibility to induce nonreciprocal gain by leveraging the frequency conversion occurring in parametric systems. This thesis enriches the literature and the theoretical bases for dynamical wave systems and provides an insight on the broad capabilities of time–varying systems in electromagnetics, optics and acoustics. It may be used as a guidance to realize wave devices that amplify and actively filter wave signals for many future applications in lasing, sensing, signal amplifying, energy transferring and imaging.

Keywords: electromagnetic propagation, time-varying systems, parametric amplification, exceptional points, parity-time symmetry, resonant devices.

Résumé

Dans cette thèse, la propagation des ondes électromagnétiques est étudiée dans des scénarios de milieu non stationnaire. On montre que les champs électromagnétiques soumis à une modulation temporelle matérielle conservent leur impulsion mais pas leur énergie. Les fondements mathématiques pour traiter la propagation des ondes dans les milieux de Floquet temporels sont donnés, et les phénomènes d'amplification paramétrique associés sont analysés à la lumière des régimes de stabilité des équations hypergéométriques correspondantes. En supposant une variation temporelle de la permittivité, de la perméabilité et de la conductivité, les solutions appropriées en domaine temporel sont obtenues sur la base d'une observation des champs dans le passé. La formulation d'une matrice d'état de la transition temporelle décrit les transitions d'énergie inhabituelles que subissent les champs électromagnétiques dans des milieux variant dans le temps. Elle est étudiée avec la théorie des points exceptionnels, une théorie fortement liée à la symétrie parité-temps. Par conséquent, l'approche matrice d'état de cette thèse permet la description des ondes électromagnétiques en terme de symétries de parité et d'inversion temporelle, et signifie que des états d'onde symétriques parité-temps peuvent être obtenus sans la présence d'une distribution spatialement symétrique du gain et de la perte, ou même d'inhomogénéités ou périodicité des matériaux. Les phénomènes d'amplification paramétrique des milieux temps-Floquet et plus précisément ceux qui génèrent une équation de Mathieu sont théoriquement étudiés et comparés numériquement à des simulations utilisant FDTD et reliés aux caractéristiques conventionnelles de diffusion parité-temps. Dans la dernière partie de cette thèse, des études sur les systèmes acoustiques et électromagnétiques résonants sont présentées. La base théorique pour traiter les phénomènes de résonance acoustiques et électromagnétiques est donnée

sur la base de la théorie des modes couplés et de l'espace de Hilbert approprié. Deux exemples intéressants sont présentés, tirant parti de la dynamique temporelle d'un système résonnant temporel. Le premier exemple est lié à la conception d'un réseau acoustique résonnant artificiel avec la modulation de temps appropriée, conduisant à un indice de réfraction effectif nul. Le deuxième exemple concerne les systèmes résonants avec couplage temporel et la possibilité d'induire un gain non réciproque en tirant parti de la conversion de fréquence se produisant dans les systèmes paramétriques. Cette thèse enrichit la littérature et les bases théoriques des systèmes d'ondes dynamiques et démontre de vastes possibilités pour manipuler les ondes avec des systèmes artificiels variant dans le temps en électromagnétique, optique et acoustique. Ce travail peut être utilisée comme guide pour réaliser des dispositifs amplifiant les ondes et filtrant activement les signaux ondulatoires pour de nombreux applications pour les amplificateurs, le transfert d'énergie et l'imagerie.

mots clés: propagation électromagnétique, systèmes variant dans le temps, amplification paramétrique, points exceptionnels, système à symétrie parité-temps, dispositifs résonants.

I would like to thank Prof. R. Fleury for offering me a PhD position in his group and a flexible as well as a free—spirited research environment. I would also like to express my appreciation to the members of my PhD jury committee: Prof. Anja Skrivervik, Prof. Emeritus Juan Mosig, Prof. Sir John Pendry and Prof. Konstantinos Makris.

I am grateful for the support of my family, friends, professors, mentors and colleagues during my PhD studies.

Theodoros T. Koutserimpas
Lausanne, March 2021.

To my family,
in appreciation for their love and encouragement.

«Με λογισμό και μ' όνειρο...»

Διονύσιος Σολωμός.

Table of Contents

1. Introduction	1
2. Electromagnetic waves under time–varying media	3
2.1 The laws of reflection and transmission	3
2.2 Poynting and momentum conservation theorem	8
2.3 Potentials, Lorentz gauge and Hertz vector	10
2.4 Integral form of field solutions under a current excitation and matched time–variations	11
2.5 Electromagnetic modes in the absence of sources	14
2.6 Temporal material discontinuities: Scattering matrix formulation.....	19
2.7 Electromagnetic modes under time–Floquet media.....	22
2.8 Parametric amplification at the momentum gaps	28
3. \mathcal{PT} –symmetry and time–variant media	35
3.1 Introduction to \mathcal{PT} –symmetry	35
3.2 Exceptional points and operator symmetries under time–variance.....	38
3.3 \mathcal{PT} –symmetric scattering of a time–Floquet slab: Parametric amplification and bidirectional invisibility	44
4. Studies on time–variant resonant systems.....	61
4.1 Coupled–mode theory	61
4.2 The mathematical foundations of the Hamiltonian formalism under time–periodicity	67
4.3 Zero refractive index in time–Floquet acoustic metamaterials	70
4.4 Induced gain and frequency conversion in time–varying coupling of a two–by–two Hamiltonian system	81
5. Conclusion	93
 Appendix A: Nonstationary and inhomogeneous medium equations	 95

Appendix B: Dipole polarizability under nonstationary conditions.....	97
Appendix C: Induced acoustic resonance by an active feedback control system.....	105
References	120
Author's CV	124

Chapter 1:

Introduction

Electromagnetic wave propagation in inhomogeneous media has been studied extensively and has been implemented in a plethora of applications from the optical to the microwave frequency regimes. The excited waves scatter at inhomogeneous obstacles, resulting in the creation of reflected and transmitted ones. The influence of complex geometries and materials has been utilized over the years to radiate, focus, guide, filter and confine waves. If the inhomogeneity is lossless the overall energy is conserved, the frequency ω remains invariant, whereas the wavenumber (momentum of the wave) k is altered [1,2].

In recent years, there has been an emergent scientific interest to investigate propagation in complex media. In particular, devices with material loss and gain can exhibit propagating modes under specific symmetry conditions (the paraxial equation of diffraction has to commute with the parity–time (PT) operator) [3–5]. Such symmetries are met in non–Hermitian optical devices, where material gain and loss are symmetrically distributed, $\varepsilon(\mathbf{r}) = \varepsilon^*(-\mathbf{r})$ and may be of use in lasers and sensors, since they exhibit amplification and unidirectional characteristics [6–9].

A seemingly different subject of interest in wave physics is the study of electromagnetic fields under nonstationary conditions [10–15]. In such case, the material parameters such as the permittivity and the permeability are considered time–dependent, an effective consequence of a strong pump by an

external agent. Contradictory to the stationary inhomogeneous case, waves under a homogeneous nonstationary medium do not conserve their energy, the frequency ω is variant and the wavenumber (momentum of the wave) k is conserved [16].

One may ask the question whether wave propagation under nonstationary media can be connected with \mathcal{PT} – symmetry and whether a distribution of gain and loss could be substituted by the parametric amplification phenomena in such momentum invariant systems. Answering this question is the main topic of this thesis and is analyzed in chapters 2, 3. The fourth chapter reports the author’s independent and concurrent studies related to the modelling of resonant systems under non–stationary conditions.

In more detail, the second chapter contains of a variety of general cases of time–dependent wave media and the appropriate mathematical modelling for general non–dispersive time–aperiodic and periodic cases [17,18].

In the third chapter, the non–trivial connection between \mathcal{PT} – symmetry and electromagnetic waves under time–varying media is shown, providing a new physical insight to such wave problems, connecting the energy transitions with the exceptional point theory and substituting material gain and loss with an out–of–phase modulation and parametric amplification [17,19].

The fourth chapter, which is a stand–alone study, includes the author’s concurrent research on periodically driven time–variant resonant systems. The mathematical formalism and foundations of resonant systems are described, while using the temporal coupled–mode theory, the Floquet–Bloch ansatz and the stroboscopic analysis for the band structure studies [20]. In conclusion of the fourth chapter, two examples of resonant systems are proposed. The first explores the possibility to induce effective zero–index of refraction to a resonant time-varying acoustic lattice, while the second to induce frequency conversion and parametric amplification [21,22].

Chapter 2:

Electromagnetic waves under time-varying media

In this chapter, the formulation and the mathematical modelling of waves under time-varying media is provided. As an introduction to this chapter, a comparison between Fresnel's [2] and Morgenthaler's reflection and transmission coefficients [16] is considered. The Poynting and the momentum conservation theorems as well as the potentials based on the Lorentz gauge and the electric Hertz vector are revised taking into account the particularities of time-variant media [17]. The integral solutions from current sources are shown [23] and the generic free-source solutions including a time-variation of the conductivity are derived [17]. In particular, wave propagation under time-periodic media is taken into account and its wave solutions according to the Floquet-Bloch ansatz are mapped with the analysis of the hypergeometric Hill's equation [18,24]. This chapter, aside from introducing a review of past literature is also based on the author's published work [17,18].

2.1 The laws of reflection and transmission

The laws of reflection and transmission are considered fundamental in electromagnetic theory. They are the physical foundation for the design of microwave and optical devices, from transmission lines to optical gratings. For this reason, we start by reformulating them in context of temporal material changes, giving an interesting twist to the usual spatial boundary problem. We consider two representative cases: the widely known spatial boundary and a

temporal one and provide the wave–phenomena equivalences between the spatial and the temporal material discontinuities and their reflection and transmission coefficients. Starting with Maxwell’s equations, the electromagnetic equations regarding the electric field \mathbf{E} , the magnetic field \mathbf{H} , the electric displacement \mathbf{D} and the magnetic induction \mathbf{B} , are:

$$\begin{aligned}\nabla \times \mathbf{E} &= -\partial_t \mathbf{B}, & \nabla \times \mathbf{H} &= \partial_t \mathbf{D} + \mathbf{J}, \\ \nabla \cdot \mathbf{D} &= \rho, & \nabla \cdot \mathbf{B} &= 0.\end{aligned}\tag{1}$$

The constitutive relations are: $\mathbf{D} = \varepsilon \mathbf{E}$, $\mathbf{B} = \mu \mathbf{H}$, where ε is the permittivity and μ is the permeability. Let us assume a source–free region, where charges and currents are absent ($\rho = 0$, $\mathbf{J} = 0$) and the space is separated by two semi–planes with different ε, μ as shown in Fig. 1, along the z –direction. A direct observation of the electromagnetic field equations is that the perpendicular field components of \mathbf{D} , \mathbf{B} and the components of \mathbf{E} , \mathbf{H} alongside the boundary are continuous despite the spatial discontinuity. Assuming a plane wave incident field E_i that can have either an electric field (TE mode) or a magnetic field (TM mode) at the y direction or a linear combination of both and an angle of incidence to the boundary equal with θ_1 (as shown in Fig. 1) is excited with a frequency ω . Then the Fresnel’s coefficients are [2]:

$$r_{TE} = \frac{E_r}{E_i} = \frac{\sqrt{\frac{\mu_2}{\varepsilon_2}} \cos \theta_1 - \sqrt{\frac{\mu_1}{\varepsilon_1}} \cos \theta_2}{\sqrt{\frac{\mu_2}{\varepsilon_2}} \cos \theta_1 + \sqrt{\frac{\mu_1}{\varepsilon_1}} \cos \theta_2},\tag{2}$$

$$\tau_{TE} = \frac{E_t}{E_i} = \frac{2\sqrt{\frac{\mu_2}{\varepsilon_2}} \cos \theta_1}{\sqrt{\frac{\mu_2}{\varepsilon_2}} \cos \theta_1 + \sqrt{\frac{\mu_1}{\varepsilon_1}} \cos \theta_2}, \quad (3)$$

$$r_{TM} = \frac{E_r}{E_i} = \frac{\sqrt{\frac{\mu_1}{\varepsilon_1}} \cos \theta_1 - \sqrt{\frac{\mu_2}{\varepsilon_2}} \cos \theta_2}{\sqrt{\frac{\mu_1}{\varepsilon_1}} \cos \theta_1 + \sqrt{\frac{\mu_2}{\varepsilon_2}} \cos \theta_2}, \quad (4)$$

$$\tau_{TM} = \frac{E_t}{E_i} = \frac{2\sqrt{\frac{\mu_2}{\varepsilon_2}} \cos \theta_1}{\sqrt{\frac{\mu_1}{\varepsilon_1}} \cos \theta_1 + \sqrt{\frac{\mu_2}{\varepsilon_2}} \cos \theta_2}, \quad (5)$$

where $\sin \theta_2 = \sqrt{\frac{\varepsilon_1 \mu_1}{\varepsilon_2 \mu_2}} \sin \theta_1$, the angle of reflection is the same with θ_1 , the momentum at the direction along the boundary and the total energy are conserved ($|r|^2 + |\tau|^2 = 1$). The total momentum is variant. The perpendicular to the interface direction has to change. This is due to the fact that the norm of the wavevector is fixed by the medium's parameters and the frequency excitation, as dictated by the satisfied wave equation. This is a consequence of the corresponding allowed wave solutions at the two regions. The existence of this mismatch is due to the discontinuity of the wave momentum at the perpendicular to the interface direction, (for the presented example in Fig. 1 the z -direction). A spatial boundary breaks thus the spatial translation symmetry of the propagating photon.

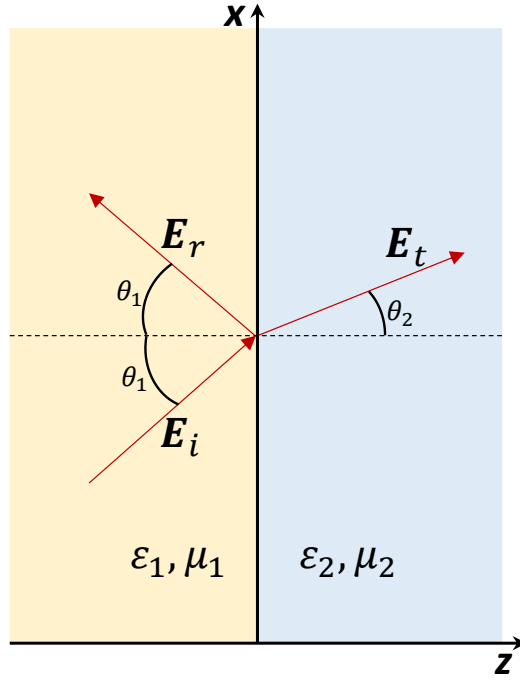


Figure 1: Diagram of the reflection and transmission of an incident wave incident with an angle on an interface.

Let us now substitute the spatial boundary with a temporal one. This means that we substitute z with t . If we assume again a plane wave the spatial dependence can be truncated to one spatial coordinate (y) as shown in Fig. 2. The values of the incident angle in the ty plane are forced by the wave equations before and after the temporal jump and the relation: $\tan \alpha_2 = \sqrt{\frac{\epsilon_1 \mu_1}{\epsilon_2 \mu_2}} \tan \alpha_1$. The angles of transmission and reflection are the same (since they satisfy the same wave equation). The plane wave under the temporal jump exhibits an adiabatic wavelength conversion (a term used in [25]), because it changes its frequency according to the plane-wave free-space dispersion relation, while k remains unchanged (the role of the source is to enforce the wavenumber k). At the boundary we require the temporal continuity of the electric displacement and magnetic induction fields

as directly observed by Maxwell's equations and can thus easily derive the Morgenthaler's coefficients as in [16]:

$$r = \frac{E_r}{E_i} = \frac{1}{2} \left[\frac{\varepsilon_1}{\varepsilon_2} - \sqrt{\frac{\mu_1 \varepsilon_1}{\mu_2 \varepsilon_2}} \right], \quad (6)$$

$$\tau = \frac{E_t}{E_i} = \frac{1}{2} \left[\frac{\varepsilon_1}{\varepsilon_2} + \sqrt{\frac{\mu_1 \varepsilon_1}{\mu_2 \varepsilon_2}} \right]. \quad (7)$$

There is no need to analyze the problem in terms of TE or TM modes since it is one-dimensional (the spatial dependence of the plane wave can be truncated in only one direction). The temporal reflection cannot travel in the left semi-plane, since causality forbids the reflected wave to travel into the past. Energy is not conserved: $|r|^2 + |\tau|^2 \neq 1$, because the time reflection and transmission are required to keep constant the total number of photons (see also next subsection about the Poynting theorem). Analogously with the spatial boundaries, a temporal jump of the wave-medium breaks the temporal translation symmetry of the photons. In the special case of a preservation of the wave impedance $\eta = \sqrt{\mu/\varepsilon}$ the plane wave does not exhibit reflection (the temporal boundary is matched) but still its frequency is altered.

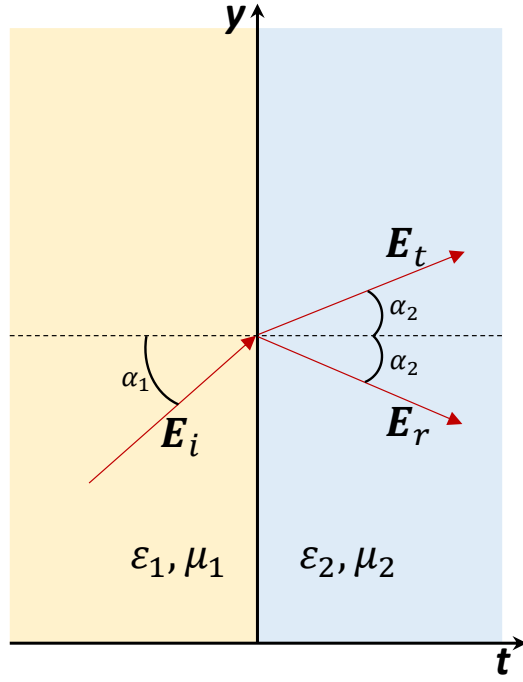


Figure 2: Diagram of the temporal reflection and transmission process. The propagation of the reflected wave is only allowed in the right semi-plane.

2.2 Poynting and momentum conservation theorems

The conservation of energy takes the form [26]:

$$\frac{\partial W}{\partial t} + \nabla \cdot \mathbf{S} = -p, \quad (8)$$

where W is the total stored energy, \mathbf{S} the Poynting vector and p is the power supplied by an external agent. In the case of a time-varying medium (including a time-varying conductivity), taking into account Maxwell's equation we derive [17]:

$$W = \frac{\varepsilon(t)}{2} |\mathbf{E}|^2 + \frac{\mu(t)}{2} |\mathbf{H}|^2, \quad (9)$$

$$\mathbf{S} = \mathbf{E} \times \mathbf{H}, \quad (10)$$

$$p = \mathbf{E} \cdot (\mathbf{J} + \sigma(t)\mathbf{E}) + \frac{1}{2} \frac{d\mu(t)}{dt} |\mathbf{H}|^2 + \frac{1}{2} \frac{d\varepsilon(t)}{dt} |\mathbf{E}|^2. \quad (11)$$

It is evident that W and \mathbf{S} remain the same as in any regular electromagnetic problem. The difference is on the external power factor p , where extra terms exist, depending on the time derivatives of the permittivity and permeability. The redefined p is a quantitative indication that time-varying media have different energy-transfer characteristics and can allow for amplification of the transmitted signals.

The momentum conservation theorem takes the form [26]:

$$\frac{\partial \mathbf{G}}{\partial t} + \nabla \cdot \mathbb{T} = -\mathbf{f}, \quad (12)$$

where \mathbf{G} is the momentum density vector, \mathbb{T} is the Maxwell stress tensor and $\mathbf{f} = \rho\mathbf{E} + [\mathbf{J} + \sigma(t)\mathbf{E}] \times \mathbf{B}$ is the Lorentz force. It is straightforward to observe that even if the medium is time-dependent, the momentum conservation theorem remains the same, namely [17]:

$$\mathbf{G} = \varepsilon(t)\mu(t)\mathbf{E} \times \mathbf{H}, \quad (13)$$

$$\mathbb{T} = \varepsilon(t)\mathbf{E}\mathbf{E} + \mu(t)\mathbf{H}\mathbf{H} - \frac{1}{2} \left[\varepsilon(t) |\mathbf{E}|^2 + \mu(t) |\mathbf{H}|^2 \right] \mathbb{I}. \quad (14)$$

The electromagnetic field momentum is invariant under homogeneous time-variations of the medium (as expected since the wavenumber is conserved) whereas its energy as shown from the redefined Poynting theorem changes (which is an indication also of the frequency shift, since from a quantum-mechanics point of view energy is directly related with frequency).

2.3 Potentials, Lorentz gauge and Hertz vector

The electric and magnetic fields can be represented by the scalar V and the vector \mathbf{A} potentials [17]:

$$\mathbf{E} = -\nabla V - \frac{\partial \mathbf{A}}{\partial t}, \quad \mathbf{B} = \nabla \times \mathbf{A}. \quad (15)$$

The two corresponding equations for the potentials are:

$$\begin{aligned} \nabla \cdot [\varepsilon(t) \nabla V] + \nabla \cdot \left[\varepsilon(t) \frac{\partial \mathbf{A}}{\partial t} \right] &= -\rho, \\ \nabla \times \nabla \times \mathbf{A} + \mu(t) \frac{\partial(\varepsilon(t) \nabla V)}{\partial t} + \mu(t) \frac{\partial(\varepsilon(t) \mathbf{A})}{\partial t} + \mu(t) \sigma(t) \left[\nabla V + \frac{\partial \mathbf{A}}{\partial t} \right] &= \mu(t) \mathbf{J}. \end{aligned} \quad (16)$$

The potentials are not unique; hence we can choose a suitable gauge to decouple the equations. The Lorentz gauge for these equations is:

$$\nabla \cdot \mathbf{A} + \mu(t) \frac{\partial(\varepsilon(t) \nabla V)}{\partial t} + \mu(t) \sigma(t) V = 0. \quad (17)$$

Under this gauge, the decoupled equation becomes:

$$\nabla^2 \mathbf{A} - \mu(t) \frac{\partial}{\partial t} \left[\varepsilon(t) \frac{\partial \mathbf{A}}{\partial t} \right] - \mu(t) \sigma(t) \frac{\partial \mathbf{A}}{\partial t} = -\mu(t) \mathbf{J}. \quad (18)$$

The equation (18) has three unknowns, we introduce thus the electric Hertz vector, $\mathbf{\Pi}$: $\mathbf{A} = -\mu(t) \partial_t \mathbf{\Pi}$ and $V = \nabla \cdot \mathbf{\Pi} / \varepsilon(t)$.

$$\nabla^2 \mathbf{\Pi} - \varepsilon(t) \frac{\partial}{\partial t} \left(\mu(t) \frac{\partial \mathbf{\Pi}}{\partial t} \right) - \int \sigma(t) \frac{\partial}{\partial t} \left(\mu(t) \frac{\partial \mathbf{\Pi}}{\partial t} \right) dt = \int \mathbf{J} dt, \quad (19)$$

where the electric and magnetic fields are: $\mathbf{H} = -\nabla \times \partial_t \mathbf{\Pi}$ and $\mathbf{E} = -\nabla \nabla \cdot \mathbf{\Pi} / \varepsilon(t) + \partial_t (\mu(t) \partial_t \mathbf{\Pi})$. Provided the time-dependent profiles of $\varepsilon(t)$, $\mu(t)$, $\sigma(t)$ and the space-time dependent source $\mathbf{J}(\mathbf{r}, t)$, a solution for $\mathbf{\Pi}$ can be found leading to the complete knowledge of the electromagnetic fields throughout the time-varying medium. In the next subsection, we derive these corresponding equations and the solution for the special case of a lossless time-varying matched wave medium.

2.4 Integral form of field solutions under a current excitation and matched time-variations

In this subsection, we assume the case of a matched time–variation (wave impedance η is constant) with no losses: $\varepsilon(t) = \varepsilon_0 a(t)$, $\mu(t) = \mu_0 a(t)$ and $\sigma(t) = 0$. We introduce the stretched time–transformation [23,27]:

$$\tau = \int_{t_0}^t dt / a(t), \quad (20)$$

where t_0 is the moment when the current is switched on, then:

$$\nabla^2 \mathbf{\Pi}(\mathbf{r}, \tau) - \varepsilon_0 \mu_0 \frac{\partial^2}{\partial \tau^2} \mathbf{\Pi}(\mathbf{r}, \tau) = \int_0^\tau a(\tau') \mathbf{J}(\mathbf{r}, \tau') d\tau', \quad (21)$$

which is the D'Alembert's equation and has the solution:

$$\mathbf{\Pi}(\mathbf{r}, \tau) = - \int_{\mathbf{r}' \in \mathbb{R}^3} \frac{\int_0^{\tau_r} a(\tau') \mathbf{J}(\mathbf{r}', \tau') d\tau'}{4\pi |\mathbf{r} - \mathbf{r}'|} d^3 \mathbf{r}', \quad (22)$$

where the retarded time is: $\tau_r = \tau - \sqrt{\varepsilon_0 \mu_0} |\mathbf{r} - \mathbf{r}'|$. The electric field is thus easily derived:

$$\begin{aligned}
\mathbf{E}(\mathbf{r}, \tau) = & \int_{\mathbf{r}' \in \mathbb{R}^3} \frac{(3\mathbb{Q} - \mathbb{I})}{4\pi |\mathbf{r} - \mathbf{r}'|^3} \int_0^{\tau_r} \frac{a(\tau') \mathbf{J}(\mathbf{r}', \tau')}{\varepsilon_0 a(\tau)} d\tau' d^3 \mathbf{r}' \\
& + \int_{\mathbf{r}' \in \mathbb{R}^3} \frac{(3\mathbb{Q} - \mathbb{I})}{4\pi |\mathbf{r} - \mathbf{r}'|^2} \sqrt{\frac{\mu_0}{\varepsilon_0}} \frac{a(\tau_r) \mathbf{J}(\mathbf{r}', \tau_r)}{a(\tau)} d^3 \mathbf{r}' \\
& + \int_{\mathbf{r}' \in \mathbb{R}^3} \frac{(\mathbb{Q} - \mathbb{I})}{4\pi |\mathbf{r} - \mathbf{r}'|} \frac{\mu_0}{\varepsilon_0} \frac{\partial_\tau [a(\tau) \mathbf{J}(\mathbf{r}', \tau)]_{\tau=\tau_r}}{a(\tau)} d^3 \mathbf{r}'.
\end{aligned} \tag{23}$$

where $\mathbb{Q} = \boldsymbol{\Theta} \boldsymbol{\Theta} \cdot$, with $\boldsymbol{\Theta} = (\mathbf{r} - \mathbf{r}') / |\mathbf{r} - \mathbf{r}'|$. The last term represents the far field radiation. If $a(\tau) \mathbf{J}(\mathbf{r}, \tau)$ is constant in the τ -domain then there is no far field, which means that the material variations can be engineered to compensate for the radiation of the currents and the radiation would decay very rapidly away from the source. In the case of a DC excitation: $\partial_\tau [a(\tau) \mathbf{J}(\mathbf{r})] = \mathbf{J}(\mathbf{r}) \partial_\tau a(\tau) \neq 0$, the system exhibits far field radiation even if the source current is steady. In this case, the far field radiation is a product of the static source interacting with the time-varying medium.

The differences between the solution of $\mathbf{E}(\mathbf{r}, \tau)$, as shown in (23) and the well-known integral solutions of an electric field in vacuum $\mathbf{E}(\mathbf{r}, t)$ are in the presence of the time weighting (the difference between t and τ) and in the modulation of the source current density ($a(\tau) \mathbf{J}(\mathbf{r}, \tau)$). The propagation of the electromagnetic waves in a time-varying constant-impedance medium can be viewed as a similar one in vacuum, where the causal time delay is measured in the stretched τ time axis. The physical measurement however is performed in t . Thus, an inverse mapping of $t(\tau)$ is required and can be directly applied to bring back the field solution of (23) to the t -domain. Such inverse mapping is straightforward if the integral of (20) is analytic.

For the general equations regarding the electromagnetic problem of propagation under nonstationary and inhomogeneous and the appropriate decoupling conditions consult Appendix A.

2.5 Electromagnetic modes in the absence of sources

As is directly observed from Maxwell's equations \mathbf{E} and \mathbf{H} can be discontinuous as the medium varies in time. The fields that remain continuous in time are: \mathbf{D} and \mathbf{B} . For this reason, it is more convenient to solve for these fields. The corresponding second order differential equations are:

$$\nabla^2 \mathbf{D}(\mathbf{r}, t) - \varepsilon(t) \frac{\partial}{\partial t} \left[\mu(t) \frac{\partial \mathbf{D}(\mathbf{r}, t)}{\partial t} \right] - \varepsilon(t) \frac{\partial}{\partial t} \left[\frac{\mu(t) \sigma(t)}{\varepsilon(t)} \mathbf{D}(\mathbf{r}, t) \right] = 0, \quad (24)$$

$$\nabla^2 \mathbf{B}(\mathbf{r}, t) - \mu(t) \frac{\partial}{\partial t} \left[\varepsilon(t) \frac{\partial \mathbf{B}(\mathbf{r}, t)}{\partial t} \right] - \mu(t) \sigma(t) \frac{\partial \mathbf{B}(\mathbf{r}, t)}{\partial t} = 0. \quad (25)$$

Equations (24) and (25) are separableⁱ. We can thus use the separation of variables method and assume solutions for $\mathbf{U} = \mathbf{D}$ or \mathbf{B} of the form: $\mathbf{U}(\mathbf{r}, t) = \mathbf{R}(\mathbf{r})T(t)$ [17]. The real solutions of $\mathbf{R}(\mathbf{r})$ and $T(t)$ represent a summation of standing waves, whereas the complex solutions of $\mathbf{R}(\mathbf{r})$ and $T(t)$ represent a summation of propagating waves. If the complex solutions are found the actual solutions in t – domain are: $\text{Re}[\mathbf{U}(\mathbf{r}, t)] = \text{Re}[\mathbf{R}(\mathbf{r})T(t)]$.

ⁱ Notice that eq. (25) is the same with eq. (18) of the vector potential under the Lorentz gauge. As we later see the equation of the form (25) or (18) is the main equation that is required for the solution of all the fields.

The second order ordinary differential equation of $\mathbf{R}(\mathbf{r})$ can be easily found to be the Helmholtz equation (for both the electric displacement and the magnetic induction):

$$\nabla^2 \mathbf{R}(\mathbf{r}) + k^2 \mathbf{R}(\mathbf{r}) = 0, \quad (26)$$

where k is the wavenumber, which remains constant despite any material temporal change as indicated by the separability of the differential equations (24), (25).

The differential equation of $T(k, t)$ is:

$$\frac{d^2 T(k, t)}{dt^2} + P(t) \frac{dT(k, t)}{dt} + Q(k, t) T(k, t) = 0, \quad (27)$$

where for the electric displacement, \mathbf{D} : $P(t) = \frac{\sigma(t)}{\varepsilon(t)} + \frac{d \ln \mu(t)}{dt}$ and

$Q(k, t) = \frac{1}{\mu(t)} \frac{d}{dt} \left[\frac{\mu(t) \sigma(t)}{\varepsilon(t)} \right] + \frac{k^2}{\varepsilon(t) \mu(t)}$. While for the magnetic induction, \mathbf{B} :

$P(t) = \frac{\sigma(t)}{\varepsilon(t)} + \frac{d \ln \varepsilon(t)}{dt}$ and $Q(k, t) = \frac{k^2}{\varepsilon(t) \mu(t)}$.

If $T_b(k, t)$ is the solution for the magnetic induction then the solution for the electric displacement, $T_d(k, t)$ is:

$$T_d(k, t) = e^{-\int^{\sigma(\zeta) d\zeta / \varepsilon(\zeta)} \int T_b(k, \zeta) e^{\int^{\sigma(\zeta') d\zeta' / \varepsilon(\zeta')} d\zeta}. \quad (28)$$

For a given wavenumber k , the solutions for the electric displacement and magnetic induction have identical spatial dependence ($\mathbf{R}(\mathbf{r})$), while the relation (28) connects the time solutions of the magnetic induction with the time solutions of the electric displacement. The electromagnetic problem is thus reduced to the solution of eq. (25).

The complex (propagating base) $\mathbf{R}(\mathbf{r})$ for a given k has the form:

$$\mathbf{R}(\mathbf{r}) = \int_0^\pi \int_0^{2\pi} \mathbf{F}(\varphi, \theta) e^{i\mathbf{k}\cdot\mathbf{r}} d\varphi d\theta, \quad (29)$$

where \mathbf{F} is a vector dependent on the spherical coordinates θ , φ and $\mathbf{k} = k \sin\theta \cos\varphi \hat{x}_1 + k \sin\theta \sin\varphi \hat{x}_2 + k \cos\theta \hat{x}_3$ is the wavevector. The solution of (29) is for the space $\mathbf{r} = (x_1, x_2, x_3)$ far away from the sources (similar with the plane wave solution in stationary media). Additionally, it is assumed that a substantial period of time has passed without any material conductivity (loss) and therefore the field solutions have filled the region.

On the other hand, the solution of the time–function is strongly dependent on the type of the time–variation of the medium (as indicated in eq. (27)). It is though obvious that the second order differential equation result in two independent solutions: $T_1(k, t)$ and $T_2(k, t)$.

The general solution, if $T_{1,2}(k, t)$ and $\mathbf{F}(\varphi, \theta)$ are known, is:

$$\mathbf{U}(\mathbf{r}, t) = \int [\mathbf{F}_1(\mathbf{k}) T_1(k, t) + \mathbf{F}_2(\mathbf{k}) T_2(k, t)] e^{i\mathbf{k}\cdot\mathbf{r}} d^3k, \quad (30)$$

where $\mathbf{F}_{1,2}(\mathbf{k}) = C_{1,2}(k)\mathbf{F}(\varphi, \theta)$ and C_1, C_2 represent the coefficients of the electromagnetic modes which propagate at the positive and negative direction, respectively. For slowly and continuously varying parameters the Liouville–Green approximation [28] can be directly applied to approximate the time–function solutions:

$$T_b(k, t) \approx \sqrt[4]{\frac{\mu(t)}{\varepsilon(t)}} e^{-\frac{1}{2} \int \frac{\sigma(\zeta) d\zeta}{\varepsilon(\zeta)}} \left[C_1 e^{-ik \int \frac{d\zeta}{\sqrt{\varepsilon(\zeta)\mu(\zeta)}}} + C_2 e^{+ik \int \frac{d\zeta}{\sqrt{\varepsilon(\zeta)\mu(\zeta)}}} \right], \quad (31)$$

$$T_d(k, t) \approx e^{-\int \frac{\sigma(\zeta) d\zeta}{\varepsilon(\zeta)}} \int \sqrt[4]{\frac{\mu(\zeta)}{\varepsilon(\zeta)}} e^{\frac{1}{2} \int \frac{\sigma(\zeta') d\zeta'}{\varepsilon(\zeta')}} \left[C_1 e^{-ik \int \frac{d\zeta'}{\sqrt{\varepsilon(\zeta')\mu(\zeta')}}} + C_2 e^{+ik \int \frac{d\zeta'}{\sqrt{\varepsilon(\zeta')\mu(\zeta')}}} \right] d\zeta, \quad (32)$$

The effective velocity can be defined directly by the Liouville–Green approximation as: $c_{\text{eff}}(t) = \frac{\int d\zeta / \sqrt{\varepsilon(\zeta)\mu(\zeta)}}{t}$, for $\zeta \leq t$. The presence of the conductivity results in the attenuation of the fields by a $e^{-\frac{1}{2} \int \sigma(t) dt / \varepsilon(t)}$ factor.

If the time–variation of the medium is known and we can also measure the electric and magnetic fields at an observation time t_0 , we can find the complete solution of (30) for $t > t_0$.

First, we can find the $T_{1,2}(k, t)$ from eq. (27), since the time–dependent profiles of $\varepsilon(t)$, $\mu(t)$, $\sigma(t)$ are known. Then we have to define $\mathbf{U}(\mathbf{r}, t_0)$ and $\partial_t \mathbf{U}(\mathbf{r}, t_0)$ by the measurements of $\mathbf{E}(\mathbf{r}, t_0)$ and $\mathbf{H}(\mathbf{r}, t_0)$. The time–domain observation of the fields is in the real domain. In order to apply them as temporal boundary conditions for the complex (propagating) \mathbf{U} we need to convert them in the complex space. This is feasible by the direct application of the Hilbert

transform, which leads to the analytic form of the signals. More precisely if $\Psi(\mathbf{r}) = \mathbf{E}(\mathbf{r}, t_0)$ or $\mathbf{H}(\mathbf{r}, t_0)$, then its Hilbert transform is [29]:

$$\tilde{\Psi}(\mathbf{r}) = \prod_{j=1}^3 \left[\delta(x_j) + \frac{i}{\pi x_j} \right] ** \Psi(\mathbf{r}), \quad (33)$$

where $\delta(x_j)$ is the Kronecker delta function with respect to the Cartesian coordinate x_j and $***$ is the 3-fold convolution. Depending on which field \mathbf{U} we choose to do our analysis with, we can derive for the magnetic induction: $\tilde{\mathbf{B}}(\mathbf{r}, t_0) = \mu(t_0) \tilde{\mathbf{H}}(\mathbf{r}, t_0)$ and $\partial_t \tilde{\mathbf{B}}(\mathbf{r}, t_0) = -\nabla \times \tilde{\mathbf{E}}(\mathbf{r}, t_0)$, and for the electric displacement: $\tilde{\mathbf{D}}(\mathbf{r}, t_0) = \varepsilon(t_0) \tilde{\mathbf{E}}(\mathbf{r}, t_0)$ and $\partial_t \tilde{\mathbf{D}}(\mathbf{r}, t_0) = \nabla \times \tilde{\mathbf{H}}(\mathbf{r}, t_0) - \sigma(t_0) \tilde{\mathbf{E}}(\mathbf{r}, t_0)$. While the Wronski determinant $\Delta(t)$ is for the magnetic induction:

$$\Delta_b(t) = \Delta_b(t_0) \frac{\varepsilon(t_0)}{\varepsilon(t)} e^{-\int_{t_0}^t \sigma(\zeta) d\zeta / \varepsilon(\zeta)}, \quad (34)$$

and for the electric displacement:

$$\Delta_d(t) = \Delta_d(t_0) \frac{\mu(t_0)}{\mu(t)} e^{-\int_{t_0}^t \sigma(\zeta) d\zeta / \varepsilon(\zeta)}. \quad (35)$$

The determination of the vectors $\mathbf{F}_1(\mathbf{k})$, $\mathbf{F}_2(\mathbf{k})$ and hence the k -context of the wave resulting in the complete solution of the wave problem can be directly

derived by the application of the inverse Fourier integral to $\mathbf{U}(\mathbf{r}, t_0)$ and $\partial_t \mathbf{U}(\mathbf{r}, t_0)$:

$$\mathbf{F}_1(\mathbf{k}) = \frac{\frac{dT_2(k, t_0)}{dt} \int \mathbf{U}(\mathbf{r}, t_0) e^{-i\mathbf{k}\cdot\mathbf{r}} d^3r - T_2(k, t_0) \int \frac{\partial \mathbf{U}(\mathbf{r}, t_0)}{\partial t} e^{-i\mathbf{k}\cdot\mathbf{r}} d^3r}{8\pi^3 \Delta(t_0)}, \quad (36)$$

$$\mathbf{F}_2(\mathbf{k}) = -\frac{\frac{dT_1(k, t_0)}{dt} \int \mathbf{U}(\mathbf{r}, t_0) e^{-i\mathbf{k}\cdot\mathbf{r}} d^3r - T_1(k, t_0) \int \frac{\partial \mathbf{U}(\mathbf{r}, t_0)}{\partial t} e^{-i\mathbf{k}\cdot\mathbf{r}} d^3r}{8\pi^3 \Delta(t_0)}. \quad (37)$$

2.6 Temporal material discontinuities: Scattering matrix formulation

Waves experience reflections under temporal material discontinuities. Let us assume that at $t = \tau$ the temporal functions of $\varepsilon(t)$, $\mu(t)$ and $\sigma(t)$ or their derivatives exhibit a discontinuity. It is clear (see eq. (27)) that this discontinuity is carried to $d^2T(k, t)/dt^2$, leaving $T(k, t)$ and $dT(k, t)/dt$ continuous, if either the permeability or permittivity of the dynamic medium remains continuous. More precisely, if the permeability is continuous the electric displacement field and its time derivative are continuous, whereas if the permittivity is continuous the magnetic induction field and its time derivative are continuous. Under such assumptions we can formulate the temporal scattering matrix.

If the solution for $t < \tau$ is:

$$T_{<}(k, t) = C_1^< T_1^<(k, t) + C_2^< T_2^<(k, t), \quad (38)$$

and for $t > \tau$ is:

$$T_{>}(k, t) = C_1^> T_1^>(k, t) + C_2^> T_2^>(k, t), \quad (39)$$

then the continuity relations at $t = \tau$ give us the temporal scattering matrix:

$$\begin{pmatrix} C_1^> \\ C_2^> \end{pmatrix} = S_\tau \cdot \begin{pmatrix} C_1^< \\ C_2^< \end{pmatrix} = \begin{pmatrix} \frac{\frac{dT_1^<(k, \tau)}{dt} T_2^>(k, \tau) - \frac{dT_2^<(k, \tau)}{dt} T_1^<(k, \tau)}{\frac{dT_1^<(k, \tau)}{dt} T_2^>(k, \tau) - \frac{dT_2^<(k, \tau)}{dt} T_1^<(k, \tau)}, & \frac{\frac{dT_2^<(k, \tau)}{dt} T_2^>(k, \tau) - \frac{dT_2^<(k, \tau)}{dt} T_2^<(k, \tau)}{\frac{dT_1^<(k, \tau)}{dt} T_2^>(k, \tau) - \frac{dT_2^<(k, \tau)}{dt} T_1^<(k, \tau)} \\ \left[\frac{T_1^<(k, \tau) - T_1^>(k, \tau)}{\frac{dT_1^<(k, \tau)}{dt} T_2^>(k, \tau) - \frac{dT_2^<(k, \tau)}{dt} T_1^<(k, \tau)} \right] \left[\frac{dT_1^<(k, \tau)}{dt} - \frac{d \ln T_2^>(k, \tau)}{dt} T_1^<(k, \tau) \right], & \left[\frac{T_2^<(k, \tau) - T_1^>(k, \tau)}{\frac{dT_1^<(k, \tau)}{dt} T_2^>(k, \tau) - \frac{dT_2^<(k, \tau)}{dt} T_1^<(k, \tau)} \right] \left[\frac{dT_2^<(k, \tau)}{dt} - \frac{d \ln T_2^>(k, \tau)}{dt} T_2^<(k, \tau) \right] \end{pmatrix} \cdot \begin{pmatrix} C_1^< \\ C_2^< \end{pmatrix}. \quad (40)$$

S_{11} and S_{22} are the parameters which correspond to the temporal transmission, whereas S_{21} and S_{12} are the parameters for the temporal reflection.

If we assume the simple case where a wave propagates at a medium with ε_1 , μ_1 , σ_1 (which are constant) and at $t=0$ the medium changes its electromagnetic-material properties to ε_2 , μ_2 , σ_2 (which are also considered constant). The ordinary differential equation that satisfies $T(k, t)$ for both \mathbf{D} and \mathbf{B} is the same (for constant values of ε , μ , σ). The time-domain solution of the resulting differential equations under nonstationary conditions (for either the \mathbf{D} or the \mathbf{B} field according to the continuity conditions) is of the

form: $\zeta(r, t) = \zeta_0 \cos \left[\mathbf{k} \cdot \mathbf{r} - \left(\frac{1}{2\varepsilon} \sqrt{\frac{4\varepsilon k^2 - \sigma^2 \mu}{\mu}} \right) t \right] e^{-\frac{\sigma t}{2\varepsilon}}$, where we can assume that

the wavevector has the direction of any of the Cartesian unit vectors. This mode along with the identical one propagating in the opposite direction can be

used as an expansion basis to form the general solution. Additionally, losses effect the field in time since the fields have filled the whole space as assumed in the analysis (contradictory to the stationary–medium plane–wave equivalent). The analytic signal of the complex field \mathbf{U} is:

$$\mathbf{U} = \begin{cases} \mathbf{U}_0 e^{i\mathbf{k}\cdot\mathbf{r} - \left(\frac{\sigma_1}{2\varepsilon_1} + \frac{i}{2\varepsilon_1} \sqrt{\frac{4\varepsilon_1 k^2 - \sigma_1^2 \mu_1}{\mu_1}}\right)t}, & t < 0 \\ \mathbf{U}_0 S_{11} e^{i\mathbf{k}\cdot\mathbf{r} - \left(\frac{\sigma_2}{2\varepsilon_2} + \frac{i}{2\varepsilon_2} \sqrt{\frac{4\varepsilon_2 k^2 - \sigma_2^2 \mu_2}{\mu_2}}\right)t} + \mathbf{U}_0 S_{21} e^{i\mathbf{k}\cdot\mathbf{r} - \left(\frac{\sigma_2}{2\varepsilon_2} - \frac{i}{2\varepsilon_2} \sqrt{\frac{4\varepsilon_2 k^2 - \sigma_2^2 \mu_2}{\mu_2}}\right)t}, & t > 0 \end{cases} \quad (41)$$

From the continuity relations we get the scattering matrix (from eq. (40)):

$$S_0 = \begin{pmatrix} \frac{1}{2} \left[\frac{\sqrt{\varepsilon_1 \mu_1} + \sqrt{\varepsilon_2 \mu_2}}{\sqrt{\varepsilon_1 \mu_1}} + i \frac{(\sigma_2 \varepsilon_1 - \sigma_1 \varepsilon_2)}{2\varepsilon_1 k} \sqrt{\frac{\mu_2}{\varepsilon_2}} \right], & \frac{1}{2} \left[\frac{\sqrt{\varepsilon_1 \mu_1} - \sqrt{\varepsilon_2 \mu_2}}{\sqrt{\varepsilon_1 \mu_1}} + i \frac{(\sigma_2 \varepsilon_1 - \sigma_1 \varepsilon_2)}{2\varepsilon_1 k} \sqrt{\frac{\mu_2}{\varepsilon_2}} \right] \\ \frac{1}{2} \left[\frac{\sqrt{\varepsilon_1 \mu_1} - \sqrt{\varepsilon_2 \mu_2}}{\sqrt{\varepsilon_1 \mu_1}} - i \frac{(\sigma_2 \varepsilon_1 - \sigma_1 \varepsilon_2)}{2\varepsilon_1 k} \sqrt{\frac{\mu_2}{\varepsilon_2}} \right], & \frac{1}{2} \left[\frac{\sqrt{\varepsilon_1 \mu_1} + \sqrt{\varepsilon_2 \mu_2}}{\sqrt{\varepsilon_1 \mu_1}} - i \frac{(\sigma_2 \varepsilon_1 - \sigma_1 \varepsilon_2)}{2\varepsilon_1 k} \sqrt{\frac{\mu_2}{\varepsilon_2}} \right] \end{pmatrix}. \quad (42)$$

This scattering matrix has interesting properties. We observe that: $S_{11} + S_{21} = 1$, $S_{12} + S_{22} = 1$, $\det(S_0) = \sqrt{\frac{\varepsilon_1 \mu_1}{\varepsilon_2 \mu_2}}$ and the inverse S_0^{-1} corresponds to the scattering by the time–reversed material–parameter transition. Additionally, if the wave impedance, η and σ/ε remain constant S_{21} and S_{12} extinguish, i.e. the wave does not reflect. The scattering matrix formalism can be equally used for standing waves without necessarily reformulating the complex solutions of $\mathbf{R}(\mathbf{r})$ and $T(t)$, since standing waves are a superposition of propagating solutions of opposite direction. Note that in an application, there can be some temporal dispersive effects which may generate high frequencies due to the abrupt change of the material parameters. However,

these generated amplitudes are expected small and exponentially decaying with time due to the momentum conservation. The analysis of time-varying media with the combination of dispersive effects is given in Appendix B.

2.7 Electromagnetic modes of time-Floquet media

In this subsection, we present the steady-state solutions of the electromagnetic field in a time-Floquet (time-periodic) medium in the absence of losses [24].

The wave equation for the electric field is:

$$\nabla^2 E(\mathbf{r}, t) - \frac{\partial}{\partial t} \left[\mu(t) \frac{\partial(\varepsilon(t) E(\mathbf{r}, t))}{\partial t} \right] = 0. \quad (43)$$

The medium has plane-wave solutions (as shown in the previous section), namely: $E(\mathbf{r}, t) = E(t)e^{i\mathbf{k}\cdot\mathbf{r}}$, with $\mathbf{k} = k\hat{\mathbf{k}}$ and k is the wavenumber. Eq. (43) becomes:

$$k^2 E(t) + \frac{d}{dt} \left[\mu(t) \frac{d(\varepsilon(t) E(t))}{dt} \right] = 0 \quad (44)$$

The permittivity and the permeability are considered periodic with circular modulation frequency: $\omega_m = 2\pi/T$, where T is the period. Hence the functions of $\mu(t)$ and $\varepsilon(t)$ can be expanded in series:

$$\varepsilon(t) = \sum_p \varepsilon_p e^{ip\omega_m t}, \quad (45)$$

$$\mu(t) = \sum_l \mu_l e^{il\omega_m t}, \quad (46)$$

where $p, l \in \mathbb{Z}$. The solution for the electric field is found using the Bloch–Floquet ansatz:

$$E(t) = \sum_n E_n e^{-i(\omega - n\Omega)t}, \quad (47)$$

where ω is the excitation frequency and $n \in \mathbb{Z}$. Substituting eqs. (45)–(47) to (44) the system of equations satisfies:

$$\sum_{p,n} \left[\mu_{l-p} \varepsilon_{p-n} (\omega - l\omega_m)(\omega - p\omega_m) - k^2 \delta_{lp} \delta_{p0} \right] E_n(\omega) = 0, \quad (48)$$

where δ_{lp} is the Kronecker delta function. Eq. (48) is a set of an infinite number of linear equations for an infinite number of eigenmodes of $E_n(\omega)$, $n \in \mathbb{Z}$. The propagating relations (dispersion relations) of $k(\omega)$ or $\omega(k)$ are the values which vanish the determinant coefficients of $E_n(\omega)$.

It is directly observed that: $k(\omega + n\omega_m) = k(\omega)$, which means that the band structure is periodic in the circular frequency (with the period being ω_m).

In the case of a weak modulation, $\varepsilon(t)$ and $\mu(t)$ reduce to their average values: $\bar{\varepsilon}$ and $\bar{\mu}$, so that: $\varepsilon_{p-n} = \bar{\varepsilon}\delta_{pn}$ and $\mu_{l-p} = \bar{\mu}\delta_{lp}$. Consequently, the dispersion relation is found:

$$\omega = l\omega_m \pm k/\sqrt{\bar{\varepsilon}\bar{\mu}}. \quad (49)$$

For $l=0$, the two corresponding solutions are the plane waves to the positive and the negative direction with velocity: $(\bar{\varepsilon}\bar{\mu})^{-1/2}$. For $l \neq 0$, the dispersion lines are displaced along the frequency axis by $l\omega_m$. This is caused by the temporal periodicity of the medium corresponding to the “empty temporal lattice” model, analogously with the “empty spatial lattice” [30]. For small values of the excitation frequency ω the dominant modes are for $l=0$ and $l=1$, which intersect at $\omega = \frac{1}{2}\omega_m$ and $k = \frac{1}{2}\Omega\sqrt{\bar{\varepsilon}\bar{\mu}}$ and result in the equations:

$$\left[\bar{\varepsilon}\bar{\mu}\omega^2 - k^2 + \varepsilon_1\mu_{-1}\omega(\omega - \omega_m)\right]E_0(\omega) + \left[\varepsilon_{-1}\bar{\mu}\omega^2 + \bar{\varepsilon}\mu_{-1}\omega(\omega - \omega_m)\right]E_1(\omega) = 0, \quad (50)$$

$$\begin{aligned} &\left[\bar{\varepsilon}\mu_1\omega(\omega - \omega_m) + \varepsilon_1\bar{\mu}\omega(\omega - \omega_m)^2\right]E_0(\omega) \\ &+ \left[\bar{\varepsilon}\bar{\mu}(\omega - \omega_m)^2 - k^2 + \varepsilon_{-1}\mu_1\omega(\omega - \omega_m)\right]E_1(\omega) = 0. \end{aligned} \quad (51)$$

It can be shown that $k(\omega) = k(\omega_m - \omega)$, which implies that the bands possess a mirror symmetry about the intersection point $\omega = \frac{1}{2}\omega_m$. This suggests a gap between the k -bands. This gap can be found (analogously to the spatial periodic equivalent [31,32]) as:

$$\frac{\Delta k}{\bar{k}} \approx \frac{1}{2} |m_\varepsilon - m_\mu|, \quad (52)$$

where m_ε, m_μ are the modulation depths for the permittivity and the permeability respectivelyⁱⁱ and $\bar{k} = \sqrt{\varepsilon\mu}\omega$, where the material modulation is considered as simply: $\varepsilon(t) = \varepsilon_0[1 + m_\varepsilon \cos(\omega_m t)]$ and $\mu(t) = \mu_0[1 + m_\mu \cos(\omega_m t)]$.

Let us limit our analysis to the case of a periodic permittivity, $\varepsilon = \varepsilon(t)$ and a constant permeability, $\mu = \mu_0$. The resulting equation is a particular case of the Sturm–Liouville eigenvalue problem:

$$\left[\frac{d}{dt} \left(q_1(t) \frac{d}{dt} \right) + q_2(t) \right] E(t) + \lambda w(t) E(t) = 0, \quad (53)$$

where: $q_1(t) = \varepsilon^2(t)$, $q_2(t) = \varepsilon(t) \frac{d^2 \varepsilon(t)}{dt^2}$, $\lambda = \frac{k^2}{\mu_0}$ and $w(t) = \varepsilon(t)$. The Sturm–Liouville problem guaranties that the eigenvalues: k^2/μ_0 are real and the modes form a complete basis and are orthogonal (with respect to the weight function of $\varepsilon(t)$)ⁱⁱⁱ. Different eigenmodes suggest different wavenumbers. The field modes have the form: $E_r(\omega, t) = \sum_n E_{rn} e^{-i(\omega - n\omega_m)t}$, for the r^{th} solution (with $k = k_r$). The orthogonality relations for two modes r and q are:

ⁱⁱ Notice that when the wave impedance remains constant: $m_\varepsilon = m_\mu$, the wave in the time–domain exhibit no temporal reflections and thus the k – gap closes.

ⁱⁱⁱ This is not guaranteed in the case where both permittivity and permeability are temporally modulated.

$$\frac{1}{N_r^2} \sum_{np} \varepsilon_{n-p} E_{rp}(\omega) E_{qn}^*(\omega) = \delta_{qr} \quad (54)$$

where δ is the Kronecker delta function and N_r is the normalization factor which satisfies the completeness relation:

$$\sum_r \frac{1}{N_r^2} \int_0^{\omega_m} E_r(\omega, t) E_r^*(\omega, t') e^{-i\omega(t-t')} d\omega = 2\pi \delta(t-t'). \quad (55)$$

Eq. (48) becomes:

$$\sum_{n,p} \left[(\omega - m\omega_m)^2 \varepsilon_{p-n} - \frac{k_r^2}{\mu_0} \delta_{pn} \right] E_{rn}(\omega) = 0. \quad (56)$$

The solutions of eq. (56) possess a symmetry around $n \frac{\omega_m}{2}$, $n \in \mathbb{Z}$. To illustrate such a symmetry we define two frequencies: $\omega_1 = n\omega_m/2 + \omega$ and $\omega_2 = n\omega_m/2 - \omega$. Plugging them into eq. (56), we find that they correspond to the same eigenvalues k_r , which means: $k(n\omega_m/2 + \omega) = k(n\omega_m/2 - \omega)$. This symmetry indicates the presence of a maximum or a minimum at $n\omega_m/2$ leading to the relation:

$$\left. \frac{dk}{d\omega} \right|_{\omega=n\frac{\omega_m}{2}} = 0. \quad (57)$$

Eq. (57) indicates a group velocity reaching to infinity. If it is assumed that just a single k (harmonic solution) exists then according to the uncertainly principle the wave must fill the whole space, therefore the speed of the wave is irrelevant. If now it is assumed that the wave doesn't fill the whole space, then the velocity of the information is not the group velocity but the front velocity as found by Sommerfeld [33], which is a high frequency component leading to a velocity equal to the velocity of light.

For the long-wavelength limit an effective parameter of the permittivity can be obtained (similarly as is derived using the Green–Liouville approximation in eq. (31)–(32)):

$$\varepsilon_{\text{eff}} = \frac{T}{\int_0^T dt / \varepsilon(t)}. \quad (58)$$

In Fig. 3, the dispersion relation is shown for the case of a step variation of the permittivity:

$$\varepsilon(t) = \begin{cases} \varepsilon_1, & 0 < t < \tau \\ \varepsilon_2, & \tau < t < T \end{cases} \quad (59)$$

with T period. In Fig. 3(a), the dispersion of the time periodic–medium with $\varepsilon_1 = 2\varepsilon_0$, $\varepsilon_2 = \varepsilon_0$ and $\tau = T/2$, while in Fig. 3(b) the dispersion with $\varepsilon_1 = 3\varepsilon_0$, $\varepsilon_2 = \varepsilon_0$ and $\tau = T/2$ are computed.

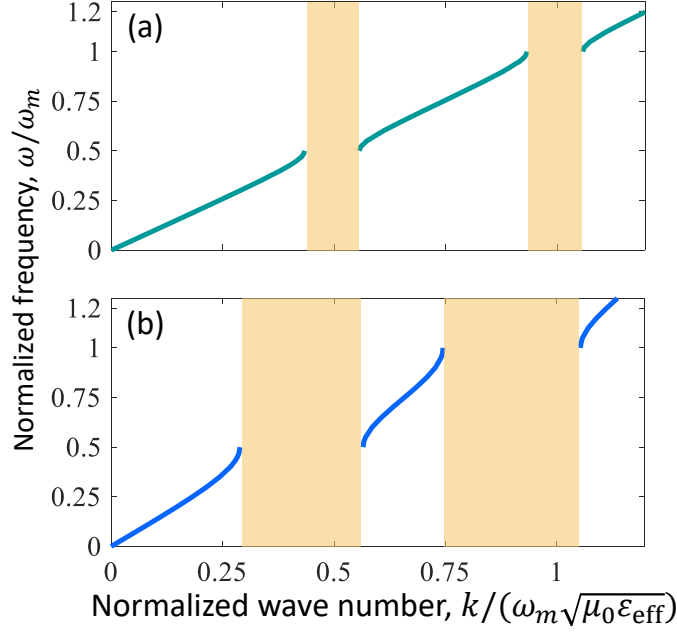


Figure 3: (a) Dispersion relation of the time periodic medium with $\varepsilon_1 = 2\varepsilon_0$, $\varepsilon_2 = \varepsilon_0$ and $\tau = T/2$. (b) Dispersion relation of the time periodic medium with $\varepsilon_1 = 3\varepsilon_0$, $\varepsilon_2 = \varepsilon_0$ and $\tau = T/2$. The calculations were performed considering 201 Floquet harmonics. Figure adapted from [18].

The symmetries of the dispersion relations as found before [$k(\omega + n\omega_m) = k(\omega)$ and $k(n\omega_m/2 + \omega) = k(n\omega_m/2 - \omega)$] allow the complete computation of the dispersion relation by finding the corresponding solutions in the vicinity of the light cone for $\varepsilon = \varepsilon_{\text{eff}}$.

2.8 Parametric amplification at the momentum gaps

In this subsection, the wave behavior in the k -gaps of a time-periodic medium is studied and explained. As proven in Section 2.2, energy is not conserved in these problems and waves can be amplified. To deal with such a problem, techniques are employed regarding hypergeometric equations and their stability [18].

The electric displacement field equation for a time-periodic permittivity (with a period of T) is:

$$\frac{d^2 T_d}{dt^2} + \frac{k^2}{\mu_0 \varepsilon(t)} T_d = 0. \quad (60)$$

Eq. (60) is the general Hill's equation [34]. The field vector: $\mathbf{T}_d = [T_d, d_t T_d]^T$, results in the reformed equation:

$$d_t \mathbf{T}_d = \begin{bmatrix} 0 & 1 \\ -k^2/\mu_0 \varepsilon(t) & 0 \end{bmatrix} \mathbf{T}_d. \quad (61)$$

Since the differential equation is of the second order the Wronskian is a 2×2 matrix, formed by the two independent solutions \mathbf{T}_{d1} and \mathbf{T}_{d2} : $\mathbf{W}(t) = [\mathbf{T}_{d1}, \mathbf{T}_{d2}]$. Hence the time-evolution from t_1 to t_2 of the wave signal is defined by the matrix: $\Phi(t_2, t_1) = \mathbf{W}(t_2) \mathbf{W}(t_1)^{-1}$. As it is directly found by the Floquet theory for a time-periodic system: $\Phi(mT, 0) = \Phi(T, 0)^m$.

In order to check the stable wave solutions, the eigenvalues λ_1 and λ_2 of $\Phi(T, 0)$ should be restricted to $|\lambda_{1,2}| < 1$.

The eigenvalues are:

$$\lambda_{1,2} = \frac{\text{tr}(\Phi(T, 0))}{2} \pm \sqrt{\left[\frac{\text{tr}(\Phi(T, 0))}{2} \right]^2 - 1}, \quad (62)$$

and thus, the stability condition requires:

$$|\text{tr}(\mathbf{\Phi}(T,0))| < 2. \quad (63)$$

If we return back to the problem of the step variation of the permittivity (see eq. (59)), $\mathbf{\Phi}(T,0)$ has a closed form formulation (since the two independent solutions are easily found as shown in previous subsections) and the stability condition (63) leads to the inequality:

$$\left| \cos \left[\frac{2k}{\omega_m \sqrt{\mu_0 \varepsilon_2}} \left(\pi - \frac{\omega_m \tau}{2} \right) \right] \cos \left[\frac{k}{\sqrt{\mu_0 \varepsilon_1}} \tau \right] - \frac{1}{2} \left[\frac{\varepsilon_1 + \varepsilon_2}{\sqrt{\varepsilon_1 \varepsilon_2}} \right] \sin \left[\frac{2k}{\omega_m \sqrt{\mu_0 \varepsilon_2}} \left(\pi - \frac{\omega_m \tau}{2} \right) \right] \sin \left[\frac{k}{\sqrt{\mu_0 \varepsilon_1}} \tau \right] \right| < 1. \quad (64)$$

Assuming a small variation of the medium: $|\varepsilon_2 - \varepsilon_1| \rightarrow 0$ we find marginal instability for:

$$\frac{k}{\omega_m} \sqrt{\frac{2(\varepsilon_2 + \varepsilon_1)}{\mu_0 \varepsilon_1 \varepsilon_2}} = n, \quad n \in \mathbb{Z}. \quad (65)$$

From eq. (58): $\varepsilon_{\text{eff}} = \frac{2\varepsilon_2 \varepsilon_1}{\varepsilon_1 + \varepsilon_2}$, which is no coincidence. Indeed, the condition of (65) is at the k – gap of the dispersion relation:

$$\omega = \frac{k}{\sqrt{\mu_0 \varepsilon_{\text{eff}}}} = n \frac{\omega_m}{2}. \quad (66)$$

In these specific frequencies, the energy provided to modulate the medium is optimally coupled to the existing wave, leading to parametric wave pumping. This is evident since at these frequencies the eigenvalues of $\Phi(T, 0)$ collide to unity and the system experiences t – multiplied instability. This means that no matter how small the difference of the dielectric permittivity, the system provides gain of parametric nature to the wave signal. From the mathematical analysis, we find that the second solution is an evanescent mode which is also an acceptable solution which corresponds to the absorption of the external pump that causes the time–modulation (the parametrical amplified one usually dominates). The stability charts regarding the condition (64) are illustrated for representative values of τ in Fig. 4. The stability charts are defined by the parameters $\alpha = \frac{4k^2}{\omega_m^2 \mu_0 \varepsilon_{\text{eff}}}$ and $q = \frac{2k^2}{\omega_m^2 \mu_0} \left[\frac{1}{\varepsilon_{\text{eff}}} - \frac{1}{\varepsilon_1} \right]$, which are often used in the analysis of the corresponding Hill’s equations^{iv}. The α parameter represents the wave operation in relation with the effective permittivity, while q represents the modulation depth (which is a quantitative parameter proportional to $\varepsilon_1 - \varepsilon_2$).

^{iv} The solution can be mapped as shown in [18] with the Hill’s equation:

$\frac{d^2 T(\xi)}{d\xi^2} + [a - 2qf(\xi)]T(\xi) = 0$, where $\xi = \omega_m t/2$ and $f(\xi)$ is π – periodic.

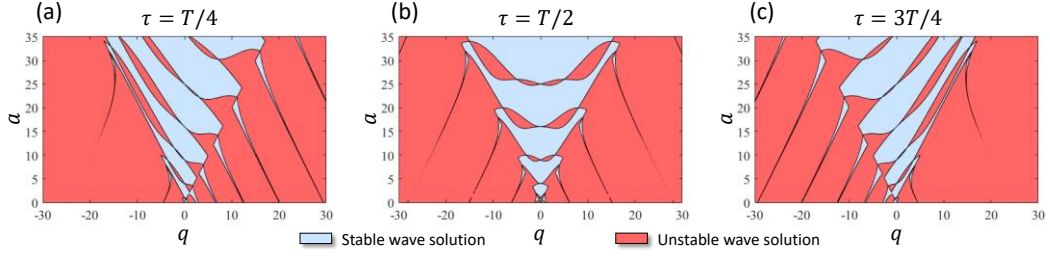


Figure 4: Illustration of the stability charts for (a) $\tau = T/4$, (b) $\tau = T/2$ and (c) $\tau = 3T/4$. The a –axis is defined by the a parameter which symbols the wave operation taking into account the effective permittivity, while the q –axis is defined by the q parameter which is proportional to the difference of ε_1 and ε_2 . Blue color: stable wave solutions, red: unstable wave solutions. Figure adapted from [18].

As also theoretically calculated it can be seen from the stability charts that for $q \rightarrow 0$ then: $a = n^2$, which is the parametric amplification condition of (66). Such property in the Hill’s stability chart is general regarding any time–periodic coefficient (meaning physically for any time–periodic permittivity function). This mathematical observation from the corresponding hypergeometric equations is in full agreement with the band structure properties and their symmetries as defined in the Section 2.7.

For $\tau = T/2$ the stability chart is symmetric, meaning that if $q \rightarrow -q$ the chart will not change. As the modulation becomes asymmetric, this asymmetry follows in the stability chart. Another important remark is that the density of stable regions is reduced as the absolute value of q increases. Even though the stability charts present the stable and unstable regions for every possible combination of the parameters (q , a and τ), the representative wave state parameters for the wave propagation problem form the geometric locus of a line, starting from $(0,0)$ point and continuing with an angle $\theta = \arctan 2(\varepsilon_1 + \varepsilon_2)/(\varepsilon_1 - \varepsilon_2)$ (similar Hill stability charts and geometric loci can be obtained for general periodic $\varepsilon(t)$). For $\theta = 90^\circ$, the geometric locus does

not intersect with any region with instability; this means obviously that for $\varepsilon_1 = \varepsilon_2$ the dispersion relation does not exhibit momentum gaps. As the angle θ deviates from 90° , the line intersects with instability regions. As the modulation depth increases, θ decreases and the size of the k -gaps are also increased. From (64) and Fig. 4, it is evident that a critical angle θ_c exists, below which the unstable regions occupy most of the space, and hence most wave numbers are not stable. This phenomenon is linked with the coexistence of unstable regions for the Meissner equation and is found for: $\alpha = \pm 2q$ resulting to $\theta_c = \arctan(2) \approx 63.43^\circ$ or $\theta_c = 180^\circ - \arctan(2) \approx 116.57^\circ$. These remarks provide us with a criterion for operating with parameters that lead to possibly denser stable region. More specifically, it yields a relation between ε_1 and ε_2 . When they are not of the same sign, the operating parameters are most likely to land in instability.

In Fig. 5 the stability chart with the corresponding geometric loci are shown regarding the same examples computed in fig. 3. For $\varepsilon_1 = 2\varepsilon_0$, $\varepsilon_2 = \varepsilon_0$ and $\tau = T/2$ the angle is $\theta_1 \approx 80.54^\circ$ (green line in the stability chart), while for $\varepsilon_1 = 3\varepsilon_0$, $\varepsilon_2 = \varepsilon_0$ and $\tau = T/2$ the angle is $\theta_2 \approx 75.96^\circ$ (blue line in the stability chart).

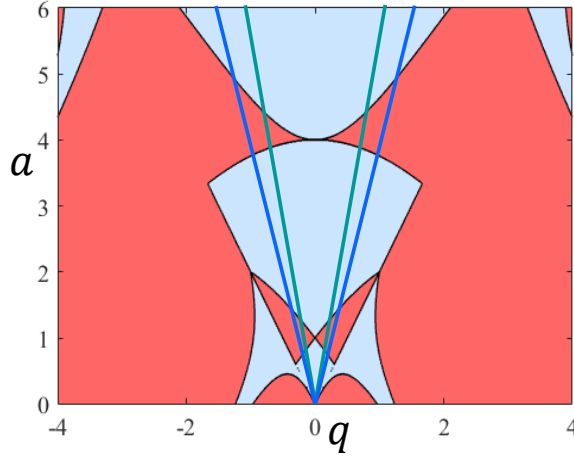


Figure 5: Stability chart with the geometric loci (lines) associated with the operating parameters in Fig. 3, with green (a) and blue (b) color respectively. Figure adapted from [18].

For the symmetric modulation ($\tau = T/2$) it is evident that wave propagation has the same dispersion when the values of ε_1 and ε_2 are swapped. This is directly linked with the fact that the stability chart is also symmetric. When this happens the operating line at the stability chart has an angle $\theta' = 180^\circ - \theta$. These operations correspond to the lines of Fig. 5 with angle of: $\theta_1' \approx 99.46^\circ$ (green line) and $\theta_2' \approx 104.04^\circ$ (blue line). Generally, as expected the exhibited k -gaps of the dispersion relations (see Fig. 3) correspond to the parametric amplification conditions at the stability chart. The n^{th} k -gap corresponds to the parametric-amplification operation: $\omega = n \frac{\omega_m}{2}$.

Chapter 3:

\mathcal{PT} –symmetry and time–variant media

In this chapter, the connection of \mathcal{PT} –symmetry and wave propagation in time–varying media is shown. This chapter starts with a brief introduction to \mathcal{PT} –symmetric wave systems and continues with their connection with waves under time–variation via a time–transitioning state matrix and the scattering by a parametrically amplifying time–Floquet slab via the appropriate scattering matrix conditions. This chapter is mainly based on the author’s published work [17,19].

3.1 Introduction to \mathcal{PT} –symmetry

Bender and Boettcher in [3] showed that a wide class of non–Hermitian Hamiltonians that commute with the \mathcal{PT} operator can exhibit real eigenvalues. Namely for a given eigenvalue problem:

$$\mathcal{H}|\psi(\mathbf{r})\rangle = \lambda|\psi(\mathbf{r})\rangle, \quad (67)$$

where \mathcal{H} is the Hamiltonian. Then if $[\mathcal{H}, \mathcal{PT}] = 0$, where \mathcal{P} is the parity operator ($\mathbf{r} \rightarrow -\mathbf{r}$) and \mathcal{T} is the time–reversal operator ($t \rightarrow -t$), the Hamiltonian can have real spectra even if it is not Hermitian. According to the

Schrödinger equation: $\mathcal{H} = -\frac{\hbar^2}{2m}\nabla^2 + V(r)$ and \mathcal{PT} –symmetry indicates that the potential obeys the condition: $V^*(-r) = V(r)$.

Despite the elegance of such theoretical results, quantum mechanics are built naturally by the Hermitian theory, meaning that such potentials that satisfy the \mathcal{PT} –symmetry condition may not be found in nature. This is not the case in the optical regime, where optical material technologies have advanced, and the presence of material gain and loss can be implemented resulting in optical devices with a distribution of gain and loss. Hence the developed \mathcal{PT} –theory can be directly applied to optics. One way to apply this theory to optics is by the application of the paraxial equation of the electric–field envelope U : $i\frac{\partial U}{\partial z} + \frac{1}{2k_0n_0}\frac{\partial^2 U}{\partial x^2} + k_0n(x)U = 0$ and its direct analogies with the Schrödinger equation leading to the \mathcal{PT} –symmetry condition: $n^*(-x) = n(x)$ of the refractive index [35]. Another approach is related to the eigenvalue and eigenmode problem formulated directly from Maxwell’s equations as shown in [36]:

$$\nabla \times \frac{1}{\varepsilon_r} \nabla \times \mathbf{H} = \frac{\omega^2}{c^2} \mathbf{H}. \quad (68)$$

where ε_r is the relative permittivity. Eq. (68) can be considered as the master equation and describes the electromagnetic fields. It defines an eigenvalue problem: $\mathcal{L}\mathbf{H} = \lambda\mathbf{H}$, where $\mathcal{L} = \nabla \times \frac{1}{\varepsilon_r} \nabla \times$ and $\lambda = \frac{\omega^2}{c^2}$ is the eigenvalue of the operator \mathcal{L} , which is proportional to the square of the frequency. This formulation resembles quantum mechanics problems, meaning that the eigenmodes and eigenvalues of \mathcal{L} give us the magnetic modes and their corresponding eigenfrequencies. It can be easily proved that for a real function

of $\varepsilon_r(\mathbf{r})$, \mathcal{L} is Hermitian which means that for two arbitrary fields \mathbf{H}_1 and \mathbf{H}_2 the inner product satisfies the relation: $\langle \mathbf{H}_1 | \mathcal{L} \mathbf{H}_2 \rangle = \langle \mathcal{L} \mathbf{H}_1 | \mathbf{H}_2 \rangle^\vee$. In addition, \mathcal{L} is linear and is positive semi-definite (all the eigenvalues ω^2 are nonnegative), hence the eigenvectors form an orthogonal basis^{vi}. For a complex permittivity, \mathcal{L} is non-Hermitian. If it is \mathcal{PT} -symmetric, which means that the operator commutes with the \mathcal{PT} operator: $[\mathcal{L}, \mathcal{PT}] = 0$ then $\varepsilon_r^*(-r) = \varepsilon_r(r)$ (same relation with the potential obtained for Schrödinger equation and the refractive index for the paraxial equation of diffraction [37]) and real eigenvalues can be observed. Additionally, between the real spectra and the complex ones there exists a degeneracy called exceptional point in which eigenvalues and eigenmodes collide. This point is the margin between propagating and evanescent modes.

Another way to check for such symmetries is through their scattering properties [38]. Consider an optical cavity coupled to a discrete set of scattering channels, where incoming waves enter as inputs and exit as outputs from the corresponding channels. The electric field satisfies the solution: $\nabla^2 E(\mathbf{r}) + \frac{n^2(\mathbf{r})\omega^2}{c^2} E(\mathbf{r}) = 0$ and has the form: $E(\mathbf{r}) = \sum_n [a_n e_n^{in}(\mathbf{r}, \omega) + b_n e_n^{out}(\mathbf{r}, \omega)]$, where $e_n^{in}(\mathbf{r}, \omega)$ and $e_n^{out}(\mathbf{r}, \omega)$ represent the input and output modes of the n^{th} channel. The input a_n and output b_n amplitudes are connected with the S matrix:

$$\sum_n S_{mn}(\omega) a_n = b_m. \quad (69)$$

^v The inner product is defined as: $\langle \mathbf{v} | \mathbf{u} \rangle = \int \mathbf{v}^* \mathbf{u} d^3 \mathbf{r}$.

^{vi} This is not the case if the electric field was considered: $\frac{1}{\varepsilon_r} \nabla \times \nabla \times \mathbf{E} = \frac{\omega^2}{c^2} \mathbf{E}$ (it is clear that the operator of the electric field is not self-adjoint).

The S matrix is symmetric due to the Lorentz reciprocity theorem regardless that the refractive index $n(\mathbf{r})$ is complex [39]. As noticed by [40] the time–reversal operator \mathcal{T} has the property: $\mathcal{T}e_n^{in}(\mathbf{r},\omega) = e_n^{out}(\mathbf{r},\omega^*)$ while for the parity operator \mathcal{P} (which mixes the channel functions and hence is a permutation matrix, but does not mix input with output channels and vice versa): $\mathcal{P}e_m^{in/out}(\mathbf{r},\omega) = \sum_n \mathcal{P}_{nm} e_n^{in/out}(\mathbf{r},\omega)$. If the cavity is \mathcal{PT} –symmetric then there exists a valid solution $(\mathcal{PT})E(\mathbf{r})$ at ω^* frequency: $(\mathcal{PT})E(\mathbf{r}) = \sum_n \left[(\mathcal{PT}a)_n e_n^{in}(\mathbf{r},\omega^*) + (\mathcal{PT}b)_n e_n^{out}(\mathbf{r},\omega^*) \right]$ which leads to the \mathcal{PT} –condition of the scattering matrix:

$$(\mathcal{PT})S(\omega^*)(\mathcal{PT}) = S^{-1}(\omega). \quad (70)$$

3.2 Exceptional points and operator symmetries under time–variance

Electromagnetic modes and the resulting parametric amplification at the momentum gaps from a time–periodic modulation were studied in the previous chapter. In this section, the simple case of a temporal material jump is considered and the connection between the parametric amplification phenomena with the exceptional–point theory will be established [17], without assuming any time–periodicity. In addition, the time–domain scattering problem is examined under the parity and time–reversal operators offering extra physical insights to this wave problem.

An exceptional point is an operating condition, in which (at least) two eigenvalues and eigenmodes collide and the operator \mathcal{L} (or a Hamiltonian \mathcal{H}) loses (at least) one of its dimensions and exhibits thus a degeneracy [41]. Such points are often connected with \mathcal{PT} –symmetric systems providing the

operating bounds of real spectra and signify interesting wave phenomena. Such theory can be extended to time-varying systems by formulating a state matrix, which models the time-evolutional behavior of the wave.

Let us assume that at $t = \tau$ there is an abrupt change in the medium from ε_1, μ_1 to ε_2, μ_2 that can be modelled by the scattering formulation of the previous section. The phase transmission matrix is defined as:

$$\mathbf{t}_\kappa(t) = \begin{bmatrix} e^{-i\frac{k}{\sqrt{\varepsilon_\kappa\mu_\kappa}}t} & 0 \\ 0 & e^{+i\frac{k}{\sqrt{\varepsilon_\kappa\mu_\kappa}}t} \end{bmatrix}, \quad (71)$$

where $\kappa = 1, 2$ and the matrix of coefficients is $\mathbf{C}(t) = [C_1, C_2]^T$, where $C_{1,2}$ are the amplitudes of $T_{1,2}(t)$. The coefficients matrix is thus:

$$\mathbf{C}(\tau') = \mathbf{t}_1(\tau)S_0^{-1}\mathbf{t}_2(\tau' - \tau)S_0\mathbf{C}(0) = \hat{H}(\tau')\mathbf{C}(0), \quad (72)$$

where S_0 is defined in (42), $\hat{H}(\tau') = \mathbf{t}_1(\tau)S_0^{-1}\mathbf{t}_2(\tau' - \tau)S_0$ is the time-transitioning state matrix of this system and τ' is the time moment of observation ($\tau' > \tau$). Since the problem neglects any conductivity the determinant of the time-transitioning state matrix is unit: $\det[\hat{H}(\tau')] = 1$ ^{vii}.

Its eigenvalues and eigenmodes are:

^{vii} If conductivities were considered the determinant would have been:

$$\det[\hat{H}(\tau')] = e^{-\left[\frac{\sigma_1}{\varepsilon_1}\tau + \frac{\sigma_2}{\varepsilon_2}(\tau' - \tau)\right]}.$$

$$\lambda_{\pm} = b \pm \sqrt{b^2 - 1}, \quad (73)$$

$$\mathbf{C}_+ = \begin{bmatrix} a \\ \lambda_+ + c \end{bmatrix}, \quad (74)$$

$$\mathbf{C}_- = \begin{bmatrix} a \\ \lambda_- + c \end{bmatrix}, \quad (75)$$

where:

$$b(k, \varepsilon_1, \mu_1, \varepsilon_2, \mu_2, \tau, \tau') = \cos \left[\frac{k}{\sqrt{\varepsilon_1 \mu_1}} \tau \right] \cos \left[\frac{k}{\sqrt{\varepsilon_2 \mu_2}} (\tau' - \tau) \right] - \frac{(\varepsilon_1 \mu_1 + \varepsilon_2 \mu_2)}{2\sqrt{\varepsilon_1 \mu_1 \varepsilon_2 \mu_2}} \sin \left[\frac{k}{\sqrt{\varepsilon_1 \mu_1}} \tau \right] \sin \left[\frac{k}{\sqrt{\varepsilon_2 \mu_2}} (\tau' - \tau) \right], \quad (76)$$

$$a = -\frac{i(\varepsilon_1 \mu_1 - \varepsilon_2 \mu_2)}{2\sqrt{\varepsilon_1 \mu_1 \varepsilon_2 \mu_2}} \sin \left[\frac{k}{\sqrt{\varepsilon_2 \mu_2}} (\tau' - \tau) \right] \exp \left[-i \frac{k}{\sqrt{\varepsilon_1 \mu_1}} \tau \right], \quad (77)$$

$$c = \exp \left[-i \frac{k}{\sqrt{\varepsilon_1 \mu_1}} \tau \right] \left[\frac{i(\varepsilon_1 \mu_1 + \varepsilon_2 \mu_2)}{2\sqrt{\varepsilon_1 \mu_1 \varepsilon_2 \mu_2}} \sin \frac{k}{\sqrt{\varepsilon_2 \mu_2}} (\tau' - \tau) - \cos \frac{k}{\sqrt{\varepsilon_2 \mu_2}} (\tau' - \tau) \right]. \quad (78)$$

Evidently the b parameter determines the energy transitions. The eigenvalues satisfy the condition: $\lambda_+ \lambda_- = 1$. The system supports two propagating modes when $|b| < 1$, as both eigenvalues are complex and unitary, and one evanescent and one parametrically amplifying for $|b| > 1$ as one is lower and the other is higher than unity. The special transition case: $|b| = 1$ is associated with exceptional points since the eigenvalues and their eigenmodes collide: $\lambda_+ = \lambda_- = \pm 1$ and $\mathbf{C}_+ = \mathbf{C}_-$.

A plot of the eigenvalue transitions is given in Fig. 6. In Fig. 6(a) the real part of the eigenvalues is shown as a function of the parameter b , while in Fig. 6(b) the position of the eigenvalues on the complex plane is presented (arrows showing the position of the eigenvalues as b changes values from a negative -3 to a positive value $+3$). The b parameter determines the energy conversions that occur as the wave takes energy from the modulation and vice versa and their overall energy–transition characteristics.

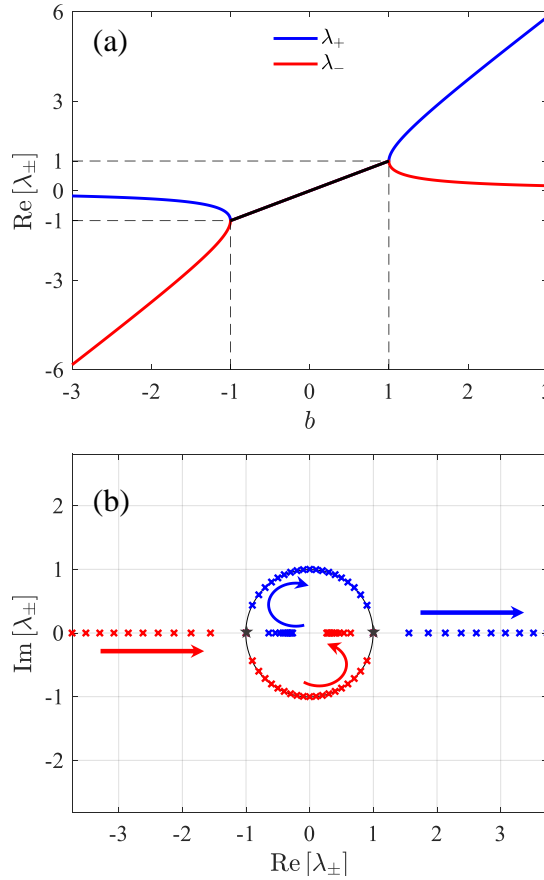


Figure 6: Graphical representations of the transitions of the eigenvalues of the time–transitioning state matrix of a system in which an abrupt change of material parameters occurs. (a) Evolution of the real part of the eigenvalues and (b) chart showing both real and imaginary part of the eigenvalues as b shifts values. For $|b| < 1$ the eigenvalues are complex and the waves represent propagation, for $|b| > 1$ the eigenvalues become real representing amplification, while at $|b| = 1$ exceptional

points are observed. The arrows at (b) show the quantitative change of the eigenvalues as b increases in values (from -3 to $+3$). Figure adapted from [17].

As proven in [16], a step temporal material jump results in a gain ratio of the electromagnetic energy density: $u_2/u_1 = (\varepsilon_1\mu_2 + \mu_1\varepsilon_2)/(2\varepsilon_2\mu_2)$, where $u = \varepsilon|\mathbf{E}|^2$, but this ratio is not the only quantitative value which defines the energy gain. Indeed, the energy interactions depend also on the time variables. As presented in the stability charts of Fig. 7, we fix $\frac{k}{\sqrt{\varepsilon_1\mu_1}}$ and $\frac{k}{\sqrt{\varepsilon_2\mu_2}}$, while τ and τ' vary in time. For a selected group of values (noted as red in Fig. 7) the system supports amplified modes, which means that the relative time that separates the initial knowledge of the field ($t=0$) the time of the change ($t=\tau$) and the time of observation ($t=\tau'$) play an important role also.

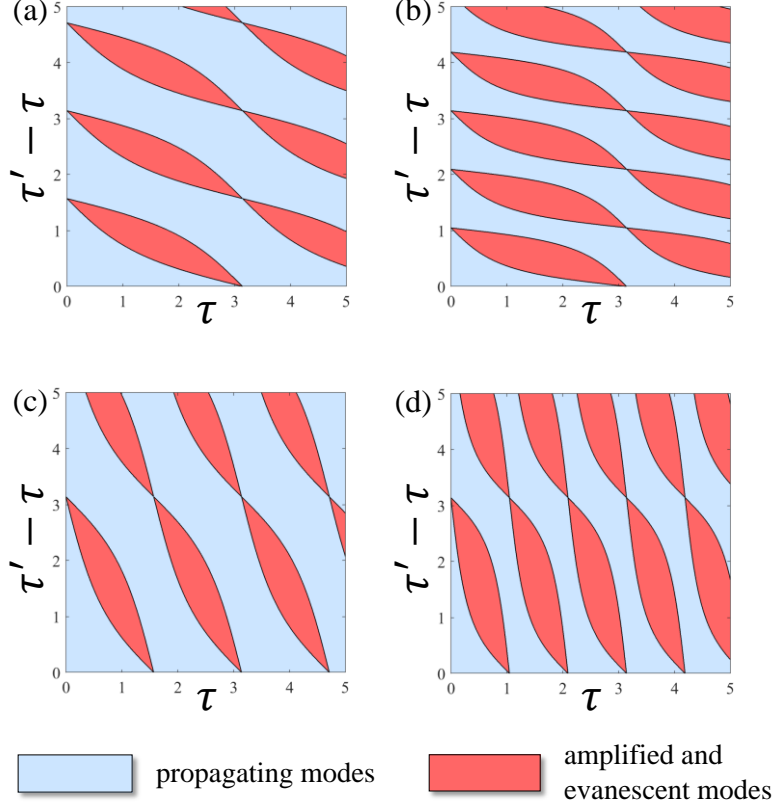


Figure 7: Stability charts for fixed values of $k/\sqrt{\varepsilon_1\mu_1}$ and $k/\sqrt{\varepsilon_2\mu_2}$: (a) $k/\sqrt{\varepsilon_1\mu_1} = 1$, $k/\sqrt{\varepsilon_2\mu_2} = 2$, (b) $k/\sqrt{\varepsilon_1\mu_1} = 1$, $k/\sqrt{\varepsilon_2\mu_2} = 3$, (c) $k/\sqrt{\varepsilon_1\mu_1} = 2$, $k/\sqrt{\varepsilon_2\mu_2} = 1$ and (d) $k/\sqrt{\varepsilon_1\mu_1} = 3$, $k/\sqrt{\varepsilon_2\mu_2} = 1$. Figure adapted from [17].

As seen also from Fig. 7, a swap of values for $\frac{k}{\sqrt{\varepsilon_1\mu_1}}$ and $\frac{k}{\sqrt{\varepsilon_2\mu_2}}$ results in a swap of the temporal axis of Fig. 7, τ and $\tau' - \tau$. This property of the stability charts indicates certain operator symmetries in time and in space.

The effect of the parity operator on the matrix of coefficients is: $\mathcal{PC}(t) = [C_2^*, C_1^*]^T$. For real eigenvalues, λ_{\pm} : $\mathcal{PC}_+ = \mathbf{C}_+$ and $\mathcal{PC}_- = \mathbf{C}_-$, while for complex λ_{\pm} : $\mathcal{PC}_+ = \mathbf{C}_-$ and $\mathcal{PC}_- = \mathbf{C}_+$. The physical interpretation of these results is intriguing. In the case of real eigenvalues (where the one mode is amplified and the other evanescent) the change of space is not going to affect the electromagnetic modes. On the contrary, for complex eigenvalues (where

both modes are propagating) the change of space is very important as the modes are interchanged.

The effect of the time–reversal operator on the matrix of coefficients is: $\mathcal{TC}(t) = [C_2, C_1]^T$. For time–varying homogeneous media, time–reversal is not the complex conjugate operator as it would have been in most of the stationary problems. The time–reversal relation of the state matrix is: $(\mathcal{TH}^{-1}(\tau')\mathcal{T})(\mathcal{TC}_{\pm}) = \lambda_{\pm}^{-1}(\mathcal{TC}_{\pm})$. $\mathcal{TH}^{-1}(\tau')\mathcal{T}$ is the new state matrix with \mathcal{TC}_{\pm} its corresponding eigenvectors. If the modulation is symmetric, meaning that starting from $t = 0$ we observe the waves at time: $\tau' = 2\tau$, where the medium has spent equal time having the two different wave parameter values then $\mathcal{TH}^{-1}(\tau')\mathcal{T}$ has interchanged eigenvalues and eigenvectors with $\hat{H}(\tau')$. This leads us to conclude that \mathcal{PT} –symmetry can be established since a double interchange of the eigenvalues and eigenmodes by the implementation of the \mathcal{PT} operator overtly brings back the system to its initial form. Such \mathcal{PT} –symmetric wave–states are exhibited without the presence of material gain and loss. The only necessary condition is a symmetric time–modulation of a dynamic medium.

3.3 \mathcal{PT} –symmetric scattering of a time–Floquet slab: Parametric amplification and bidirectional invisibility

In this subsection, a parametric time–Floquet system is considered which is modulated with a frequency twice that of the incident field. Such systems under specific conditions exhibit \mathcal{PT} symmetry. In full agreement with the \mathcal{PT} scattering theory, examples that exhibit coherent–perfect–absorption (CPA) or laser operations, phase transitions and anisotropic transmission resonances are provided [19].

Let us assume a special case of a time–Floquet system, which is a Mathieu medium that was first introduced in [42]. Such medium is subject to a uniform time–modulation of its refractive index: $u(t) = u_0 \sqrt{1 - 2m \cos(2\Omega t)}$, where $u_0 = \frac{\omega}{k}$ is the velocity of the medium when it is not modulated, m is the modulation depth and $\omega_m = 2\Omega$ is the modulation frequency. The scalar one–dimensional wave equation is:

$$\frac{\partial^2 \psi(x, t)}{\partial t^2} = u_0^2 [1 - 2m \cos(2\Omega t)] \frac{\partial^2 \psi(x, t)}{\partial x^2}, \quad (79)$$

where for an electromagnetic problem as modelled in chapter 2: ψ could be the electric displacement or the magnetic induction and the modulation of the refractive index would be in regards to the permittivity or the permeability respectively. A general solution of the form: $\psi(x, t) = X(x)T(t)$ is considered, which produces two coupled ordinary differential equations

$$\frac{d^2 X(x)}{dx^2} + k^2 X(x) = 0, \quad (80)$$

$$\frac{d^2 T(t)}{dt^2} + k^2 u_0^2 [1 - 2m \cos(2\Omega t)] T(t) = 0. \quad (81)$$

k^2 is a constant value (physically related to the square of the wave number of the medium) that defines the Sturm–Liouville problem. This eigenvalue problem is well known, and it provides the dispersion relation of the system (see chapter 2). The solution is a wave of the form

$$\psi(x, t) = \int \psi(x, t; k) dk. \quad (82)$$

Since the differential equation consists of periodic coefficients the Floquet theory forces the system to operate in discrete frequencies: $\omega + n(2\Omega)$, for $n \in \mathbb{Z}$. This simplifies eq. (82) since the dispersion relation is now discrete and for every n^{th} Floquet harmonic the solution corresponds to a wave number k_n .

We can write thus:

$$\psi(x, t) = \sum_n \psi(x, t; k_n). \quad (83)$$

Eq. (81) is the Mathieu differential equation of the form [43]:

$$\frac{d^2 w(z)}{dz^2} + [a - 2q \cos(2z)]w(z) = 0, \quad (84)$$

with a transformation of: $z = \Omega t$ and $a = \frac{k^2 u_0^2}{\Omega^2}$, $q = \frac{k^2 u_0^2 m}{\Omega^2}$. Similar with the analysis of the Hill's equation shown in chapter 2 a is a parameter regarding the operating frequency and q is a parameter analogous to the modulation depth m . The solution of this equation is a hypergeometric function the simplest form of a Hill's equation, which was first reported by the French mathematician Emile Leonard Mathieu, when solving the wave equation for an elliptical membrane moving through a fluid. This kind of differential equation has been of great scientific interest since then. The fundamental solutions of eq. (84) are $w_\alpha = e^{jvz} \varphi(z)$ and $w_\beta = e^{-jvz} \varphi(-z)$, where $\varphi(z)$ is a $\pi -$

periodic function and $v = \beta - j\mu$ is the characteristic exponent, which depends on the other parameters of the equation, namely, $v = v(\alpha, q)$. Taking this into account the solution is of the form

$$\psi(x, t) = A_1 w_\alpha(\Omega t) e^{jkx} + A_2 w_\alpha(\Omega t) e^{-jkx} + B_1 w_\beta(\Omega t) e^{jkx} + B_2 w_\beta(\Omega t) e^{-jkx}. \quad (85)$$

According to eq. (85) the medium allows as solutions waves with time-periodically varying amplitudes or standing waves which exponentially increase in time, depending on the stability of the Mathieu solutions, dictated by the imaginary part of the characteristic exponent v , which depends on the parameters α and q . A thorough analysis of Mathieu functions and their stability (which is similar to the one found for the Hill's equation in chapter 2) can be found in a plethora of textbooks, e.g., [43].

The system is studied in an operation which belongs in the first momentum gap with $\alpha = n^2$ and $n = 1$ (as found in chapter 2). In that case, the operating frequency ω is assumed fixed and the modulation frequency is tuned and satisfies the relation: $\Omega = \omega$, which corresponds to a modulation of the phase velocity at twice the signal frequency. This frequency modulation results in a Mathieu equation of the form

$$\frac{d^2 w(z)}{dz^2} + \kappa^2 [1 - 2m \cos(2z)] w(z) = 0, \quad (86)$$

where $K = \frac{\Omega}{u_0}$ and $\kappa = \frac{k}{K} \approx 1$. The solution of this Mathieu equation is unstable since it belongs to the first unstable region of the stability chart ([43], Chap. III, p. 40). This means that no matter how small the depth of modulation m

is, the dominant field solution is a time—exponentially increasing one. The parametric medium therefore behaves as an infinite space filled with material gain of parametric nature. To make it stable, one needs to balance the amplifying effects with losses, for instance, of radiative nature. This is feasible by considering a Mathieu slab of finite thickness surrounded by an unmodulated medium.

A Mathieu slab with length l is considered, subject to a fixed modulation depth $m \ll 1$. The surrounding medium is not modulated and is assumed to be free space [as shown in Fig. 8(a)].

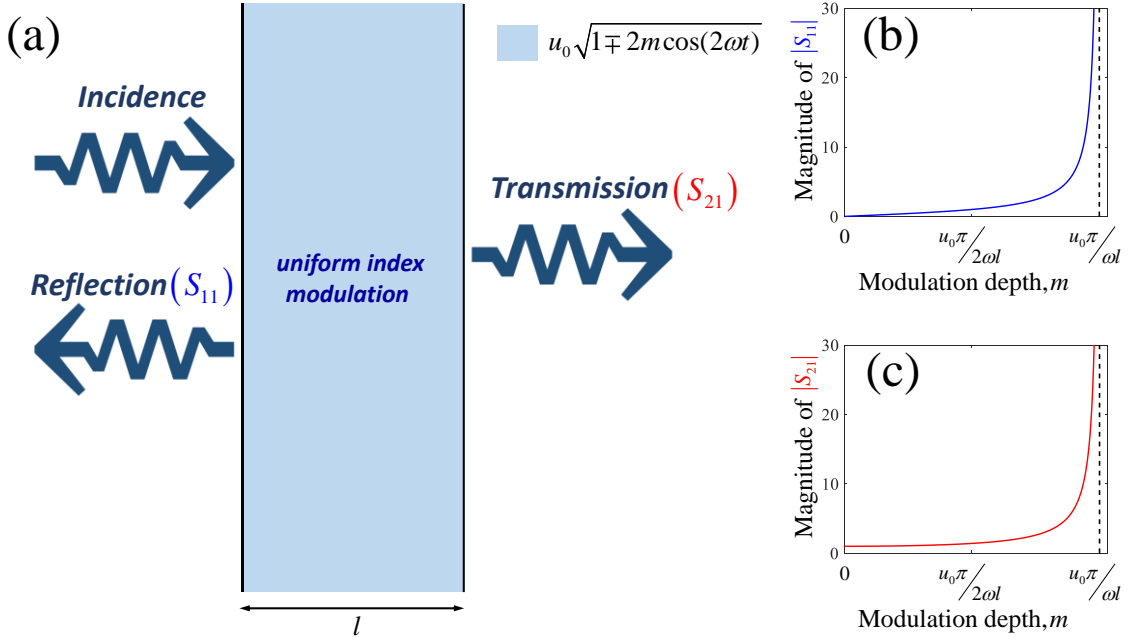


Figure 8: Scattering from a \mathcal{PT} —symmetric time—Floquet slab. (a) Graphic representation of a Mathieu slab with uniform time modulation of the refractive index, surrounded by free space; (b) diagram of the reflection coefficient as the modulation depth increases; (c) diagram of the transmission coefficient as the modulation depth increases. Modulation is assumed to be at twice the incident signal frequency. Figure adapted from [19].

A solution can be found in the form of

$$\psi = \sum_r \psi_r e^{j(2r+1+v')z}, \quad (87)$$

where $v = 1 + v'$, $v = \beta - j\mu$, $v' = \beta' - j\mu$ and $v = \frac{\omega}{\Omega}$. The resulting recursive relation is:

$$q_r \psi_{r-1} + \psi_r + q_r \psi_{r+1} = 0, \quad (88)$$

where $q_r = -\frac{m\kappa^2}{\kappa^2 - (2r+1+v')^2}$. The modulation is fixed: $\omega = \Omega$ and therefore $\kappa = 1 + \delta\kappa$ while $v \approx 1$. The only sufficient time-harmonics are the 0 and -1 Floquet harmonics of the field. Eq. (88) gives us the following system:

$$\mathbf{\Gamma}\mathbf{\Psi} = \begin{bmatrix} 1 & q_{-1} \\ q_0 & 1 \end{bmatrix} \begin{bmatrix} \psi_{-1} \\ \psi_0 \end{bmatrix} = 0, \quad (89)$$

where $q_0 \approx -\frac{m/2}{\delta\kappa - v'}$ and $q_{-1} \approx -\frac{m/2}{\delta\kappa + v'}$. For nonzero solutions $\det(\mathbf{\Gamma}) = 0$, which gives the condition

$$\delta\kappa^2 - v'^2 = \frac{m^2}{4}. \quad (90)$$

For κ real, $\delta\kappa$ has to be real, which forces v'^2 to be either real or imaginary (but not complex). An imaginary value would mean an unstable solution of the Mathieu equation located in the first unstable region of the Mathieu stability chart. A real solution in the special case of $v' = 0$ gives the result:

$$\delta\kappa = \pm \frac{m}{2}. \quad (91)$$

The solutions correspond to the ce_1 and se_1 Mathieu functions. Taking into account the condition of (91)

$$\frac{\psi_{-1}}{\psi_0} = \pm 1. \quad (92)$$

The incident field ψ_{inc} , the reflected one ψ_{ref} , the field distribution inside the slab ψ_{slab} and the transmitted field ψ_{t} are of the form

$$\psi_{\text{inc}} = e^{j(1+\beta')\Omega(t-x/u_0)}, \quad (93)$$

$$\psi_{\text{ref}} = r_0 e^{j(1+\beta')\Omega(t+x/u_0)} + r_{-1} e^{-j(1-\beta')\Omega(t+x/u_0)}, \quad (94)$$

$$\begin{aligned} \psi_{\text{slab}} = e^{j(1+\beta')\Omega t} & (Ae^{jK(1+\delta\kappa)x} + Be^{-jK(1+\delta\kappa)x} - Ce^{jK(1-\delta\kappa)x} - De^{-jK(1-\delta\kappa)x}) \\ & + e^{-j(1-\beta')\Omega t} (Ae^{jK(1+\delta\kappa)x} + Be^{-jK(1+\delta\kappa)x} + Ce^{jK(1-\delta\kappa)x} + De^{-jK(1-\delta\kappa)x}), \end{aligned} \quad (95)$$

$$\psi_{\text{t}} = t_0 e^{j(1+\beta')\Omega(t-x/u_0)} + t_{-1} e^{-j(1-\beta')\Omega(t-x/u_0)}. \quad (96)$$

The boundary conditions are assumed to involve the continuity of the total field ψ and the continuity of its derivative $\partial_x \psi$. The result in the form of a scattering matrix is thus [19]:

$$S = \begin{bmatrix} -j \tan[\omega l m / (2u_0)], & \sec[\omega l m / (2u_0)] \\ \sec[\omega l m / (2u_0)], & j \tan[\omega l m / (2u_0)] \end{bmatrix}. \quad (97)$$

The matrix is symmetric due to reciprocity. In Fig. 8(b), S_{11} which is the reflection from the 1st port ($S_{22} = -S_{11}$, where S_{22} is the reflection from the 2nd port), while in Fig. 8(c), $S_{21} = S_{12}$ which is the transmission, are illustrated versus the modulation depth. As a result of parametric amplification, the reflection and the transmission reach very high values when the modulation depth is increased away from zero. In particular, when the system is critically modulated with $m = \frac{u_0 \pi}{\omega l}$, both reflection and transmission go to infinite. This threshold value corresponds to the limit of the stability of the Mathieu solution. Above that value the radiative losses cannot compensate for the parametric gain of the slab and the fields are unstable. This phenomenon can be directly interpreted as a consequence of the \mathcal{PT} – symmetry breaking.

Indeed, the scattering matrix of (97) satisfies the \mathcal{PT} – symmetry condition (70): $(\mathcal{PT})S(\mathcal{PT}) = S^{-1}$. Because the scattering matrix of this time–Floquet slab satisfies \mathcal{PT} – symmetry it can be mapped directly to the established \mathcal{PT} – scattering theory developed in detail in [44,45]. The scattering matrix is of the form

$$S = \frac{1}{a} \begin{bmatrix} jb, & 1 \\ 1, & jc \end{bmatrix}, \quad (98)$$

where $a = \cos[\omega lm/(2u_0)]$, $b = -\sin[\omega lm/(2u_0)]$ and $c = \sin[\omega lm/(2u_0)]$ parametrize the scattering matrix. The transfer matrix M is thus defined as

$$M = \begin{bmatrix} \cos[\omega lm/(2u_0)], & -j \sin[\omega lm/(2u_0)] \\ -j \sin[\omega lm/(2u_0)], & \cos[\omega lm/(2u_0)] \end{bmatrix}. \quad (99)$$

$\det[M] = 1$, which is equivalent to the reciprocity condition. The CPA–laser condition which is defined by $a = 0$, is obtained for $m = \pm \frac{u_0 \pi}{\omega l}$, which is precisely the Mathieu condition of critical stability. The scattering matrix S_c corresponds to the scattering matrix with permuted outgoing channels

$$S_c = \begin{bmatrix} \sec[\omega lm/(2u_0)], & j \tan[\omega lm/(2u_0)] \\ -j \tan[\omega lm/(2u_0)], & \sec[\omega lm/(2u_0)] \end{bmatrix}. \quad (100)$$

It is easily checked that at the CPA–laser point, the eigenvalues of S_c are $\lambda_1 = 0$ and $\lambda_2 = \infty$, in full agreement with the usual nomenclature of \mathcal{PT} –symmetric systems [45]. At this special point, the system resonates, and the bounded charges of the medium cannot be considered macroscopically neutral anymore, as their sway is significant and generates a positive feedback system, leading to parametric lasing.

Following the analysis of [45], it is clear that the following “generalized unitarity relation” and the conservation relation also stand for this parametric system, namely:

$$S_{11}S_{22} = S_{21}^2 \left(1 - \frac{1}{|S_{21}|^2} \right), \quad (101)$$

$$\left| |S_{21}|^2 - 1 \right| = \pm |S_{11}| |S_{22}|. \quad (102)$$

$T = |S_{21}|^2 \geq 1$ and $R = |S_{11}| = |S_{22}|$, meaning that the phases of the right reflection and the left reflection always have a phase difference of π and the system has a similar behavior with nonlinear three-wave mixing systems in the undepleted pump approximation [46]. Eq. (102) implies: $T - R = 1$, which corresponds to the conservation relation imposed by \mathcal{PT} symmetry on the parametric time-Floquet system.

Anisotropic transmission resonances (ATRs) correspond to a condition for which the system conserves its flux ($T = 1$). Thus eq. (102) implies that an ATR is always associated with zero reflection from at least one of the ports (i.e., ATRs are associated with unidirectional or bidirectional invisibility). ATRs occur when $b = 0$ or $c = 0$, implying directly that transparency requires $m = 0$, i.e., no modulation. Therefore, the simple Mathieu slab supports only one trivial ATR.

In order to achieve nontrivial transparency a similar system with more degrees of freedom is considered. Assuming two different slabs with lengths l_A and l_B respectively operating with a modulation depth $m_A = \pm \frac{u_0 \pi}{\omega l_A}$ and $m_B = \mp \frac{u_0 \pi}{\omega l_B}$. We pair a percentage of these slabs with lengths $x l_A$ and $y l_B$, where $x, y \in [0, 1]$ and $x + y \leq 1$ (as shown in Fig. 9), keeping their modulation depths to the same value. Solving the scattering problem, the system is found to be equivalent to a single slab with effective length $l_{\text{eff}} = |x - y| l_{A,B}$ (in respect to either the first or the second slab) and the new scattering matrix is

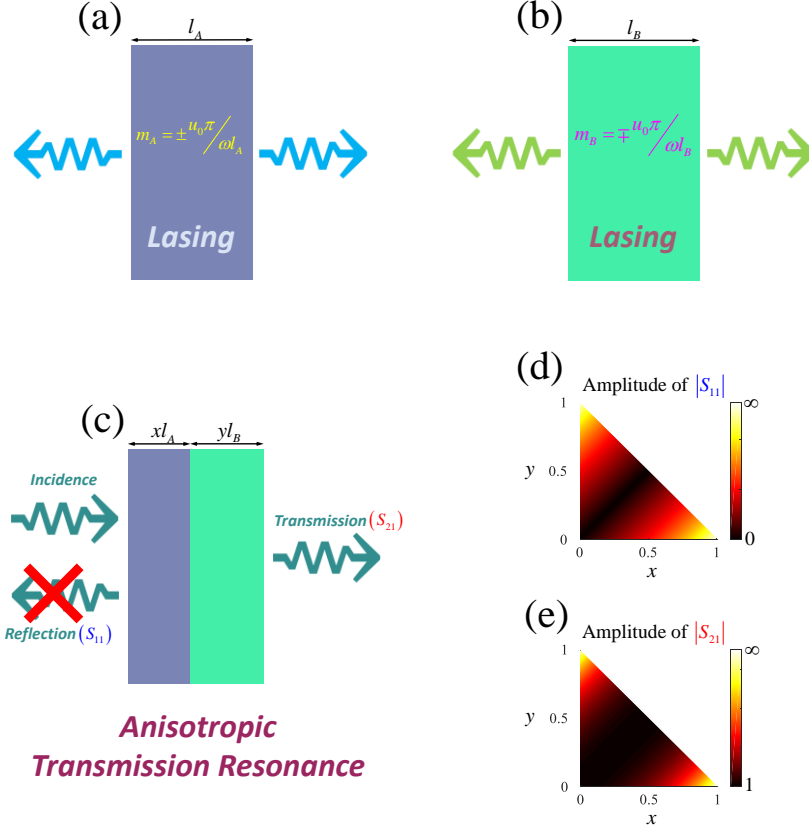


Figure 9: Anisotropic transmission resonance by pairing two out-of-phase time-Floquet slabs. (a) Lasing Mathieu slab with length l_A at its critical modulation depth. (b) Lasing Mathieu slab with length l_B at its critical modulation depth. (c) Composite Mathieu slab obtained by pairing a fraction of the two slabs in (a) and (b). (d) Reflection coefficient and (e) transmission coefficient of the system depicted in (c). ATRs occur when $x = y$ regardless of the length of l_A and l_B . Figure adapted from [19].

$$S = \begin{bmatrix} -j \tan[\text{sgn}(m_A)(x - y)\pi/2], & \sec[\text{sgn}(m_A)(x - y)\pi/2] \\ \sec[\text{sgn}(m_A)(x - y)\pi/2], & j \tan[\text{sgn}(m_A)(x - y)\pi/2] \end{bmatrix}. \quad (103)$$

$\text{sgn}(m_A)(x - y)$ can be replaced with $\text{sgn}(m_B)(y - x)$, since it gives the same result. This observation is directly linked with a hidden symmetry. Due to the critically tuned modulation of the slabs, the scattering matrix S again satisfies the \mathcal{PT} -symmetry relation (70): $(\mathcal{PT})S(\mathcal{PT}) = S^{-1}$. This is a somewhat

counterintuitive result since it stands for every possible value of x and y ($x, y \in [0,1]$ and $x + y \leq 1$), i.e., even when the composite slab is not mirror symmetric ($l_A \neq l_B$). The parameters of the transfer matrix are in this case:

$$a = \cos[\text{sgn}(m_A)(x - y)\pi/2], \quad b = -\sin[\text{sgn}(m_A)(x - y)\pi/2] \quad \text{and}$$

$$c = \sin[\text{sgn}(m_A)(x - y)\pi/2].$$

Contrary to the single Mathieu slab, in this more complex problem one finds non-trivial ATRs. These are obtained at specific values of the tuning parameters x and y . ATRs occur for $b = 0$ or $c = 0$, which give us: $y = x$. At these special points the structure becomes bidirectional invisible ($T = 1$ and $R = 0$). This bidirectional transparency arises because each slab compensates the “Mathieu” oscillations of the other, making the system transparent from both sides. A parametric study of the dependency of the scattering parameters on x and y as we move away from the ATR condition is given in Figs. 9(c)–9(e). In Figs. 9(d) and 9(e) the conditions $(x, y) = (1, 0)$ or $(x, y) = (0, 1)$ correspond to the CPA-laser points of a single Mathieu slab. Fig. 10 summarizes the geometric loci of the CPA-laser points and ATR points in the parameter space.

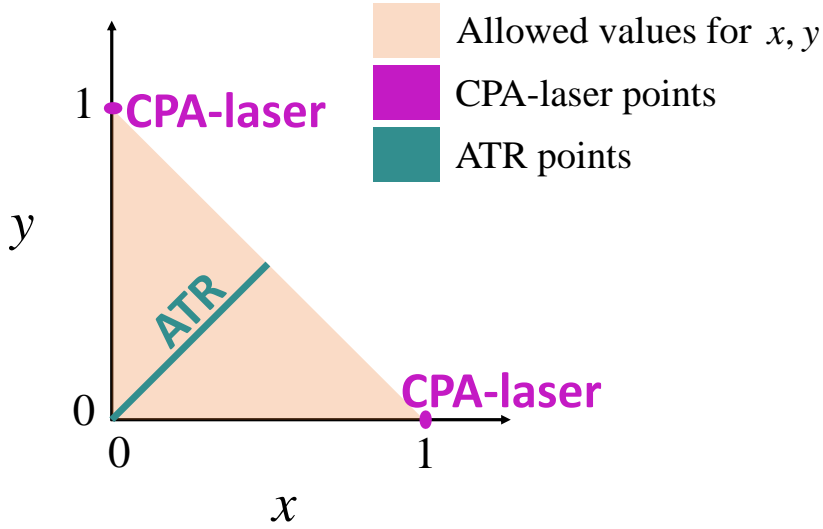


Figure 10: Graphic representation of the geometric loci of the special wave conditions of the scattering matrix. The CPA–laser points correspond to the bidirectional lasing; the ATRs correspond to the bidirectional invisibility. For parameters outside the shaded triangular region, the solution is unstable. Figure adapted from [19].

The analysis of this chapter has relied on the assumption that the modulation depth is always very small. Such assumption may be a subject of doubt. For this reason, a validation of the mathematical model is shown below, by providing full–wave numerical simulations using a homemade 1–D finite–difference in the time–domain (FDTD) code with open boundary conditions (Mur’s boundary conditions [47]). Such simulations do not involve any approximation on the Mathieu equations (the only approximations made are regarding the equation’s derivatives forced by the discretization of space and time while the dispersive error has been minimized to the minimum taking into account the Courant stability criterion, $u_0 \Delta t / \Delta x = 1$ [48]).

The special case of $y = 1 - x$, which lies at the hypotenuse of the triangle of Fig. 10, is considered. The investigated problem and the associated analytical results, which are subject of validation by FDTD are depicted in Fig. 11.

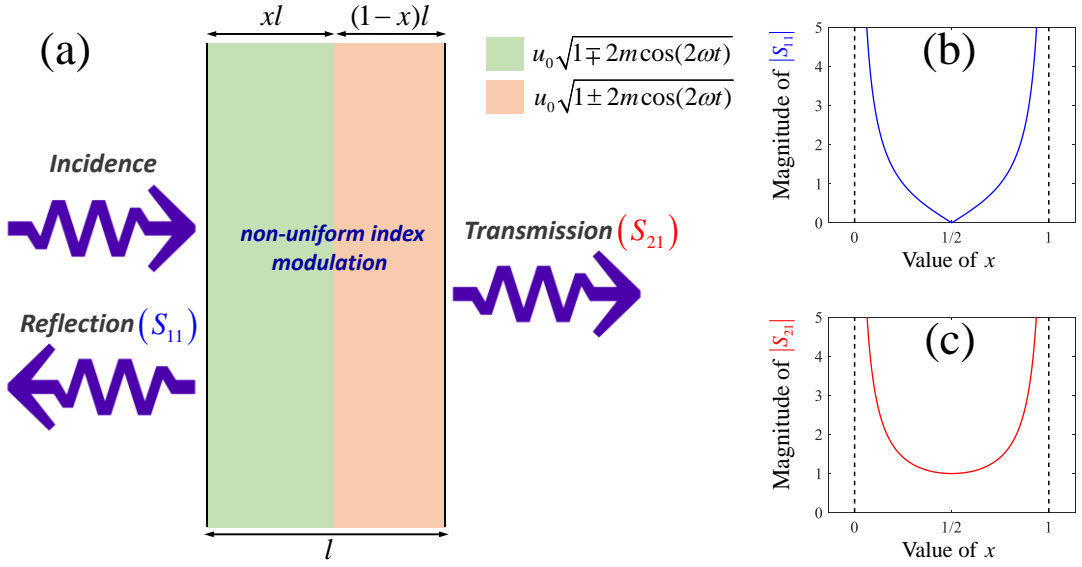


Figure 11: System under numerical FDTD investigation. (a) Special case of $y = 1 - x$. (b) Analytical predictions of reflection for $0 \leq x \leq 1$. (c) Analytical predictions of transmission for $0 \leq x \leq 1$. These curves are compared with the FDTD results in Fig. 13. Figure adapted from [19].

Fig. 12 shows the field oscillations at two observation points located in the unmodulated medium on each side of the slab. The blue curve corresponds to an observation on the incident side and the red on the transmission side. Figs. 12(a) and 12(b) correspond to $x=1$ for which the analytical predictions indicate a growing field (on both sides) which agrees to a bidirectional-laser operation. Figs. 12(c) and 12(d) correspond to $x = \frac{1}{2}$ the fields demonstrate unambiguously the transparent effect of the ATR operation (which was predicted analytically for such a choice of x).

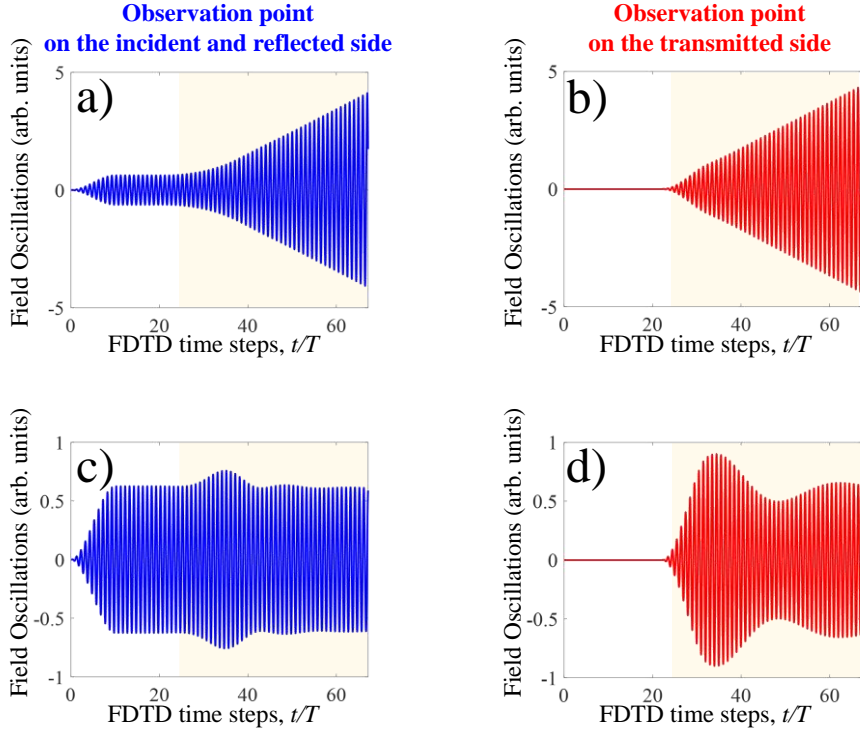


Figure 12: Wave dynamic oscillations from the FDTD simulations at a point at the incidence and the reflection side of the slab (blue) and at a point at the transmitted side (red). (a,b) Oscillations corresponding to the bidirectional lasing condition, $\chi = 1$. (c,d) Oscillations corresponding to the ATR, $\chi = 1/2$. Figure adapted from [19].

In Fig. 13 is presented a direct comparison between the analytically predicted and simulated magnitudes of reflectance and transmittance. The numerical results are in perfect agreement with the analytic results.

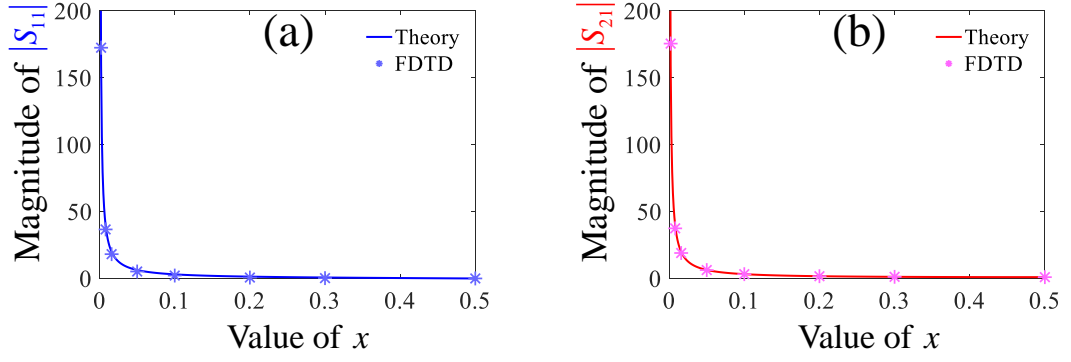


Figure 13: Comparison between FDTD and analytical model. Magnitude of (a) reflection and (b) transmission for the slab of Fig. 11 as the value of x varies. Figure adapted from [19].

Further, in Fig. 14 chronophotographs are provided of the “Mathieu” wave pattern inside a \mathcal{PT} –symmetric slab under an ATR operation with total length of 10λ , where λ is the wavelength and the critical depth of modulation is $m = \frac{u_0\pi}{\omega 10\lambda}$. The chronophotographs cover a full period of the incident signal after the steady state solution has been reached. The field profile inside the slab undergoes a beating characteristic of related to the Mathieu solutions (two beatings cycles per incident period).

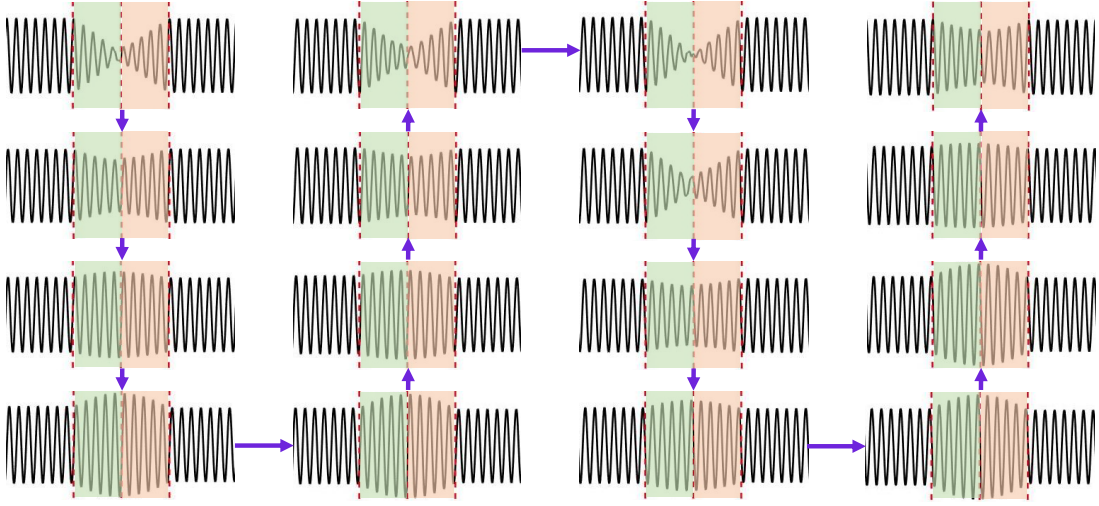


Figure 14: FDTD chronophotographs of the wave pattern at steady state for the \mathcal{PT} – symmetric Mathieu slab of Fig. 13 operating at the ATR condition. The time sequence of the snapshots is given by the arrows, and snapshots are separated by $\Delta t = \frac{\pi}{8\omega}$. The overall sequence corresponds to one period of the incident signal. Figure adapted from [19].

For additional simulation results and motion pictures of the FDTD simulations see supplementary material of [19].

Chapter 4:

Studies on time–variant resonant systems

In this chapter, studies regarding resonant systems are shown for nonstationary conditions. A brief introduction is given to the coupled–mode theory which is often used to model physical systems of resonant characteristics [20]. The corresponding theoretical background to study time–variant systems based on the coupled–mode theory is then addressed [49]. The time–variant resonant systems are shown in the last part of the chapter to impart interesting effective medium properties such as zero–index of refraction and non–reciprocal amplification [21,22].

4.1 Coupled–mode theory

Coupled–mode theory has been widely studied to investigate resonant systems from optics to acoustics [20,50]. Taking into account Maxwell’s equations or the acoustic equations the system can be casted into the form

$$i\hat{\zeta} \cdot \partial_t |\Psi\rangle = \mathcal{H} |\Psi\rangle, \quad (104)$$

where $|\Psi\rangle = [\mathbf{E}, \mathbf{H}]^T$ for electromagnetics or $|\Psi\rangle = [p, \mathbf{u}]^T$ for acoustics (indicating pressure and particle velocity). $\hat{\zeta}$ is a tensor, which depends on the material parameters and is most often invertible. For electromagnetics it is

$$\hat{\zeta} = \begin{bmatrix} \varepsilon \mathbb{I} & \mathbf{0} \\ \mathbf{0} & \mu \mathbb{I} \end{bmatrix}, \quad (105)$$

while for acoustics it is

$$\hat{\zeta} = \begin{bmatrix} \frac{1}{K_0} & 0 \\ 0 & \rho_0 \mathbb{I} \end{bmatrix}, \quad (106)$$

where K_0 is the bulk modulus and ρ_0 is the material density. The tensor can be appropriately modified for anisotropic media. For lossless media, the tensor is Hermitian ($\hat{\zeta} = \hat{\zeta}^\dagger$). \mathcal{H} is an operator which is defined for Maxwell's equations as

$$\mathcal{H} = \mathbf{i} \begin{bmatrix} \mathbf{0} & \nabla \times \\ -\nabla \times & \mathbf{0} \end{bmatrix}, \quad (107)$$

while for acoustics it is

$$\mathcal{H} = -\mathbf{i} \begin{bmatrix} 0 & \nabla \cdot \\ \nabla & 0 \end{bmatrix}. \quad (108)$$

The operator is Hermitian iff $\langle \Psi_a | \mathcal{H} \Psi_b \rangle = \langle \mathcal{H} \Psi_a | \Psi_b \rangle$, for two arbitrary solutions of the same boundary-condition problem. It can be proven that the operator is indeed Hermitian for systems made of finite localized resonances, for lossless

structures and for any isolated two–port system. Assuming a Hermitian system, the resonant frequencies are real (their set could be either continuous or discrete depending on the system), while its eigenwaves are orthogonal, e.g.

$$\text{for } n \neq m, \quad \int \varepsilon \mathbf{E}_n^* \cdot \mathbf{E}_m dV = \int \mu \mathbf{H}_n^* \cdot \mathbf{H}_m dV = 0 \quad \text{or} \\ \int \frac{1}{K_0} p_n^* p_m dV = \int \rho_0 \mathbf{u}_n^* \cdot \mathbf{u}_m dV = 0.$$

For the same eigenfrequency ω_n two modes exist. The one on the positive direction $|\psi_n^+\rangle = [\mathbf{E}_n, \mathbf{H}_n]^T$ or $[p_n, \mathbf{u}_n]^T$ and the one on the negative direction $|\psi_n^-\rangle = [\mathbf{E}_n^*, -\mathbf{H}_n^*]^T$ or $[p_n^*, -\mathbf{u}_n^*]^T$.

A direct consequence of the orthogonality of such Hermitian systems is that in the electromagnetic case the electric–field energy stored is the same with the magnetic–field energy which is stored $\int \varepsilon |\mathbf{E}_n|^2 dV = \int \mu |\mathbf{H}_n|^2 dV$ and analogously for the acoustic case the potential energy of the wave mode which is stored in the acoustic pressure is the same with the kinetic energy stored in the motion of the medium’s particles $\int \frac{1}{K_0} |p_n|^2 dV = \int \rho_0 |\mathbf{u}_n|^2 dV$.

The wave system is then investigated as a first order time–derivative system with added perturbations. Next, we provide a simple example working with such first order equations.

If a traveling wave basis is assumed the wave distribution may take the form

$$|\Psi\rangle = \alpha_+(\mathbf{r}, t) |\psi_n^+\rangle e^{-i\omega_n t} + \alpha_-(\mathbf{r}, t) |\psi_n^-\rangle e^{-i\omega_n t}. \quad (109)$$

To proceed further to the coupled–mode analysis, important approximations shall be made for eq. (109). As advocated by a general assumption of weak coupling the α_+ and α_- envelopes are presumed to be slowly varying in space

and time. Plugging eq. (109) into eq. (104) and projecting with the bra $\langle \psi_n^\pm |$ the resulting equations are

$$\partial_t \alpha_+ + (\mathbf{v}_g \cdot \nabla) \alpha_+ = -g^* \partial_t \alpha_-, \quad (110)$$

$$\partial_t \alpha_- - (\mathbf{v}_g \cdot \nabla) \alpha_- = -g \partial_t \alpha_+, \quad (111)$$

where $g = \frac{\langle \psi_n^- | \hat{\psi}_n^+ \rangle}{\langle \psi_n^+ | \hat{\psi}_n^+ \rangle}$, $\mathbf{v}_g = \frac{2\mathbf{F}_e}{\langle \psi_n^+ | \hat{\psi}_n^+ \rangle}$ with $\mathbf{F}_e = \int \text{Re}(\mathbf{E}_n^* \times \mathbf{H}_n) dV$ or $\int \text{Re}(p_n^* \mathbf{u}_n) dV$.

The g parameter, which has an upper bound of $|g| \leq 1$, characterizes the homogeneity of the medium and the localization of the field in the resonators. If the chosen medium has no defects or cavities then it reaches extinction ($g = 0$), which means that there is no coupling between the two envelopes α_+ and α_- . If a defect is placed the wave propagation problem supports a back scattered mode and the total field is localized. Taking a closer look at \mathbf{v}_g , we find that aside from the normalization, it is proportional to \mathbf{F}_e , which describes the power flow over the integral. This directional flux should satisfy the solenoidal field condition in the absence of active elements, due to the general continuity equation. The resulting algebra for the computation of \mathbf{v}_g provides a quantitative parameter that characterizes the effective group velocity of the wave.

Further to the slowly envelope analysis, scattering problems can be easily modeled with these first order approximations. Let us assume an one-dimensional structure from $x=0$ to $x=L$ as depicted in Fig. 15, forming an on-channel resonance system.

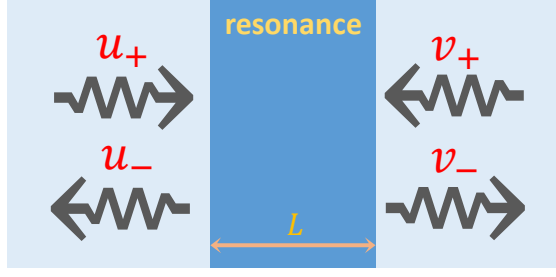


Figure 15: Schematic representation of a one-dimensional sound resonant system with input and output wave signals from the left and right directions. Figure adapted from [20].

The notations u_+ and v_+ are used to symbolize the incoming signals on the left and the right side and u_- , v_- the outgoing signals on the left and the right side, respectively. Utilizing the analysis based on the traveling waves and approximating the wave distributions with averages we get: $\alpha_{\pm} \approx (u_{\pm} + v_{\mp})/2$. Using finite difference approximations (which are valid approximations for weak coupling problems or strong inhomogeneities with considerably small length), we write: $\partial_x \alpha_{\pm} \approx (v_{\mp} - u_{\pm})/L$ and $\partial_t \alpha_{\pm} \approx -i(\omega - \omega_n)(u_{\pm} + v_{\mp})/2$.

The mathematical model assumes an average of the wave distributions, where the mode traveling in the positive direction is the average of the signal that enters from the left and the signal that leaves the structure from the right direction. In analogous way, the traveling mode at the negative direction is the average of the signal that enters from the right and leaves from the left. Additionally, the space derivative is modeled as a first order approximation. These assumptions are valid under weak coupling approximation, which assumes that the energy of the mode decays exponentially and is true for large quality factors. The scattering matrix is thus

$$S = \frac{1}{1 - \frac{i(\omega - \omega_n)}{\gamma}} \begin{bmatrix} \frac{ig(\omega - \omega_n)}{\gamma} & 1 \\ 1, & \frac{ig^*(\omega - \omega_n)}{\gamma} \end{bmatrix}, \quad (112)$$

where $\gamma = \mathbf{v}_g \cdot \hat{n}/L$ is the radiative delay rate and \hat{n} is the unit vector in the direction of the wave propagation. Let us consider the acoustic problem of reflection and transmission of a water slab amid air. Water has speed velocity $c = 1498$ m/s and density $\rho_0 = 1000$ kg/m³, whereas air has $c = 343$ m/s and $\rho_0 = 1.225$ kg/m³. The slab has a length of $L = 0.2$ m. Such scattering problem can be solved analytically, by considering plane waves and boundary conditions at the boundaries of the water slab and the radiation conditions at infinity.

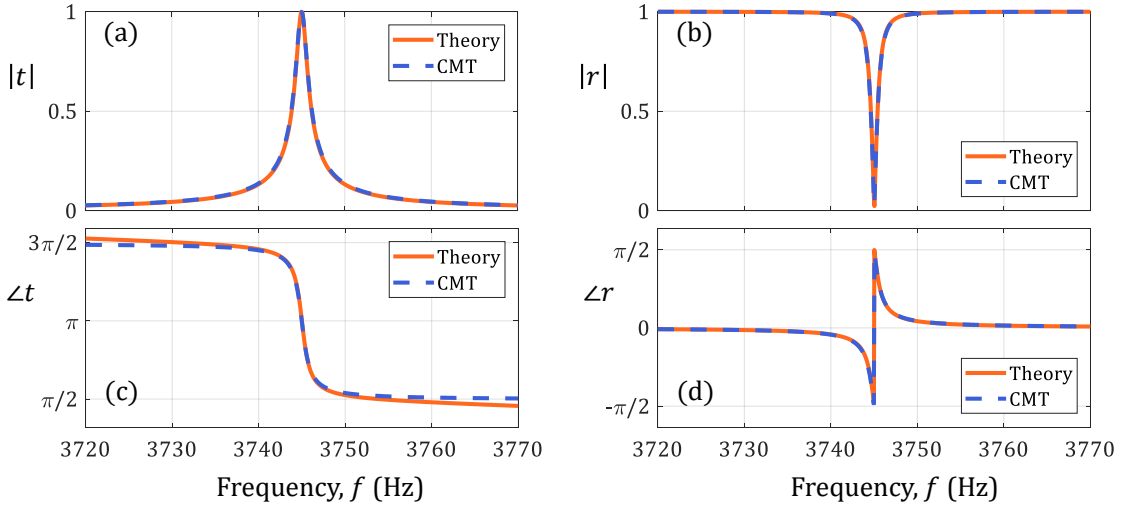


Figure 16: Numerical example of a 20 cm-thick water slab amid air. (a) Graphical plot and comparison of theory and CMT of the transmission amplitude, (b) graphical plot and comparison of theory and CMT of the reflection amplitude, (c) graphical plot and comparison of theory and CMT of the transmission phase and (d) graphical plot and comparison of theory and CMT of the reflection phase of the wave propagation problem under examination. Figure adapted from [20].

The obtained analytical solutions match perfectly the prediction obtained from coupled-mode theory. As depicted in Fig. 16(a) and (b) the resonant frequency is $f_n = 3745$ Hz, corresponding to a resonant mode occurring under the condition: $L = \lambda/2$. The dominant mode is odd, hence the transmission has a π phase as seen in the phase diagrams [Fig. 16(c), (d)]. The conservation of energy stands, i.e. $|r|^2 + |t|^2 = 1$, where r is the reflection coefficient and t is the transmission coefficient. Furthermore, we obtain the typical Lorentzian shape-line consistent with the prediction of CMT.

Such CMT techniques can be very useful while studying resonant systems either by matching experimental results or as a basis to study complex wave nonlinear or nonstationary systems. In the latter case, one has to fully solve the eigenvalue problem, including the scattering part, but only for one frequency, i.e. the resonance frequency of the system. Then, the scattering response of the system at any other frequencies around the resonant can be deduced from CMT. After that, CMT can be used as an orthogonal basis for implementing several perturbations and solve a more complicated problem. Several examples can be found in the literature [20,50].

4.2 The mathematical foundations of the Hamiltonian formalism under time-periodicity

As was previously shown electromagnetic and generally resonant systems can be casted into a Hamiltonian formalism. In this subsection we revise the mathematical foundations necessary in regard to such systems with time periodic Hamiltonians [49]. Let us assume a general case

$$i\partial_t |\Psi(\mathbf{r}, t)\rangle = \mathcal{H}(t) |\Psi(\mathbf{r}, t)\rangle, \quad (113)$$

where $|\Psi\rangle$ represents the modes, $\mathcal{H}(t) = \mathcal{H}(t+T)$ is the Hamiltonian, which is periodic with period T , with modulation frequency $\omega_m = 2\pi/T$ and any weighting operators or \hbar are normalized. Assuming a solution: $|\Psi(\mathbf{r}, t)\rangle = u(\mathbf{r}, t)e^{-i\omega_q t}$, with $u(\mathbf{r}, t) = u(\mathbf{r}, t+T)$ then

$$(\mathcal{H}(t) - i\partial_t)u(\mathbf{r}, t) = \omega_q u(\mathbf{r}, t). \quad (114)$$

If $u(\mathbf{r}, t)$ is square integrable and ω_q is real, the solution is a steady bound state and ω_q is called the quasifrequency (or quasienergy) of the state. Furthermore, the time–translation operator $\tau(\Delta t)$ defined as

$$\tau(\Delta t)|\Psi(\mathbf{r}, t + \Delta t)\rangle = |\Psi(\mathbf{r}, t)\rangle, \quad (115)$$

has the property $[\mathcal{H}(t) - i\partial_t, \tau(nT)] = 0$, for $n \in \mathbb{Z}$ and hence forms a symmetry group. All irreducible representations are one–dimensional for this time–translation group at any nT . Assuming the steady state solution

$$\tau(nT)|\Psi(\mathbf{r}, t)\rangle = e^{in\omega_q T}|\Psi(\mathbf{r}, t)\rangle. \quad (116)$$

It is clear that the irreducible representation is given by $e^{in\omega_q T}$ which depends on the quasifrequency. Hence one may find steady state solutions corresponding to an irreducible representation of the symmetry group of the Hamiltonian and consequently to its quasifrequency. This is similar to the

stationary case. For a time-invariant Hamiltonian the time-translation operator $\tau(t)$ forms symmetry groups of the Schrodinger type equation for any $t \in \mathbb{R}$. A stationary state can be defined thus as one which belongs to the time-translation group of $\tau(t)$ and the frequency (or energy) eigenvalue characterizes the irreducible representation.

Next, in order to form the Hilbert space necessary to study time-periodic Hamiltonians let us remind that a linear space consisting of all square-integrable functions is a Hilbert space \mathcal{R} where the range of integration is the entire configuration space [51]. While the Hilbert space \mathcal{T} consists of all possible periodic functions of time with period T , where $\int_{-T/2}^{T/2} |g(t)|^2 dt < \infty$. Obviously, $\exp(in\omega_m t)$, for $n \in \mathbb{Z}$ forms a complete orthogonal set in \mathcal{T} space.

$\mathcal{R} + \mathcal{T}$ space consists of all possible functions $f(\mathbf{r}, t) = f(\mathbf{r}, t + T)$ for which $\int_{-T/2}^{T/2} \int |f(\mathbf{r}, t)|^2 d\mathbf{r} dt < \infty$. The inner product of the functions $f(\mathbf{r}, t)$ and $g(\mathbf{r}, t)$ in $\mathcal{R} + \mathcal{T}$ is defined as

$$\langle f(\mathbf{r}, t) | g(\mathbf{r}, t) \rangle = \frac{1}{T} \int_{-T/2}^{T/2} \int f^*(\mathbf{r}, t) \cdot g(\mathbf{r}, t) d\mathbf{r} dt. \quad (117)$$

If $f_p(\mathbf{r})$ for $p \in \mathbb{Z}^>$ forms a complete orthogonal set in \mathcal{R} then $u_{pn}(r, t) = f_p(r, t) \exp(in\omega_m t)$ for $n \in \mathbb{Z}$, forms a complete orthogonal set in $\mathcal{R} + \mathcal{T}$. Furthermore, any linear Hermitian operator in \mathcal{R} or \mathcal{T} is also one in $\mathcal{R} + \mathcal{T}$. For example, $-i\partial_t$ is a linear Hermitian operator in \mathcal{T} , hence is also in $\mathcal{R} + \mathcal{T}$.

Let us assume $\mathcal{L} = \mathcal{H}(t) - i\partial_t$ and the solution $u(\mathbf{r}, t)$ located in $\mathcal{R} + \mathcal{T}$. It is evident that \mathcal{L} is analogous to the Hamiltonian in a stationary system, since the quasifrequencies and the steady states are the eigenvalues and the eigenfunctions of \mathcal{L} . Moreover, \mathcal{L} is Hermitian resulting in real quasifrequencies and orthogonal eigenfunctions. Additionally, if ω_q and $u(\mathbf{r}, t)$ are a solution of the steady-state eigenvalue equation (114) then clearly

$$\omega'_q = \omega_q + n\omega_m, \quad u'(\mathbf{r}, t) = u(\mathbf{r}, t)e^{in\omega_m t}, \quad (118)$$

are a solution for any $n \in \mathbb{Z}$. All solutions of (118) are physically equivalent, hence the temporal Brillouin zone can be defined

$$E - \frac{\omega_m}{2} < \omega_q < E + \frac{\omega_m}{2}, \quad (119)$$

where E can be any real value. Eq. (119) is in full agreement with the dispersion relations temporal zone of time–Floquet electromagnetic media in Section 2.7. For further mathematical analyses regarding such systems evolving their variational principle, the Hellmann–Feynman theorem and the perturbation theory one can consult the work of Sambe in [49].

4.3 Zero refractive index in time–Floquet acoustic metamaterials

In this subsection, we demonstrate how a particular time–modulation can impart zero refractive index properties to an acoustic resonant metamaterial. Zero refractive index metamaterials have been on the front line of wave physics research for their unique wave manipulation properties and application

potentials [52–56]. Remarkably, in such exotic materials, time–harmonic fields have an infinite wavelength and do not exhibit any spatial variations in their phase distribution. This unique feature can be achieved by forcing a Dirac cone to the center of the Brillouin zone (Γ point), as previously predicted and experimentally demonstrated in time–invariant metamaterials by means of accidental degeneracy between three different modes [57,58,66,67,58–65].

Here, we propose a different approach that enables true conical dispersion at Γ with twofold degeneracy and generates zero index properties. We break time–reversal symmetry and exploit a time–Floquet modulation scheme to demonstrate a time–Floquet acoustic metamaterial with zero refractive index. This behavior, predicted using stroboscopic analysis, is confirmed by full–wave finite element simulations.

Let us consider the metamaterial represented in Fig. 17. This Floquet acoustic crystal has already been discussed in another context for its unique and exotic topological properties [68]. It forms a hexagonal lattice constructed by coupled acoustic trimers connected together along the hexagonal bonds via small rectangular channels. The medium filling the acoustic crystal is silicone rubber RTV–602, which is a low loss material with density $\rho_0 = 990 \text{ kg m}^{-3}$ and compressibility $\beta_0 = 9.824 \cdot 10^{-10} \text{ Pa}^{-1}$. The surrounding medium could be considered a denser material like steel, which imposes hard wall acoustic boundary conditions to the rubber (large impedance mismatch), and the cavity diameter is 1 cm with a thickness of 3 mm. Following [69], at low frequencies, the trimer can be viewed as a lumped element acoustic pressure network featuring three parallel coupled LC resonators, with the acoustic capacitance of $C_0 = \beta_0 V_0$, where V_0 is the volume; i.e., we operate the system way below the first dipolar resonant frequency of the individual cavities (circa 60 kHz). We modulate periodically in time the acoustic capacitance of each cavity as shown in Fig. 17(a) at an angular frequency $\omega_m = 2\pi f_m = 2\pi/T$, with a modulation

depth of δC and a phase φ_m^i different for each symmetric cavity $i \in \{1, 2, 3\}$, $\varphi_m^1 = 0$, $\varphi_m^2 = -2\pi/3$ and $\varphi_m^3 = 2\pi/3$ as shown in Fig. 17(a) so that the modulation will convey an effective spin to the trimer and break time–reversal symmetry, while Fig. 17(b) depicts the complete periodic structure. The inner trimer coupling is equal to k while the outer coupling is J . Such systems may be implemented using piezoelectric materials or active control (see Appendix C and [70]).

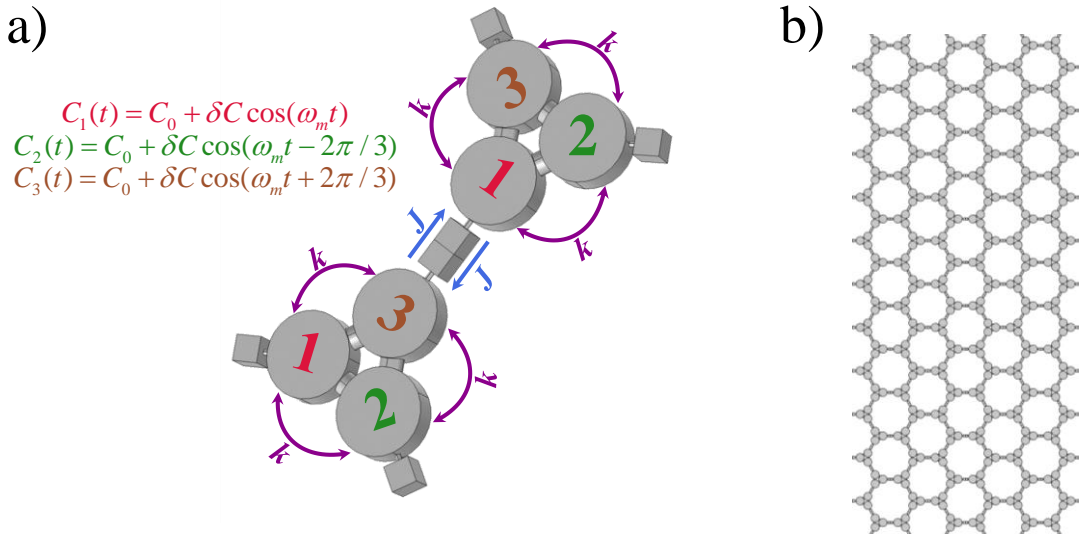


Figure 17: The considered spatiotemporal periodic structure. (a) The unit cell of the periodic structure with the time modulation of the acoustic capacitance and the internal and external coupling coefficients. (b) The complete periodic structure from a macroscopic point of view. The grey domains are filled with silicone rubber. The external boundaries are hard wall boundary conditions. Figure adapted from [21].

In the case of $\delta C = 0$, the system does not vary in time. The band structure of this case is shown in Fig. 18, where k and J correspond to the internal and external coupling coefficients of the structure [as indicated in Fig. 17(a)]. From a standard tight binding model, it is straightforward to show that the distances

of the bands at $\mathbf{k}=0$ are directly dependent on the relative values of the internal and external coupling coefficients, as shown in the figure.

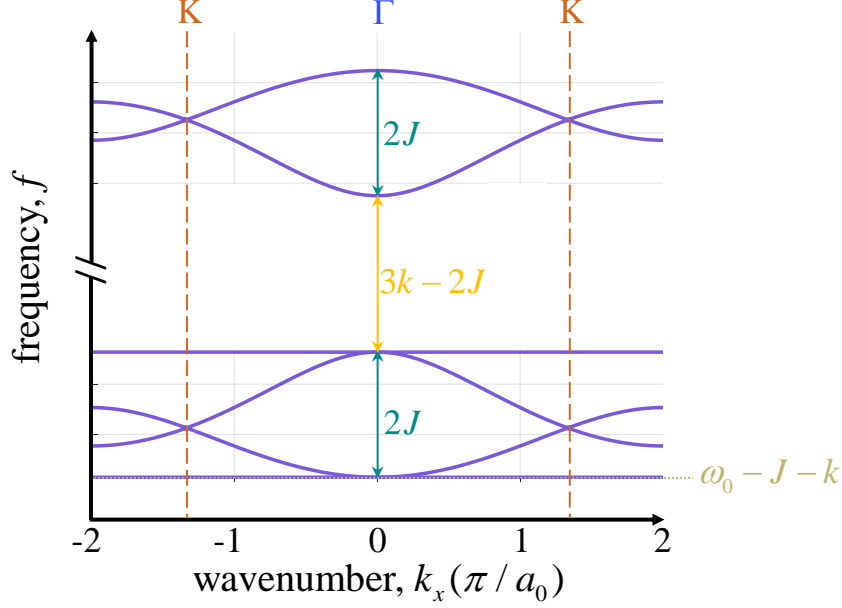


Figure 18: The band structure of the static crystal. The bottom four bands are of dipolar nature, whereas the top two bands are of monopolar nature. Figure adapted from [21].

The next step of the approach is to consider the effect of nonzero modulation, $\delta C \neq 0$. In order to extract the quasifrequencies of this system we calculate the stroboscopic Hamiltonian

$$\mathcal{H}_{eff} = \frac{i}{T} \log U(T), \quad (120)$$

where,

$$U(t) = \mathcal{T} \exp \left[-i \int_0^t \mathcal{H}(t) dt \right] \quad (121)$$

and \mathcal{T} is the time ordering operator. This effective Hamiltonian has the ability to describe the time evolution of the system at discrete times separated by T and hence acquire the quasifrequencies, in a similar way as a stroboscopic photography can sample the motion of a moving item. The dynamics of our system are actually much simpler than the ones of an arbitrary stroboscopic photographic shot: indeed, our Hamiltonian is not only time-dependent but also time periodic. This information is crucial because it implies that we can define a quasi-band structure that repeats itself along the frequency axis every $\omega + n\omega_m$ (where n is an integer). The repartition of the modal energy among the various Floquet Harmonics describes the frequency content of the Floquet mode. Next, we show the effect of the modulation on the quasi-band structure of the system.

To simplify the design procedure, we start by isolating the upper two bands of the quasi band structure from the bottom four in the limit of the vanishingly small modulation depth. We will then focus only on what happens to the bottom four bands when the modulation depth is increased. For this purpose, let us define the dimensionless parameters: $Q_T = \omega_0/2J$, $Q_M = \omega_0/2k$, $x_T = Q_T \omega_m/\omega_0$ and $x_M = Q_M \omega_m/\omega_0$, where ω_0 is the resonant frequency of the cavities. From the tight binding model it is straightforward to show that the condition which guarantees that the two upper bands remain isolated from the rest once folded along the frequency axis is, $x_T > 2$. We also stress that this condition only takes into account the folding of the static band structure of the static lattice into the first temporal Brillouin zone, providing a starting point for the design of a system with non-overlapping dipolar and monopolar bands at small modulation depths, but does not guarantee the absence of band overlapping when the modulation depth gets too large. The physical meaning

of the parameter x_T is to quantify the empty frequency space left (not occupied) in the temporal Brillouin zone by the bands. The values of x_T larger than 2 mean that some space is left in the temporal Brillouin zone, and under this condition only, it is possible to find values of x_M which do not fold the two upper bands on top of the four lower bands. $x_T > 2$ is a necessary but not sufficient condition to obtain separated bands, and the value of x_M also has to be adjusted.

In order to demonstrate the sway that the time–Floquet dynamics dictate to the system, we set our structure with the following parameters (as an example): $\omega_0 = 200$ MHz, $\omega_m = 17.89$ MHz, $J = 2$ MHz and $k = 62.6$ MHz which result in $Q_T = 50$, $Q_M = 1.6$, $x_T = 4.5$ and $x_M = 0.1428$ (these values satisfy the condition), while the dimensionless parameter representing the depth of the modulation is $y = Q_T \delta C / C_0 = Q_T \delta \omega / \omega_0$. It is evident that when we do not apply any modulation, $y = 0$, the stroboscopic analysis coincides with the static analysis as shown in Fig. 19(a) which illustrates the same band structure as in Fig. 18, although folded along the frequency axis. As we increase the modulation depth, the upper two bands are not affected by the activation of the Floquet dynamics, due to the monopolar symmetry of the modes, which does not overlap with the dipolar modulation scheme. However, the rest of the bands (see green arrows) are strongly affected by the modulation and become very flat, opening large bandgaps as shown in Fig. 19(b) for $y \approx 2.12$. If we continue to tune up the level of the modulation (for $y \approx 3.134$), the two bands highlighted with light green arrows in Fig. 19 get close to each other at the center of the Brillouin zone and form a Dirac cone, turning the sound insulator into a time–Floquet zero index acoustic metamaterial at the Dirac frequency. Figure 19(d) shows the 3D graphic representation of the two bands of interest, demonstrating the existence of genuine conical dispersion over almost the entire Brillouin zone. It is remarkable that the dispersion of

the massless Floquet Dirac phonons remains linear over a very large area of the Brillouin zone.

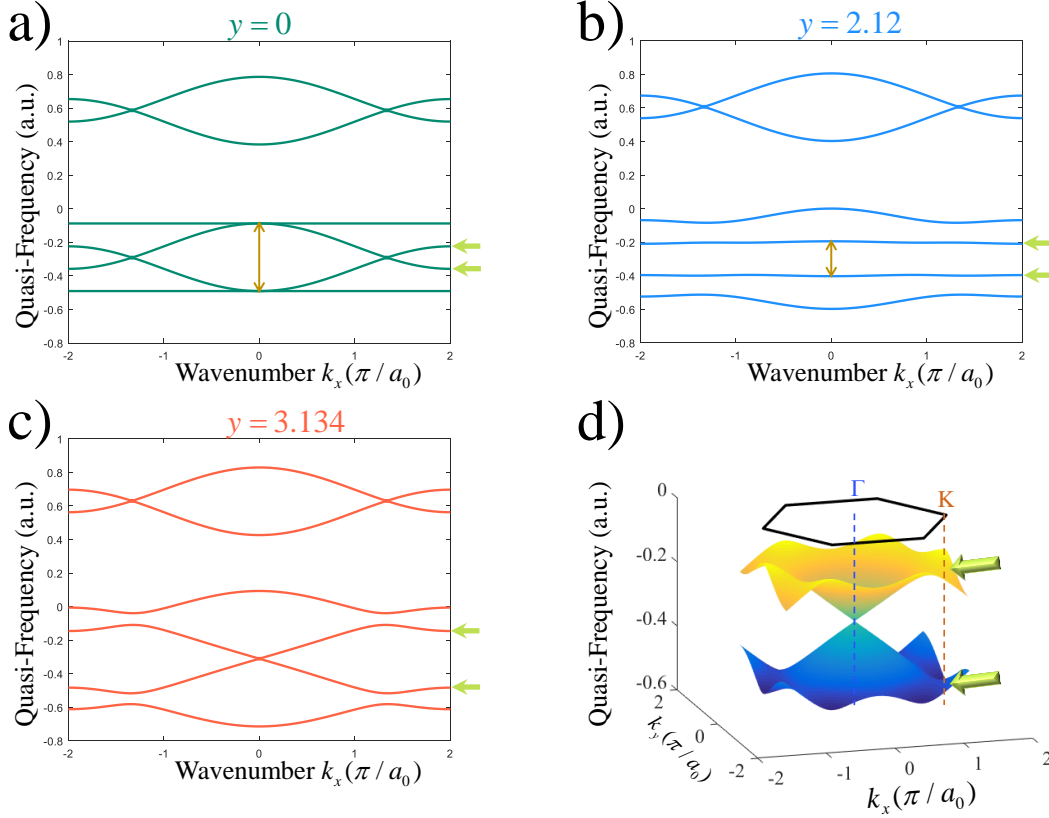


Figure 19: The quasi band structure of the time-Floquet system as the modulation depth increases (the two bands that eventually form a Dirac cone at Γ are highlighted by the light green arrows). (a) The band structure of the unmodulated system, $y = 0$ (same as in Fig. 25, but folded), (b) the band structure becomes flat as modulation increases, $y \approx 2.12$ (c) at a specific modulation depth, the Dirac cone appears in the center of the Brillouin zone, $y \approx 3.134$, (d) a 3D graphical representation of the Dirac cone, showing its large spatial extent in the Brillouin zone (black hexagon). Figure adapted from [21].

So far, our investigations were only based on a toy model relying on the tight-binding stroboscopic Hamiltonian. We now turn to full-wave finite

element simulations to corroborate the exact behavior of the system as a stroboscopic zero index structure. We set the parameters $\delta C/C_0 = \delta\omega/\omega_0 = 9.745\%$ with a time-modulation frequency of $f_m = 1312.5$ Hz and the coupling rates of $k \approx 6840$ Hz and $J \approx 209.38$ Hz. The tight binding model is an abstract mathematical tool, which describes the coupling interactions of complex structures [30]. Such systems can be normalized over the maximum resonant frequency or an arbitrary frequency value. Thus, what is important for this kind of modeling is only the relative value of the coupling with respect to the resonance frequencies and the necessary separated-bands conditions to be satisfied. This gives us the flexibility to observe the relative similarities of our simulation and our previous theoretical example. The computational tool we use to illustrate the time-Floquet dynamics of the system is the finite-element method with a truncation of the Floquet expansion of the acoustic wave equation to -1 , 0 and $+1$ Floquet Harmonics.

We compute the dispersion relation of the structure. Our results shown in Fig. 20(a) show the quasi-band structure obtained in the simulation for the four bands of interest, and the two upper bands are indeed isolated (not shown in Fig. 20 for brevity). The graph of the dispersion follows the theoretical results of the band structure described before. The results are in excellent agreement with the analytical prediction, demonstrating the expected conical dispersion for frequency $f = 21889$ Hz at $\mathbf{k} = 0$. Figure 20(b) shows the three dominant Floquet Harmonics associated with the two degenerate acoustic modes at Γ . The dominant frequency at which we have wave propagation in this system is the 0^{th} Floquet Harmonic. This means that there is no significant energy conversion to adjacent Floquet Harmonics, consistent with the relatively low value of the modulation depth.

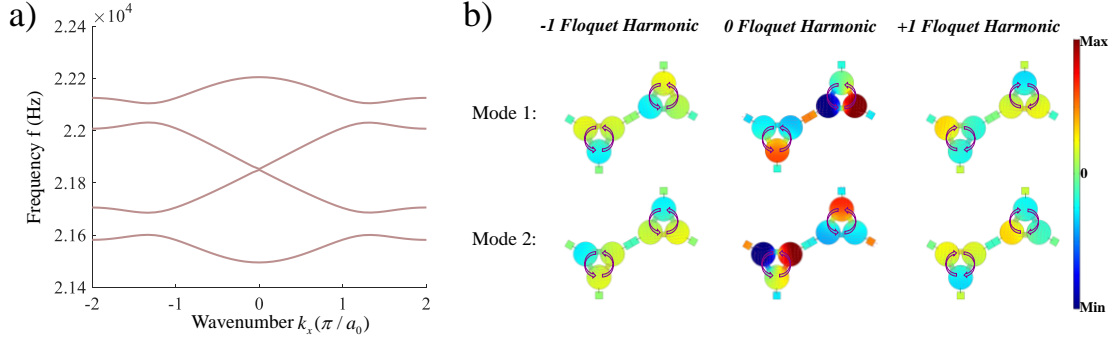


Figure 20: FEM simulation of the infinite space-time crystal. (a) Band structure of the full-wave simulation for $\delta C/C_0 = \delta\omega/\omega_0 = 9.745\%$ and $f_m = 1312.5$ Hz and the formulation of the Dirac cone at $f = 21889$ Hz. (b) Acoustic pressure of the modes at the Dirac frequency $f = 21889$ Hz (frequency components corresponding to -1 , 0 and $+1$ Floquet Harmonics). Figure adapted from [21].

Since we know the band structure of our model, we can now simulate the acoustic pressure propagation in finite-size acoustic metamaterials, exciting the stroboscopic zero refractive index behavior for the specific Dirac frequency $f = 21889$ Hz (Figs. 21 and 22). To excite finite sized systems with plane waves, we used two rectangular domains (labeled I and II in Figs. 21 and 22) filled with water and located outside the metamaterials. Both the simulations in Figs. 21 and 22 depict the scattering profile of the acoustic metamaterial for -1 , 0 and $+1$ Floquet Harmonic acoustic pressure fields.

-1 Floquet Harmonic

0 Floquet Harmonic

+1 Floquet Harmonic

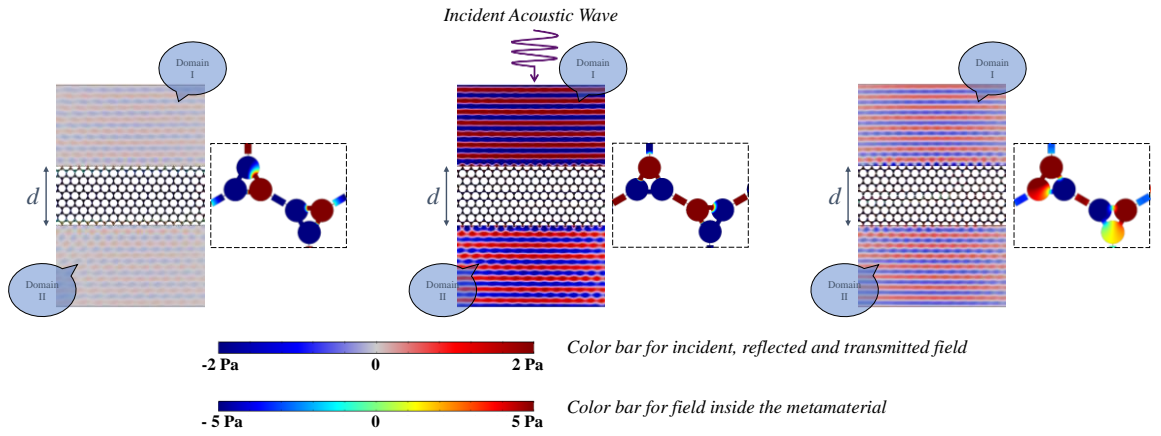


Figure 21: Full-wave simulation of a zero-index time-Floquet slab: the acoustic pressure field as it is reflected and transmitted by a rectangular metamaterial slab (domains I and II are filled with water). Figure adapted from [21].

More specifically, in Fig. 21, the metamaterial forms a slab: the incident and reflected fields are illustrated in domain I and the transmitted field is illustrated in the domain II.

-1 Floquet Harmonic

0 Floquet Harmonic

+1 Floquet Harmonic

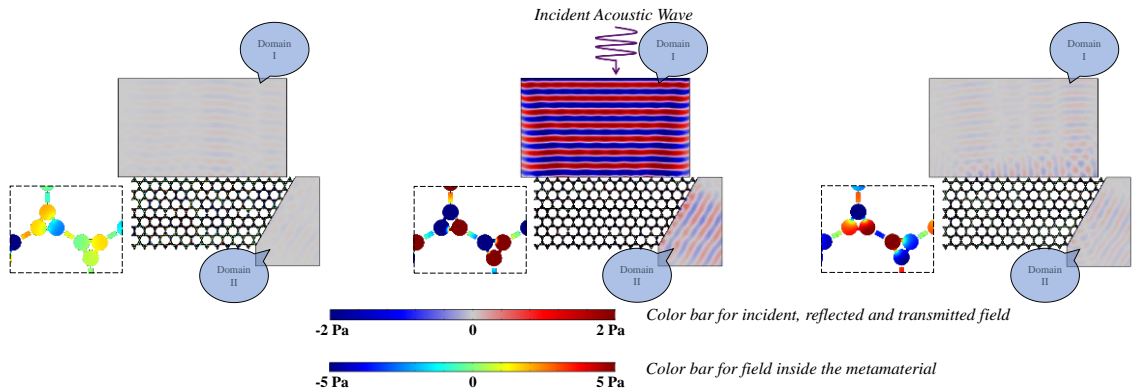


Figure 22: Full-wave simulation of a zero-index time-Floquet prism: the acoustic pressure field as it is reflected and transmitted by a metamaterial prism,

demonstrating zero-index properties at the fundamental harmonic frequency (domains I and II are filled with water). Figure adapted from [21].

Fig. 22 shows a similar simulation for which the metamaterial has the shape of a prism. For the simulation of Fig. 22, it is shown that the transmitted field is actually a steered plane wave with the transmitted wavefront determined by the direction of the output interface, a result which agrees well with the propagation theory of zero-index materials. We stress that the simulation in Fig. 22 is of a hard wall waveguide (domain I) connected to another waveguide (domain 2) of a different width and geometry. Since the effective impedance of a waveguide depends on its cross section, there is a mismatch between the two domains which does not exist in Fig. 21 and cause the transmission to the second domain in Fig. 22 to be slightly reduced when compared to Fig. 21. In either case, by looking at the scale bar, it is clear that the dominant frequency of the system remains at the 0^{th} Floquet Harmonic, which corresponds to the frequency of the incident acoustic field.

The simulation of a finite-thickness slab depicted in Fig. 21 can be used to extract an effective refractive index, N_{eff} for the metamaterial and an effective acoustic impedance Z_{eff} . The computation of the model of Fig. 21 gives us the transmission, S_{21} and reflection S_{11} of the field. With these simulation results, it is straightforward to determine the characteristics of the material as a homogenous medium, by applying the following equations [71,72]:

$$Z_r = \frac{Z_{eff}}{Z_0} = \pm \sqrt{\frac{(1+S_{11})^2 - S_{21}^2}{(1-S_{11})^2 - S_{21}^2}} \text{ and } \exp(iN_{eff}k_0d) = \frac{S_{21}}{1-S_{11}\frac{Z_r-1}{Z_r+1}}. \text{ } d \text{ is the slab thickness. The}$$

length d has been selected to be $d \gg a_0$, where a_0 is the lattice constant of the acoustic metamaterial, so that the extraction procedure is valid. When this condition is satisfied, a deviation of d does not change the outcome of the effective index or the effective impedance, which confirms that N_{eff} , Z_{eff} are

meaningful effective parameters. These formulae give an acoustic impedance of $Z_{eff} = (295.86 + i1050.7)\text{kPa s/m}$ and an effective acoustic index of $N_{eff} = -0.0127 + i0.0056$. It is evident that the system is not completely matched since the effective impedance is different from the one of water (1500 kPa s/m). This is mainly due to the hard walls along the interface between the metamaterial and the external space. As expected, the real part of the relative acoustic index is very close to zero. The non-zero imaginary part represents losses from the viewpoint of the 0^{th} order Floquet field.

In this subsection, we have presented an active acoustic metamaterial that exhibits near the zero refractive index. In contrast to the existing literature, we derived this peculiarity by activating time-Floquet dynamics and by tuning the time-modulation depth to a specific point that provides a quasi-band structure featuring a Dirac cone at the Γ point. Such a structure possesses the advantage to be reconfigurable and to provide a unique platform for the observation of acoustic waves with pseudo-spin $1/2$. A zero refractive index is achieved from just the dipolar modes in contrast to the existing literature. This is feasible due to the dynamics of the time-modulated system. Contrary to static systems, here frequency is not conserved and the interactions between the dipolar mode of the zero harmonic and its two nearest neighboring harmonics (which are also dipolar) result in a conical dispersion at the center of the Brillouin zone.

4.4 Induced gain and frequency conversion in time-varying coupling of a two-by-two Hamiltonian system

In this subsection, we examine a special resonant system and its effects on the scattering when the coupling is temporally varying [22]. Let us assume a two-by-two Hamiltonian: $\mathcal{H} = [\omega_1, k_{12}(t); k_{21}(t), \omega_2]$, where $k_{21}(t) = k_{12}^*(-t)$, consistent with a coupling from a time-varying material and taking into

account the Stokes principle of microscopic reversibility^{viii} ([73] and Appendix B). A particular example and one of interest to this subsection is the one with the form $k_{21}(t) = k_{12}(t) = K(t) = k_0 + \Delta k' \cos(\Omega t) + j\Delta k'' \sin(\Omega t)$ (as shown in Fig. 23). Such Hamiltonians are not just non-Hermitian due to the third term but also periodic in time with a period of $T = 2\pi/\Omega$. As shown in Fig. 23, we consider the two coupled resonators with $K(t)$ coupling and resonance frequencies ω_1, ω_2 with $\omega_1 < \omega_2$ which are combined with two ports for incoming or outgoing wave signals, with decay rates γ_1 and γ_2 respectively.

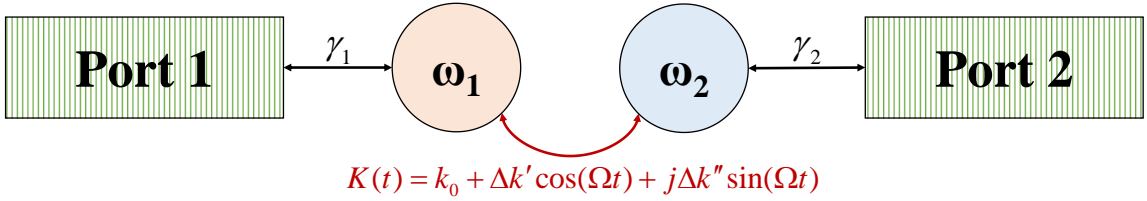


Figure 23: Non-Hermitian time-Floquet system under study. Two coupled resonators with resonant frequencies ω_1 and ω_2 are connected to ports 1 and 2, with lifetimes $1/\gamma_1$ and $1/\gamma_2$. The complex internal coupling coefficient $K(t)$ is time dependent, with $K(t) = k_0 + \Delta k' \cos(\Omega t) + j\Delta k'' \sin(\Omega t)$. Figure adapted from [22].

The Floquet theorem in combination with the temporal coupled mode theory assuming an incident wavesignal from port 1 at ω frequency [36], give us the equations of the modes α_1 and α_2 at the resonators

$$(\omega + n\Omega - \omega_1 - j\gamma_1)\alpha_1^n - k_0\alpha_2^n - \frac{\Delta k' + \Delta k''}{2}\alpha_2^{n-1} - \frac{\Delta k' - \Delta k''}{2}\alpha_2^{n+1} = \sqrt{2\gamma_1}\delta_{n0}, \quad (122)$$

^{viii} In the literature [83], one can find also different conditions for such artificial systems which could be considered consistent under the appropriate physical platform or engineered devices.

$$(\omega + n\Omega - \omega_2 - j\gamma_2)a_2^n - k_0 a_1^n - \frac{\Delta k' + \Delta k''}{2} a_1^{n-1} - \frac{\Delta k' - \Delta k''}{2} a_1^{n+1} = 0, \quad (123)$$

where δ_{n0} is the delta function, $n \in \mathbb{Z}$ and $\alpha_{1,2} = \sum_n a_{1,2}^n e^{j(\omega+n\Omega)t}$. We see that k_0 couples identical frequencies, whereas the harmonic time–Floquet modulation couples each resonator with the two adjacent Floquet harmonics in the other resonator. For a Hermitian system ($\Delta k'' = 0$), upward and downward frequency conversion are equally efficient. Conversely, adding a non–Hermitian time–Floquet modulation allows one to tune the amount of energy that will undergo upward and downward frequency transitions. Crucially, the condition $\Delta k'' = \Delta k'$ is special as it enables only upward frequency conversion.

To illustrate better the profound implication of this special condition on the scattering properties of the system, let us assume incidence from port 1 at $\omega = \omega_1$ and $\Omega = \omega_2 - \omega_1$, so that the +1 harmonic is exactly at ω_2 which excites optimally the second resonator. Fig. 24 shows the norm of the field amplitudes $\alpha_{1,2}^n$ of the -1 , 0 and $+1$ Floquet harmonics in various cases of interest. In the Hermitian case [Fig. 24(a), $\Delta k'' = 0$], the -1 , 0 and $+1$ Floquet harmonics of the field amplitudes $\alpha_{1,2}$ all have significant energy. When we increase $\Delta k'$, the energy of the -1 and $+1$ modes both increase, since all the frequency conversion rates are equal and proportional to $\Delta k'$. Still for $\Delta k'' = 0$, another interesting phenomenon occurs if we force k_0 to become zero [Fig. 24(b)]: the system is driven to a condition where the second resonator cannot have a 0 harmonic and transmission to the second port can only be at a frequency different than the incident. Yet, in both Hermitian cases of Figs. 24(a)–24(b), because upward and downward frequency conversion coefficients are equal, the transmission coefficient for incidence at port 2 with frequency ω_2 to port 1 with frequency ω_1 would be the same with the transmission coefficient for an

input field at port 1 at ω_1 to port 2 at ω_2 , hence the system is reciprocal. The situation is drastically different when we provide the system with a non-Hermitian time-periodic modulation [Figs. 24(c)–(d)]. The plots are made under the special condition $\Delta k'' = \Delta k'$, which promotes absolute upward frequency conversion. As discussed above, this modulation never excites the -1 harmonic, whose amplitude is always identically zero, and forces the system to exhibit only the 0 and $+1$ Floquet harmonics [Fig. 24(c)]. In addition, if we force $k_0 = 0$, the only remaining states are α_1^0 and α_2^1 [Fig. 31(d)]. This means that the field is transmitted to port 2 only via α_2^1 , through upward frequency conversion. Evidently, in these conditions a backward field incident on port 2 at ω_2 will neither be downward converted to ω_1 (since downward conversions are forbidden), nor be transmitted at ω_2 through the zero harmonic, while the transmission to port 1 will be identically zero.

Therefore, the non-Hermitian time-Floquet system can exhibit perfect nonreciprocity: it transmits energy incident on port 1 to port 2, but has zero transmission for any signal incident on port 2.

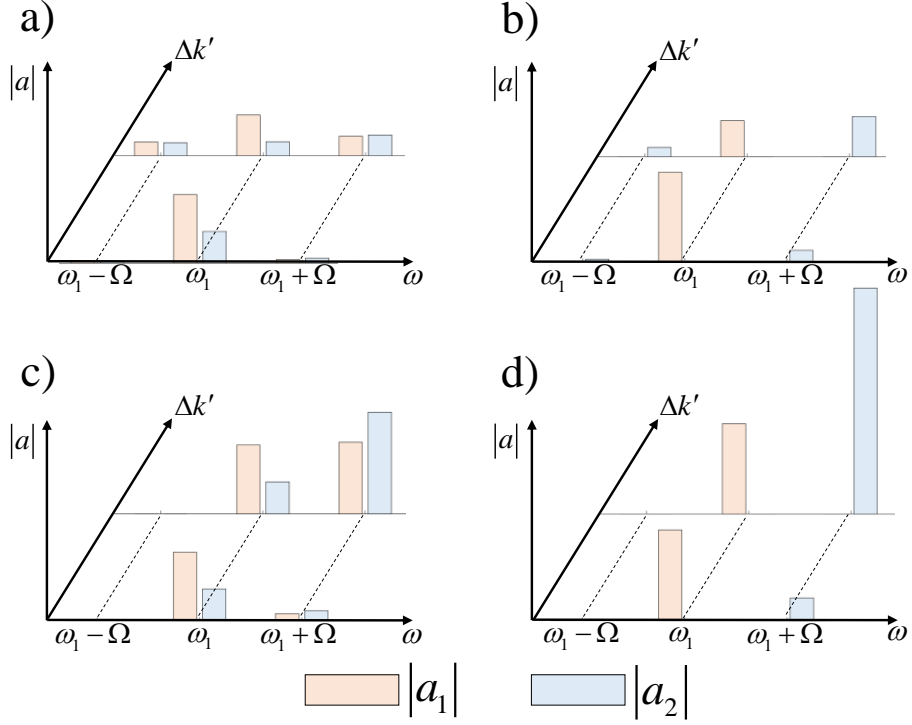


Figure 24: Excited Floquet amplitudes for incidence at ω_1 from port 1. We represent the amplitudes of the three dominant Floquet harmonics in the first (orange) and second (blue) resonators for two different (arbitrary) values of $\Delta k'$ and for (a) $\Delta k'' = 0$ and $k_0 \neq 0$, (b) $\Delta k'' = 0$ and $k_0 = 0$, (c) $\Delta k'' = \Delta k'$ and $k_0 \neq 0$, and (d) $\Delta k'' = \Delta k'$ and $k_0 = 0$. Figure adapted from [22].

Assuming time-harmonic incidence on port 1, with $\psi_{inc} = \psi_{inc}^0 e^{j\omega t}$, the transmitted field at the second port can be expanded as $\psi_t = \sum_n \psi_t^n e^{j(\omega + n\Omega)t}$, and we can define a transmission coefficient for each frequency harmonic as $S_{21}^n = \psi_t^n / \psi_{inc}^0$. Here, only the -1 , 0 and $+1$ harmonics are important and we use the short-hand notations S_{21}^- , S_{21}^0 and S_{21}^+ . Similarly, we define transmission coefficients for excitation from port 2 and note them S_{12}^- , S_{12}^0 and S_{12}^+ .

We present in Fig. 25 the evolution of $|S_{21}^+(\omega_1)|$ and $|S_{12}^-(\omega_2)|$ as $\Delta k'$ is gradually increased, comparing excitation from port 1 at ω_1 and the reciprocal situation of excitation from port 2 at ω_2 . We also look at the transmission at the incident frequency $|S_{21}^0(\omega_1)|$ and $|S_{12}^0(\omega_2)|$. We consider two cases: (i) the Hermitian case with $k_0 = \Delta k'' = 0$ [Fig. 32(a)], and (ii) the non-Hermitian case with $k_0 = 0$ $\Delta k'' = \Delta k'$ [Fig. 32(b)]. Because $k_0 = 0$ in both cases, transmission at the excitation frequency is impossible, thus S_{21}^0 and S_{12}^0 are zero. In the Hermitian case, frequency conversion is symmetric and therefore the system is always reciprocal: we have $|S_{21}^+(\omega_1)| = |S_{12}^-(\omega_2)|$. Conversely, in the non-Hermitian case, transmission from port 2 to port 1 is identically zero regardless of the considered harmonic, whereas $|S_{21}^+(\omega_1)|$ is nonzero, demonstrating the large nonreciprocal behavior. In addition, for sufficiently high values of $\Delta k'/\sqrt{\gamma_1\gamma_2}$, we find that $|S_{21}^+(\omega_1)|$ can even reach values well above unity resulting in parametric amplification. Remarkably, the non-Hermitian time-Floquet modulation provides unidirectional parametric gain to the signal. A closed-form analytical validation of this amplifying behavior can be obtained if we truncate the system of eqs. (122), (123) to three Floquet harmonics. For a field incident at port 1 at frequency ω_1 , we find

$$S_{21}^+ = \frac{2\sqrt{\gamma_1\gamma_2}\Delta k' [(-\Omega - j\gamma_1)(-\Omega - j\gamma_2) + k_0^2]}{[(-j\gamma_1)(-\Omega - j\gamma_2) - k_0^2][(\Omega - j\gamma_1)(-j\gamma_2) - k_0^2]}. \quad (124)$$

If $k_0 = 0$, eq. (124) becomes $S_{21}^+ = -2\Delta k'/\sqrt{\gamma_1\gamma_2}$, which is identical with the results in Fig. 25(b), obtained numerically considering 201 Floquet harmonics. It is noteworthy that amplification can be obtained with arbitrarily small

modulation depths $\Delta k'' = \Delta k'$ as long as the system is resonant enough, i.e., $\sqrt{\gamma_1 \gamma_2} < \Delta k'$. Using the same method, we have also checked that the transmission coefficients of the 0 Floquet harmonic S_{21}^0 and S_{12}^0 are proportional to k_0 , and thus become zero when $k_0 = 0$, in perfect agreement with the results of Fig. 25.

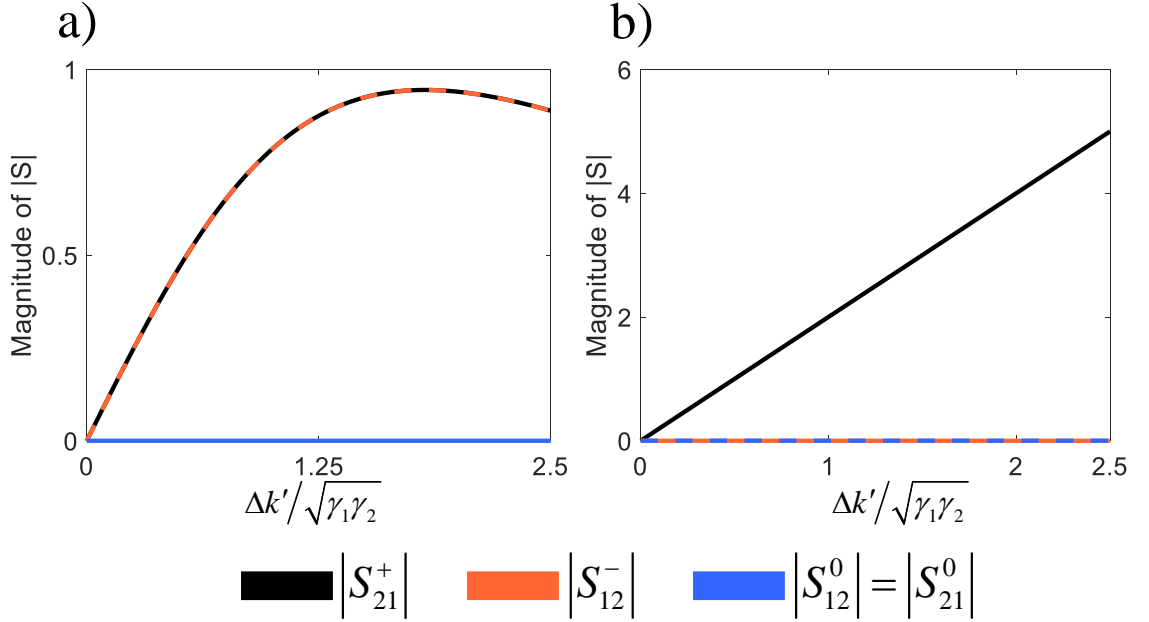


Figure 25: Nonreciprocal gain in non-Hermitian time-Floquet systems. We plot the magnitude of the transmission coefficients to demonstrate the highly nonreciprocal behavior of the system. S_{21}^0 and S_{21}^+ correspond to the transmissions to port 2, respectively, at ω_1 and ω_2 , when a signal at ω_1 is incident on port 1. S_{12}^0 and S_{12}^- correspond to the transmissions to port 1, respectively, at ω_2 and ω_1 , when a signal at ω_2 is incident on port 2. We compare the (reciprocal) Hermitian time-Floquet system with (a) $\Delta k'' = 0$ and $k_0 = 0$ to the (nonreciprocal) non-Hermitian time-Floquet system (b) $\Delta k'' = \Delta k'$ and $k_0 = 0$. Transmission through any other frequency channel is identically zero. Figure adapted from [22].

We demonstrate our findings in a full-wave device simulation at microwave frequencies. The resonators are split rings with eigenfrequencies $f_1 = 3.1201$ GHz and $f_2 = 3.6921$ GHz, the ports are microstrip transmission lines of width 0.333 mm and height 0.1778 mm, while the substrate is FR4 with $\varepsilon_r = 4.5$.

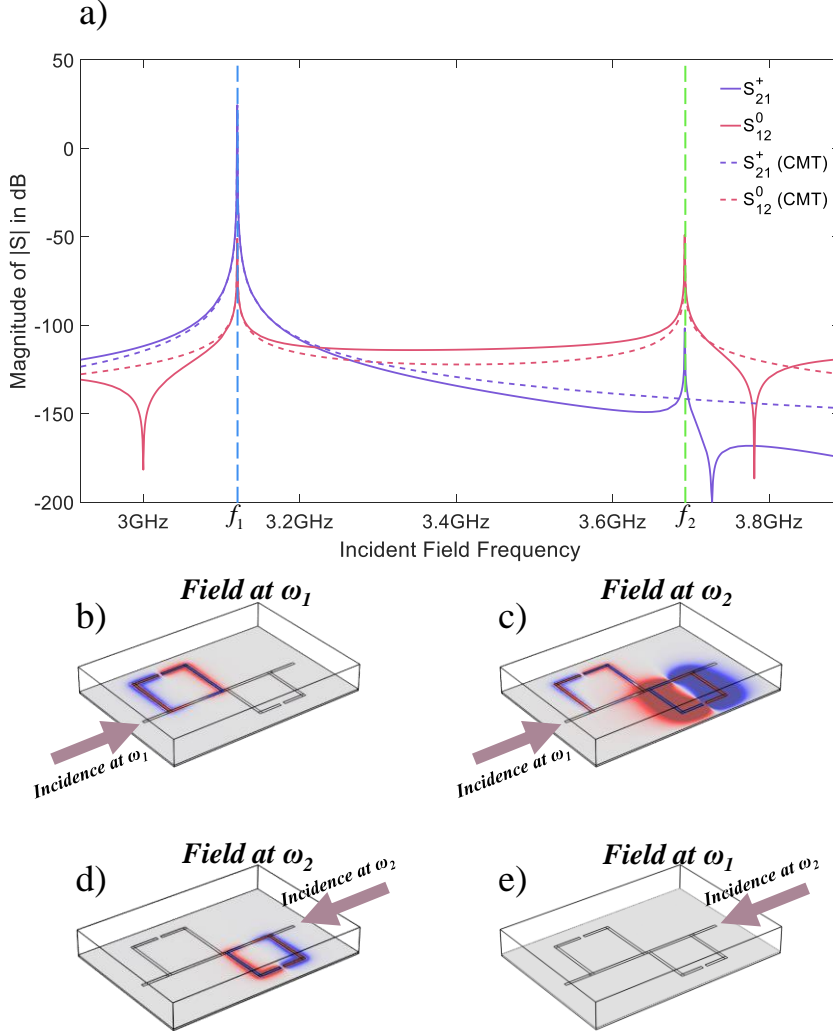


Figure 26: Full-wave finite-element demonstration of non-reciprocal gain at microwave frequencies. (a) Spectrum of the scattering parameters demonstrating strong nonreciprocity and one way amplification in a non-Hermitian time-Floquet system made of coupled split-ring resonators at f_1 . Panels (b) and (c) correspond to incidence on port 1 at ω_1 and show the vertical electric field component at ω_1 and ω_2 ,

respectively. (d),(e) Same as (b) and (d) for incidence on port 2. All panels are plotted with the same scale, where blue correspond to a negative field and red to a positive field. Figure adapted from [22].

Between the resonators, we insert a complex capacitor of $C = 15.849$ fF, which has a small modulation with depth $\Delta C = 0.15849$ fF and slow modulation frequency $f_c = 572$ MHz. The complex coupling as aforementioned can be achieved by time-varying materials since $C \sim \varepsilon$ for a broad band of frequencies or by a complex circuit with simultaneous modulation of the resistor distributed in a number of harmonics with depth equal to $\Delta R = 1/\Delta C \omega$ [22,73,74]. To minimize the static coupling strength k_0 , we keep some distance between the components and place the resonators in antisymmetric positions (Fig. 26). The fields are computed using the three-dimensional finite-element method (FEM) method in frequency domain using a truncation of Maxwell's equations to three harmonics $\{-1, 0, +1\}$. Fig. 26(a) shows the numerical results (solid lines), and compares them to the analytical CMT model (dashed lines). In Fig. 26(a), we plot the spectrum in dB of the only nonzero transmission coefficients: $|S_{21}^+(\omega)|$, and $|S_{21}^0(\omega)| = |S_{12}^0(\omega)|$. Note that the x axis of Fig. 26(a) corresponds to the frequency of the incident field. A point of abscissa ω on the curve $|S_{21}^+(\omega)|$, for instance, describes the amplitude of the Fourier component at $\omega + \Omega$ of the field transmitted to the second port as defined before. Therefore, the peak of $|S_{21}^+|$ at the position f_1 of the x axis corresponds to a strong transmission to port two at $f_2 = f_1 + \Omega/2\pi$, i.e., transmission via upward frequency conversion. The level of this peak is above 30 dB, meaning amplification. At any other frequency, including at f_2 , the transmission from port 2 to port 1 $|S_{12}^0|$ is always

below -50 dB; i.e., $|S_{21}^+|$ is more than 80 dB higher than $|S_{12}^0|$ over the entire spectrum, which demonstrates that this parametric amplification phenomenon is indeed strongly nonreciprocal and well suited for signal isolation. The analytical model captures very well the physics involved, the only discrepancies being attributed to the inherent dispersion of the coupling coefficients, which is neglected in CMT. These discrepancies are extremely small, as they correspond to corrections that are -100 dB below the incident field level. We find that the unidirectional transmission gain is linearly controlled by the modulation depth ΔC and the quality factor of the system, in perfect agreement with coupled mode theory. The simple Hamiltonian model is therefore a very good description of this system.

Below the spectrum, we show the distribution of the electric field (vertical component). Since this field is principally made up of two frequency components (at ω_1 and ω_2), we plot each component separately. When the signal is incident from port 1 at ω_1 [Fig. 26(b)], the field component at ω_1 remains isolated on the first resonator and no field is excited at frequency ω_1 in the second resonator, preventing transmission to port 2 at this frequency. This is consistent with the very small static coupling k_0 between the rings. However, a nonzero field exists in the second resonator at frequency ω_2 [Fig. 26(c)], which is consistent with upward frequency conversion. This field leaks out to port 2, giving nonzero transmission. When the signal is incident from port 2 at ω_2 , the field at ω_2 remains localized on resonator 2, and there is no significant transmission to port 1 [as shown in Fig. 26(d)]. Because of the upward-only frequency conversion property, downward frequency conversion is not allowed and the Floquet harmonic at ω_1 is identically zero [Fig. 26(e)], making the system an extremely efficient isolator. The same phenomenon happens if $\omega_1 > \omega_2$, providing Ω is negative; i.e., the helicity of the modulation is reversed to get downward frequency conversion. Therefore, by cascading two

inverted systems, one with upward frequency conversion, and one with downward frequency conversion, a nonreciprocal amplifier which operates without changing the frequency of the signal could be exhibited.

Chapter 5:

Conclusion

In this thesis, electromagnetic wave propagation was studied in nonstationary–medium scenarios in chapters 2–3. Electromagnetic fields under material time–modulation conserve their momentum but not their energy. The proper analysis to treat wave propagation in time–Floquet media was given and their related parametric amplification phenomena were investigated. Assuming a time–variation of permittivity, permeability and conductivity the appropriate time–domain solutions are derived based on the causality state at a past observation time. The formulation of a time–transitioning state matrix connects the unusual energy transitions of electromagnetic fields in time–varying media with the exceptional point theory. This state–matrix approach allows the analysis of the electromagnetic waves in terms of parity and time–reversal symmetries and signifies parity–time symmetric wave–states without the presence of a spatially symmetric distribution of gain and loss, or any inhomogeneities and material periodicity. Additionally, the parametric amplification phenomena of time–Floquet media and more precisely those that generate a Mathieu equation for the electric displacement field are theoretical studied and numerical compared with simulations using FDTD and connected with the parity–time scattering characteristics.

In chapter 4, a collection of studies regarding resonant acoustic and electromagnetic systems is exhibited. In the beginning of the chapter the theoretical foundation to treat both acoustic and electromagnetic resonant

phenomena is provided based on the coupled mode theory and the appropriate Hilbert space. Two examples of interest are given leveraging the time–dynamics of a temporal resonant system. The first example is related to the design of an artificial resonant acoustic lattice which with the appropriate time–modulation can have an effective zero index of refraction. The second example is related to a study related to resonant systems with temporal coupling and the possibility to induce nonreciprocal gain by leveraging the frequency conversion occurring in parametric systems.

The present thesis, aside from enriching the literature, also provides an insight on the broad capabilities of time–varying systems in electromagnetics, optics and acoustics and may be used as a guidance to design and fabricate wave devices that amplify and actively filter wave signals, for many future applications in telecommunications, amplifiers, energy transfer and imaging.

Appendix A:

Nonstationary and inhomogeneous medium equations

The electromagnetic equations for $\varepsilon = \varepsilon(\mathbf{r}, t)$, $\mu = \mu(\mathbf{r}, t)$ and $\sigma = \sigma(\mathbf{r}, t)$ are [17]:

$$\begin{aligned} \nabla \times \frac{1}{\mu} \nabla \times \mathbf{E} + \varepsilon \frac{\partial^2 \mathbf{E}}{\partial t^2} + \left[\sigma + 2 \frac{\partial \varepsilon}{\partial t} + \varepsilon \frac{\partial \ln \mu}{\partial t} \right] \frac{\partial \mathbf{E}}{\partial t} + \left[\frac{\partial \sigma}{\partial t} + \frac{\partial^2 \varepsilon}{\partial t^2} + \left(\frac{\partial \varepsilon}{\partial t} + \sigma \right) \frac{\partial \ln \mu}{\partial t} \right] \mathbf{E} = \\ \mathbf{H} \times \nabla \frac{\partial \ln \mu}{\partial t} - \left[\frac{\partial \ln \mu}{\partial t} + \frac{\partial}{\partial t} \right] \mathbf{J}, \end{aligned} \quad (125)$$

$$\begin{aligned} \nabla \times \frac{1}{\varepsilon} \nabla \times \mathbf{H} + \mu \frac{\partial^2 \mathbf{H}}{\partial t^2} + \left[2 \frac{\partial \mu}{\partial t} + \left(\frac{\sigma}{\varepsilon} + \frac{\partial \ln \varepsilon}{\partial t} \right) \mu \right] \frac{\partial \mathbf{H}}{\partial t} + \left[\frac{\partial^2 \mu}{\partial t^2} + \left(\frac{\sigma}{\varepsilon} + \frac{\partial \ln \varepsilon}{\partial t} \right) \frac{\partial \mu}{\partial t} \right] \mathbf{H} = \\ -\mathbf{E} \times \nabla \left(\frac{\sigma}{\varepsilon} + \frac{\partial \ln \varepsilon}{\partial t} \right) + \nabla \times \frac{1}{\varepsilon} \mathbf{J}. \end{aligned} \quad (126)$$

Eqs. (125)–(126) describe the electrodynamic–wave interactive phenomena with material time–variation and inhomogeneities. The wave equations have extra terms associated with the derivative coefficients and the sources due to the unusual properties imparted by the combination of time–variation and the inhomogeneities.

A sufficient condition to decouple the electric field equation from the \mathbf{H} is: $\nabla \frac{\partial \ln \mu}{\partial t} = 0$. Such condition is naturally satisfied for stationary media and implies that the permeability is a product of a function that depends only on space μ_r and a function the depends only on time μ_t : $\mu = \mu_r \mu_t$. The electric field thus becomes in the absence of currents:

$$\nabla \times \frac{1}{\mu_r} \nabla \times \mathbf{E} + \frac{\partial}{\partial t} \left[\mu_t \left(\frac{\partial(\varepsilon \mathbf{E})}{\partial t} + \sigma \mathbf{E} \right) \right] = 0. \quad (127)$$

Analogously for the magnetic field equation the condition is: $\nabla \left[\frac{\sigma}{\varepsilon} + \frac{\partial \ln \varepsilon}{\partial t} \right] = 0$. This condition is not naturally satisfied for stationary media, because the conductivity of the medium induces electric–displacement currents. The condition implies that the permittivity is a function of the form: $\varepsilon = \varepsilon_r \varepsilon_t \exp \left[- \int_{\tau}^t \frac{\sigma}{\varepsilon} dt \right]$, for $t > \tau$ where ε_r depends on space while ε_t depends only on time. If in addition $\sigma = \sigma_r \sigma_t$ with $\sigma_r = \varepsilon_r$, then the magnetic field equation in the absence of currents is:

$$\nabla \times \frac{1}{\varepsilon_r} \nabla \times \mathbf{H} + \frac{\partial}{\partial t} \left[\varepsilon_t e^{-\int_{\tau}^t \frac{\sigma}{\varepsilon} dt} \frac{\partial(\mu \mathbf{H})}{\partial t} \right] + \sigma_t \frac{\partial(\mu \mathbf{H})}{\partial t} = 0. \quad (128)$$

In the special cases of space–time periodic media the solutions are found by the implementation of the Bloch–Floquet ansatz [75,76].

Appendix B:

Dipole polarizability under nonstationary conditions

If a wave with frequency ω incidents into an atom, the electric field in the former acts on the elastically bound electrons in the latter and sets them into oscillation with the same frequency. Each of the electrons acquires an instantaneous dipole moment with respect to its equilibrium position, and as far as the scattered wave is concerned, the atom can be regarded as a single dipole whose moment is the vectorial sum of those of the several electrons. Once the dipole moment is known, all the characteristics of the scattered wave are found.

Finding the dipole moment requires solving the equations of motion of the electrons under the external force. The amplitude of the moment is proportional to that of the applied electric field. If the moment and the field are thus expressed in complex form, the complex amplitude of the electric field \mathbf{E} is multiplied by a complex scalar, called polarizability kernel α , to obtain the complex amplitude of the dipole moment \mathbf{p} .

$$\mathbf{p}(\omega) = \alpha \mathbf{E}(\omega). \quad (129)$$

While the time-domain description of the formula (129) is a convolution integral [73]:

$$\mathbf{p}(t) = \int_0^{+\infty} \alpha(\xi) \mathbf{E}(t - \xi) d\xi. \quad (130)$$

The above equation illustrates two notable characteristics. The first is that the instantaneous dipole moment depends on the values of the field in the present and the past but not in the future (this is due to causality). The second characteristic is that if the electric field is temporally shifted, then the dipole moment will be also shifted by the same time units.

The situation can be different if the particle under study is under nonstationary conditions. Of course, causality has to remain, however time–translation is broken. A temporal shift of the electric field does not result in the same temporal shift of the induced dipole moment when nonstationary interactions are considered between the electrons and the field. A more general relation is thus required with respect to causality. Such relation is of the form:

$$\mathbf{p}(t) = \int_0^{+\infty} \alpha(\xi, t) \mathbf{E}(t - \xi) d\xi. \quad (131)$$

In this generalized relation the polarizability kernel α is not just a function of the delay between the action and the reaction ξ , but it also depends on the observation time t . The instantaneous value of the dipole depends not only on the past and the present values of the electric field, but also on the history of the evolution of the electronic properties. This is evident if the electric field is assumed to be a Dirac: $E(t) = \delta(t - t_0) \hat{u}$, where \hat{u} is a unit vector. The dipole moment equals with: $\mathbf{p}(t) = \alpha(t - t_0, t) \hat{u}$. The impulse response depends on how much time has passed since the pulse excitation was applied, but also on the present conditions explicitly. This property manifests that the particle

responds differently at different moments of time and that time–translation symmetry is broken.

An alternative form of the integral (131) can be useful. Using the transformation: $\tau = t - \xi$ and $h(t, \tau) = \alpha(\xi, t) \Big|_{\xi=t-\tau}$, then:

$$\mathbf{p}(t) = \int_{-\infty}^t h(t, \tau) \mathbf{E}(\tau) d\tau. \quad (132)$$

Through this variable transformation the causality of the systems is clearly proven, meaning that the integration limits show that the dipole moment depends only on past and present values of the polarizability and the electric field and not in future values and obeys the Kramers–Kronig relations [77]. For the stationary case, it is straightforward to show that: $h(t, \tau) = h(t - \tau)$ and $\partial_t \alpha = 0$ converting the integral polarizability relation to the known convolution.

The response of the electron is considered linear. An appropriate excitation field can be considered time–harmonic and in the form of: $\mathbf{E}(t) = \text{Re } \mathbf{E}_0 \exp(j\omega t)$, since an arbitrary response can be dealt by its Fourier expansion. The polarizability can be written in the form (according to eq. (131)):

$$p(t) = \text{Re} \left[\alpha_p(\omega, t) E_0 e^{j\omega t} \right], \quad (133)$$

where $\alpha_p(\omega, t) = \int_0^{+\infty} \alpha(\xi, t) e^{-j\omega\xi} d\xi$ and assuming that the dipole moment and the electric field are parallel (in a different case the polarizability is a tensor

of the second order). The instantaneous electric dipole is the real part of a complex-valued function, which is multiplied by the complex amplitude of the time-harmonic electric field $E_0 \exp(j\omega t)$. This formulation is no different than the known stationary one, however the complex function of α_p depends also on the variable t . Indeed, by implementing the usual Fourier transform: $\hat{g}(\omega, \omega') = \int_{-\infty}^{+\infty} g(\omega, t) e^{-j\omega' t} dt$, the dipole moment has the property: $\hat{p}^*(\omega, \omega') = \hat{p}(\omega, -\omega')$, while: $\hat{\alpha}_p^*(\omega, \omega') \neq \hat{\alpha}_p(\omega, -\omega')$. α_p is defined as a “temporal complex polarizability”^{ix}. The resulting dipole moment of (133) is not necessarily time-harmonic.

Consider the one-dimensional equation of motion for the position $x(t)$ of a bound electron under the influence of an electric field $E(t)$ and subject to a time-varying damping $\gamma(t)$, time-varying natural frequency $\omega_n(t)$ with charge q_e and mass m :

$$\frac{d^2 x(t)}{dt^2} + \gamma(t) \frac{dx(t)}{dt} + \omega_n^2(t) x(t) = \frac{q_e}{m} E(t). \quad (134)$$

The corresponding second order differential equation for the dipole moment is:

$$\frac{d^2 p(t)}{dt^2} + \gamma(t) \frac{dp(t)}{dt} + \omega_n^2(t) p(t) = \frac{q_e^2}{m} E(t). \quad (135)$$

^{ix} Notice that same definition was obtained in [84] for the characterization of the macroscopic susceptibility of time-varying plasmas.

The combination of the eqs. (131) and (135) can determine the polarizability under time-varying coefficients of the Drude–Lorentz model. The application of the Leibniz integral rule^x leads to the three relations, which should be satisfied:

$$\frac{\partial^2 h(t, \tau)}{\partial t^2} + \gamma(t) \frac{\partial h(t, \tau)}{\partial t} + \omega_n^2(t) h(t, \tau) = 0, \quad (136)$$

$$2 \frac{\partial h(t, \tau)}{\partial t} \Big|_{\tau=t} + \frac{\partial h(t, \tau)}{\partial \tau} \Big|_{\tau=t} = \frac{q_e^2}{m}, \quad (137)$$

$$h(t, \tau) \Big|_{\tau=t} = 0. \quad (138)$$

The condition of $\tau = t$ means $\xi = 0$. Depending on the specific functions of the damping and nature frequency in time the differential solution of (136) which satisfy the temporal boundary conditions of (137)–(138) the appropriate $h(t, \tau)$ is provided and hence the polarizability $\alpha(\xi, t) = h(t, \tau) \Big|_{\tau=t-\xi}$.

It can be easily verified that the conditions of (137)–(138) deliver the well-known results for the stationary case, $d\gamma/dt = d\omega_n/dt = 0$ [78]:

$$\alpha(\xi, t) = h(t, t - \xi) = \frac{q_e^2 \exp\left[-\frac{\gamma}{2}\xi\right] \sin\left[\sqrt{\omega_n^2 - \frac{\gamma^2}{4}}\xi\right]}{m\sqrt{\omega_n^2 - \frac{\gamma^2}{4}}}. \quad (139)$$

^x $\frac{d}{dx} \int_{g_1(x)}^{g_2(x)} f(x, y) dy = f(x, g_2(x)) \frac{dg_2(x)}{dx} - f(x, g_1(x)) \frac{dg_1(x)}{dx} + \int_{g_1(x)}^{g_2(x)} \frac{\partial}{\partial x} f(x, y) dy.$

In a low-density medium the electrons interact weakly with each other, hence it is possible to assume a time-dependent density $N(t)$, which minimally effects the parameters of the motion of the electrons. In that case the polarization is:

$$\mathbf{P}(t) = N(t)\mathbf{p}(t) = \int_0^{+\infty} N(t)\alpha(\xi, t)\mathbf{E}(t - \xi)d\xi = \int_0^{+\infty} \varepsilon_0\chi(\xi, t)\mathbf{E}(t - \xi)d\xi, \quad (140)$$

where the electric susceptibility kernel is:

$$\chi(\xi, t) = \frac{N(t)q_e^2 \exp\left[-\frac{\gamma}{2}\xi\right] \sin\left[\sqrt{\omega_n^2 - \frac{\gamma^2}{4}}\xi\right]}{\varepsilon_0 m \sqrt{\omega_n^2 - \frac{\gamma^2}{4}}}, \quad (141)$$

and the relative permittivity of the medium is:

$$\varepsilon_r(\xi, t) = \delta(\xi) + \frac{N(t)q_e^2 \exp\left[-\frac{\gamma}{2}\xi\right] \sin\left[\sqrt{\omega_n^2 - \frac{\gamma^2}{4}}\xi\right]}{\varepsilon_0 m \sqrt{\omega_n^2 - \frac{\gamma^2}{4}}}, \quad (142)$$

where $\delta(\xi)$ is the delta function. Using the Fourier transform on the time variable ξ , the relative permittivity becomes:

$$\varepsilon_r(\omega, t) = 1 + \frac{\frac{q_e^2}{\varepsilon_0 m} N(t)}{\omega_n^2 - \omega^2 + j\gamma\omega}. \quad (143)$$

Assuming a free–electron plasma ($\omega_n = 0$) the results are identical to the expressions used for the effective permittivity of plasma with time–varying electron density [79].

In the case that the damping and the natural frequency are time–dependent the results change dramatically. To illustrate this an example is taken. If the nonstationary condition of the coefficients satisfies the equation:

$$\omega_n(t) = \frac{1}{2} \sqrt{\gamma^2(t) + 2 \frac{d\gamma(t)}{dt}}, \quad (144)$$

then:

$$h(t, \tau) = \frac{q_e^2}{m} (t - \tau) \exp \left[- \int \frac{\gamma(t)}{2} dt + \int \frac{\gamma(\tau)}{2} d\tau \right]. \quad (145)$$

For a free–electron model, $\omega_n = 0$, the damping coefficient is: $\gamma(t) = 2\gamma_0/(1 + \gamma_0 t)$ and $h(t, \tau) = (q_e^2/m)(t - \tau)(1 + \gamma_0 \tau)/(1 + \gamma_0 t)$. The polarizability kernel is thus:

$$\alpha(\xi, t) = \frac{q_e^2}{m} \xi \left[1 - \frac{\gamma_0 \xi}{1 + \gamma_0 t} \right], \quad (146)$$

and the relative permittivity is:

$$\varepsilon_r(\xi, t) = \delta(\xi) + \frac{N(t)q_e^2}{\varepsilon_0 m} \xi \left[1 - \frac{\gamma_0 \xi}{1 + \gamma_0 t} \right]. \quad (147)$$

The relative permittivity under the Fourier transform of the time-variable ξ is:

$$\varepsilon_r(\omega, t) = 1 - \frac{\frac{q_e^2}{\varepsilon_0 m} N(t)}{\omega^2} + j \frac{2 \frac{q_e^2}{\varepsilon_0 m} N(t) \gamma_0}{\omega^3 (1 + \gamma_0 t)}. \quad (148)$$

The temporal permittivity has an imaginary part which is time-dependent and is negative indicating that the medium is lossy. It is observed that the effective permittivity of the plasma with time-varying damping coefficient requires careful mathematical treatment and should not be treated in the same way as for the stationary case.

Appendix C:

Induced acoustic resonance by an active feedback control system

The basic experimental setup was explored and investigated to practically realize the theoretically examined physical concepts of the thesis in the acoustics regime. This experimental setup can actively control subwavelength acoustic resonator responses, via active electroacoustic elements and may be used as a fundamental building block for more complicated artificial resonating systems.

Acoustic resonators play a key role in the development of subwavelength-sized technologies capable of interacting with airborne audible sound, from emission and absorption, to manipulation and processing. Specifically, artificial acoustic media made from an ensemble of subwavelength resonators, namely acoustic metamaterials and metasurfaces, have enabled novel sound manipulation possibilities well beyond what is typically achievable using natural materials. Yet, the transition of such concepts from physics-driven explorations to practical applications has been drastically hindered by the major difficulty to control the resonance frequency, absorption level and bandwidth making acoustic metamaterials often too narrowband, or sensitive to disorder and absorption losses. In this subsection, the relevance of active electroacoustic resonators to address such limitations is demonstrated. This active mechanism is based on a feedback control scheme for loudspeakers, which involves passband current-control based on real-time sensing and processing of the pressure signal by FPGA technologies.

Specifically, we demonstrate a class of acoustic resonant scatterers with externally tunable resonance bandwidth and frequency and externally controlled absorption level. We use the transduction property of the electroacoustic resonators to implement an active feedback control based on a time–domain processing of the sensed pressure signal, reinjecting a passband current signal properly related to the sensed acoustic pressure, thus creating an acoustic resonance with controllable properties. We experimentally demonstrate our scheme in one–dimensional scenarios involving a loudspeaker used as a resonant acoustic scatterer and embedded in a cylindrical pipe supporting a single propagating mode.

The electrodynamic loudspeaker is an electroacoustic element, which is mechanically driven by a voice coil within a magnetic field. The acting forces are considerably small enough so that we can adopt a linear model for the sound pressure in front and back of the loudspeaker. It consists of three parts: the acoustic, the mechanical, and the electrical part. The equation in the frequency domain that describes the loudspeaker model is [80,81]

$$S_d = Z_{MS}u + Bli, \quad (149)$$

where S_d is the effective surface area of the loudspeaker, $\Delta p = p^+ - p^-$ is the pressure difference at the front and the back of the loudspeaker, u is the velocity, Bl is the force factor, i is the current flowing through the voice coil and $Z_{MS} = R_{MS} + j\omega M_{MS} + 1/(j\omega C_{MS})$ is the mechanical impedance which describes a spring–mass–damper system with mechanical resistance R_{MS} , mass M_{MS} and compliance C_{MS} , while the propagation at the tube of S_t cross section area is modelled via the transmission line model (see Table I).

TABLE I: Analogies between electromagnetic (EM) and acoustic transmission line parameters

EM model	Acoustic model
V (voltage)	p (pressure disturbance)
I (current)	Q (volume flux)
L (induction)	ρ_0/K_0 (spring effect)
C (capacitance)	S_t/K_0 (mechanical compliance)
$\sqrt{L/C}$ (characteristic impedance, Z_{char})	$\sqrt{\rho_0 K_0}/S_t$ (characteristic impedance, Z_{char})
$1/\sqrt{LC}$ (speed of EM signal, c)	$\sqrt{K_0/\rho_0}$ (speed of acoustic signal, c)

The two electroacoustic systems which are examined are the closed-box loudspeaker and the in-tube loudspeaker as shown in Fig. 27(a) and 27(b) respectively.

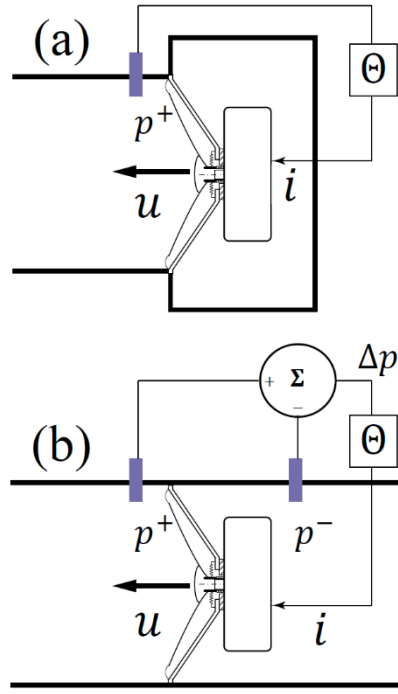


Figure 27: (a) A tube terminated by a closed-box loudspeaker, (b) a loudspeaker in the middle of the tube. Figure adapted from [70].

For the case of the closed-box loudspeaker, the closed-volume loading at the back allows the elimination of the variable p^- , by relating it to the membrane velocity u using the acoustic compliance $C_{ab} = v_b / (\rho_0 c^2)$, where v_b is the volume of the enclosure, ρ_0 is the density and c is the speed of sound. $p^- = S_d u / (j\omega C_{ab})$, eq. (104) becomes

$$S_d p^+ = \underbrace{\left(Z_{MS} + \frac{S_d^2}{j\omega C_{ab}} \right)}_{Z_{MCL}} u + Bli. \quad (150)$$

Both closed-box and in-tube models are of the form

$$S_d p = Z_M u + Bl i, \quad (151)$$

where p is p^+ for closed-box and Δp for in-tube systems and Z_M is Z_{MCL} for closed-box and Z_{MS} for in-tube systems. The control strategy relies on a feedback system that senses p and applies a control current $i = \Theta p$ as shown in Fig. 27, where Θ represents the transfer function of the controller. The quantity of interests which determines the resonant characteristics is the acoustic impedance of the loudspeaker: $Z_s = \frac{Z_M}{S_d^2} + \frac{Bl i}{u S_d^2}$. To enforce a resonance for a particular frequency, one has to enforce a real acoustic impedance Z_c to the electroacoustic element. Taking into account eq. (151), the control parameter takes the form: $\Theta = \frac{S_d}{Bl} (1 - \frac{Z_s}{Z_c})$. In Fig. 28, the block diagram is displayed for the loudspeaker under control.

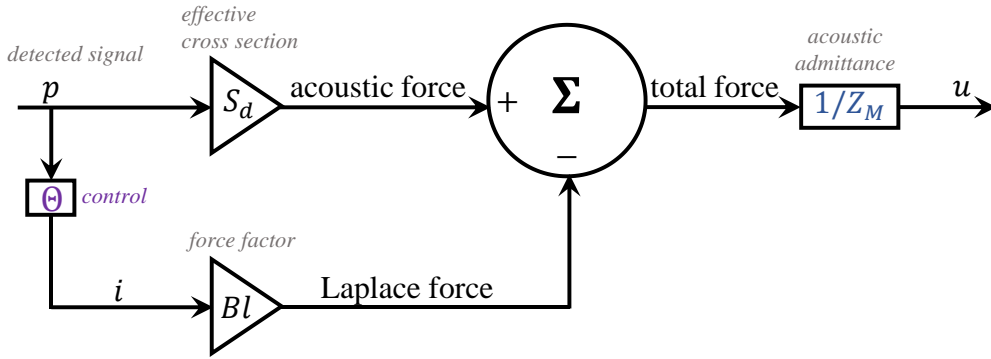


Figure 28: Block diagram of the electrodynamic loudspeaker model. As the pressure signal is detected, its value is multiplied by control parameter Θ and gives the right value of the current. The current is injected back in real time to the loudspeaker and alters the particle velocity, resulting in the manipulation of the lumped element impedance. Figure adapted from [70].

For the full control of the resonance one has to tailor the frequency content of $\Theta(\omega)$ at the resonant frequency f_0 and the neighbor frequencies (as long as causality permits it). A narrowband control allows for the assignment of a desired real value of the impedance at the resonance and tune the bandwidth. Since our objective is to control a small fraction of the frequency spectrum in real time, we design a reconfigurable band-pass system. To achieve this, one has to jump back and forth into time and frequency domain signal-processing techniques to implement a complex envelope control technique, as presented in Fig. 29. First, the pressure signal is detected $p(t)$, where $\mathcal{F}\{p(t)\} = P(\omega)$ [Fig. 29(a)]. Then the analytic signal $p_a(t) = p(t) + jp_h(t)$ is computed, where $p_h(t)$ is the Hilbert transform of $p(t)$ and $\mathcal{F}\{p_a(t)\} = P_a(\omega) = 2P(\omega)H(\omega)$, where $H(\omega)$ is the Heaviside distribution [Fig. 29(b)]. Working with the analytic signal is merely a trick to avoid dealing with the complex conjugate content of $P(\omega)$ at negative frequencies. A shift to target the central frequency f_0 is performed, $p'(t) = p_a(t)e^{j2\pi f_0 t}$, where it is clear that $\mathcal{F}\{p'(t)\} = P'(\omega) = P_a(\omega - 2\pi f_0)$ [Fig. 29(c)]. $p'(t)$ can be filtered by a low-pass filter $L(2\pi B)$. The choice of the low-pass filter and its bandwidth B determines the ultimate dispersion and bandwidth of the controlled resonance. We then multiply the signal by the constant value $\Theta(2\pi f_0)$, which corresponds to the demanded real impedance at f_0 . The resulting signal is $C(\omega) = \Theta(2\pi f_0)L(2\pi B)P_a(\omega - 2\pi f_0)$ [Fig. 29(d)]. After this analysis, it is straightforward to compute the required driving current by positively shifting back the signal by f_0 units [as shown in Fig. 29(e)] and finally extract the driving current as $i(t) = \text{Re}[\mathcal{F}^{-1}\{C(\omega)\}e^{-j2\pi f_0 t}]$.

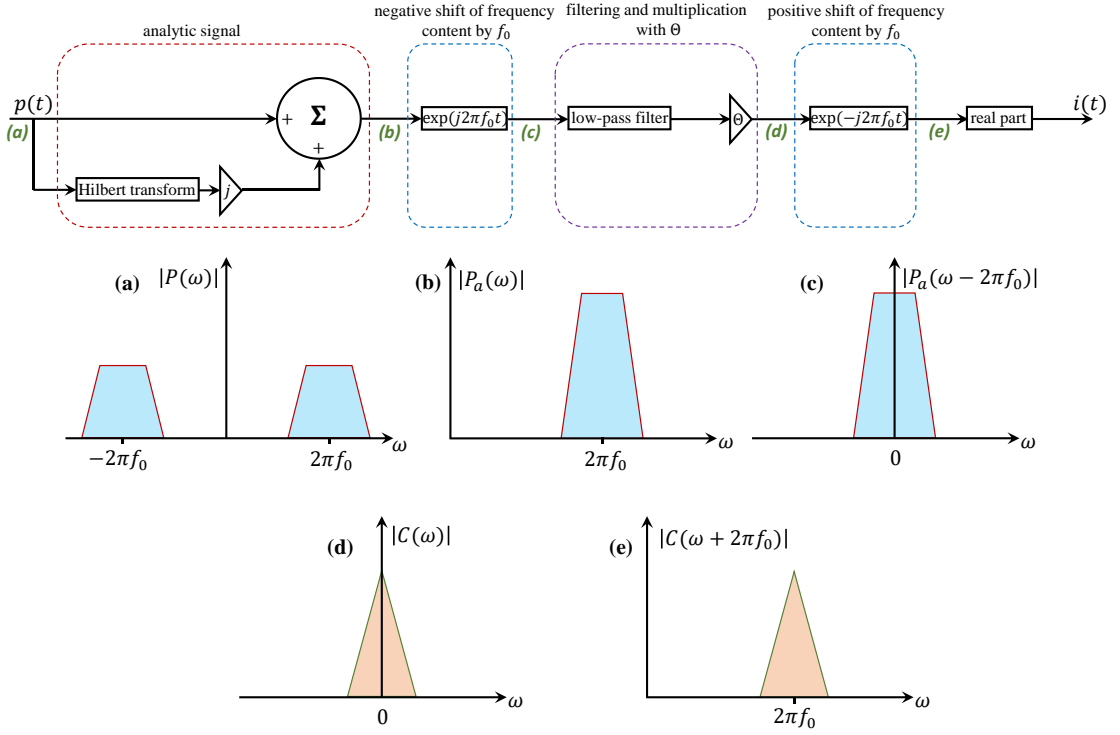


Figure 29: Block diagram of the acoustic pressure signal processed by the complex envelope technique and the corresponding frequency content of the signals under modulation: (a) frequency content of the pressure signal $p(t)$, (b) frequency content of the analytic signal $p_a(t)$, (c) negative frequency shift by the central frequency f_0 , (d) application of the low-pass filter and multiplication by the control parameter θ and (e) positive frequency shift by f_0 . Figure adapted from [70].

Next, the experimental results are explained and discussed from two representative cases: (a) a closed-box resonator and (b) an in-tube resonator. A low-pass Bessel filter of the second order is used to filter the shifted analytic pressure signal because it offers a reasonably flat and smooth area between the edges (other type of filters can be also used). The experimental setup consists of a power amplifier driving a source loudspeaker connected to a rigid tube, the controlled loudspeaker (either closed-box or in-tube), and a set of 130F20 microphones that are used to detect the pressure signals. The control system consists of a FPGA-based Speedgoat performance real-time target

machine with an IO131 interface (16-bit inputs) controlled by the xPC target environment of MATLAB and SIMULINK and a homemade analog voltage to current convertor with a transconductance equal to 21.3 mA/V.

To identify the system's characteristic parameters (Bl , Z_{MS} or Z_{MCL}), we first conduct three independent scattering measurements, for the loudspeaker to be controlled with three different electric loads plugged at its terminals. For the closed-box case, we use the standard two-microphone impedance measurement method. For the in-tube case, the impedance measurements require three simultaneous pressure measurements p_{ref} , p^+ and p^- . Hence, the formula for the impedance can be easily derived from the transmission line model: $Z = jZ_{char} \sin(kd)(p^+ - p^-)/[p_{ref} - \cos(kd)p^+]$, where d is the distance between p_{ref} and p^+ (assuming p_{ref} is closer to the source than p^+) and k is the wave number.

Based on the above sections and assuming polynomial fits for the unknown parameters, we derive a fit regarding the [120 Hz, 330 Hz] frequency range for the closed-box system and the [60 Hz, 230 Hz] frequency range for the in-tube system. The measured impedances and those calculated from the fitted parameters are seen in Fig. 30, thus demonstrating excellent agreement between measurements and our linear model.

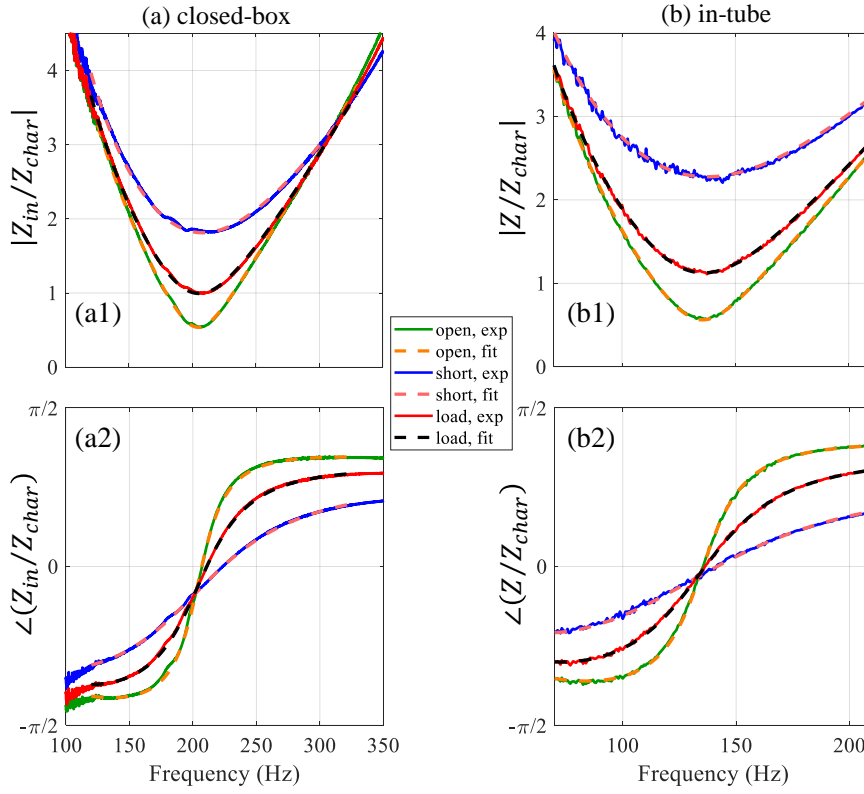


Figure 30: Graphical plots for (a) closed-box and (b) in-tube systems under examination. (a1), (b1) show the amplitude and (a2), (b2) the phase of the normalized impedances for three independent cases: open circuit, short circuit and load. Solid lines, measured data; dashed lines, results of fitting model. Figure adapted from [70].

We start with a first set of experiments in which we demonstrate the possibility of controlling the resonance central frequency of such systems, i.e., control of the resonance frequency for a fixed bandwidth and real value of impedance at resonance. More precisely, in the case of the closed-box system, we fix the target impedance to $Z_{in}/Z_{char} = 0.1$, where Z_{in} is the input impedance of the loudspeaker and Z_{char} is the characteristic impedance. We target a low-loss resonator with a low residual acoustic resistance at resonance of 10% of the tube impedance. The edge frequency of the Bessel filter is set to $B = 10\text{Hz}$, and we set the control to vary the value of the central frequency f_0 . Notably, once these parameters are enforced to the system by the

controller, the acoustic resonator is probed using microphones connected to a data acquisition system that is independent from the FPGA, while looks from the outside just like a normal passive mechanical acoustic resonator. In Fig. 31(a), we show the measured acoustic impedance for five independent experiments, each time with a central frequency of different value, namely, 200, 205, 210, 215, and 220 Hz. Evidently, the control mechanism provides the expected results, which can be seen clearly in Fig. 31(a2). The phase of the acoustic impedances crosses zero at the externally determined frequencies, while the measured impedance is at the targeted ratio and the bandwidth does not change. This corresponds to a system with almost unitary reflection, i.e., almost no absorption, at resonance. The measurements for the in-tube system are seen in Fig. 31(b). This time, we fix the target real impedance at $Z/Z_{char} = 0.15$, where Z is the impedance of the in-tube loudspeaker and the edge frequency at $B = 5\text{Hz}$. We exhibit five independent experiments similarly with the closed-box system, where the central frequency takes the values 120, 125, 130, 135, and 140 Hz. Again, the measurements agree with the expected results of the control mechanism in terms of the target real impedance value and constant bandwidth [Fig. 31(b1)] and the location of the resonance frequencies [Fig. 31(b2)]. In terms of the scattering, the total reflection, absorption, and transmission of this element depend also on the tube termination. For instance, in the case of an anechoic termination, this in-tube element would have a reflection coefficient of about 0.115 at resonance. Notably, also, since the loudspeaker is deeply subwavelength, its reflection is symmetric, despite its asymmetric geometry, and the control strategy works regardless of the wave direction.

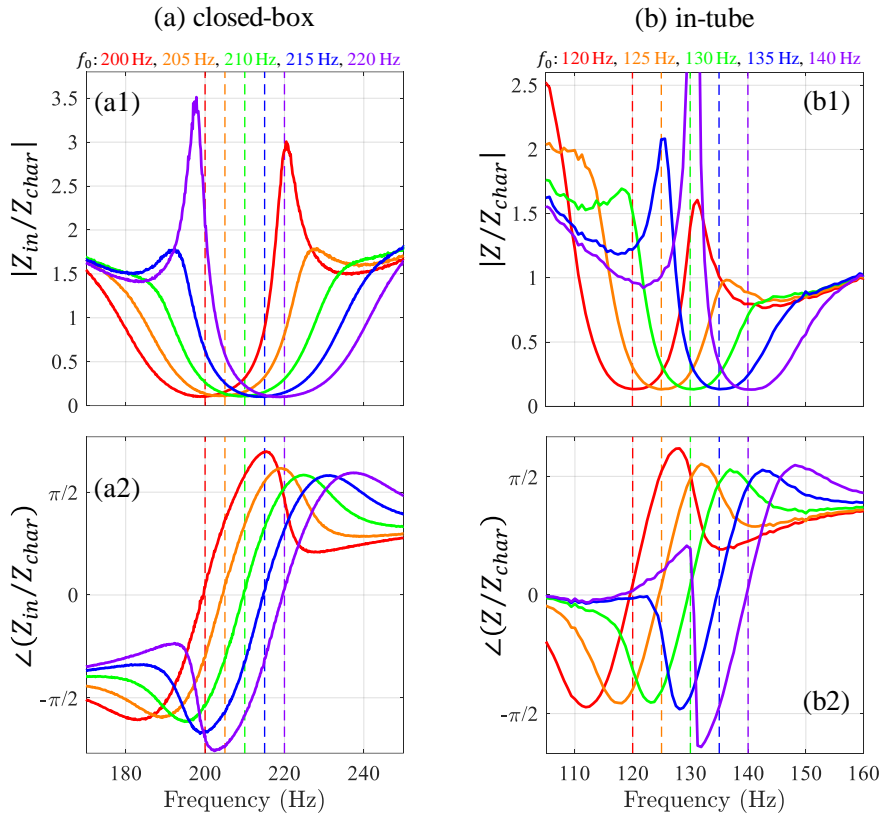


Figure 31: Measured (a) closed-box and (b) in-tube electrodynamic loudspeaker impedance. For the closed-box system, the central frequency f_0 is shifted from 200 to 220 Hz with $B = 10$ Hz and $Z_{in}/Z_{char} = 0.1$. For the in-tube system, the central frequency f_0 is shifted from 120 to 140 Hz with $B = 5$ Hz and $Z/Z_{char} = 0.15$. (a1), (b1) are graphic presentations of the amplitude and (a2), (b2) of the phase of the acoustic impedance. Figure adapted from [70].

The bandwidth of the resonators can be controlled by tuning the edge of the Bessel filter (Fig. 32) at a fixed resonance frequency and real resonant target impedance. In Fig. 32(a), the measurements of the closed-box system are shown, while Fig. 32(b) reports those of the in-tube configuration. The measurements confirm that by changing the edge frequency of the filter we can easily control the bandwidth of the resonance. As expected, while the bandwidth opens, the slope of the phase of the impedance decreases, although it always crosses zero at the frequency of resonance f_0 .

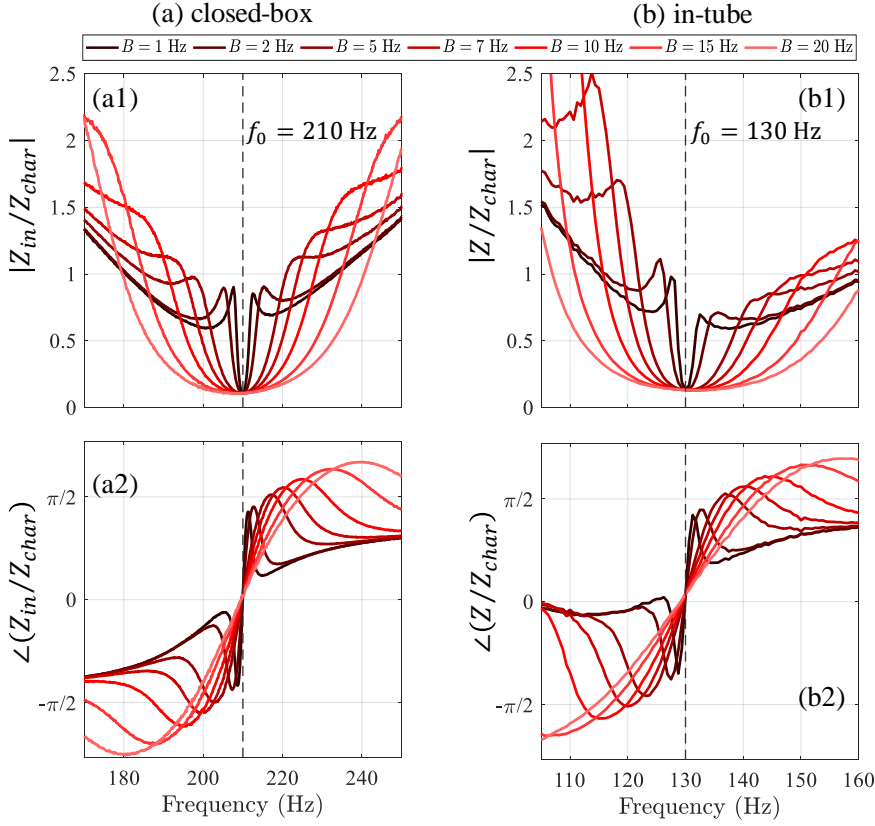


Figure 32: Measured (a) closed-box and (b) in-tube electrodynamic loudspeaker impedance, where the edge frequency of the Bessel filter B is shifted from 1 to 20 Hz. For the case of the closed-box system: $f_0 = 210$ Hz (dashed line) and $Z_{in}/Z_{char} = 0.1$. For the case of the in-tube system: $f_0 = 130$ Hz (dashed line) and $Z/Z_{char} = 0.15$. (a1), (b1) are graphic presentations of the amplitude and (a2), (b2) of the phase of the acoustic impedance. Figure adapted from [70].

In Fig. 33, we show the last possibility, namely, control of the targeted real impedance for a scenario of fixed central frequency and edge-filter frequency. The measurements show a wide range of achievable targets for the impedances, from values higher than the impedance of the tube all the way down to near zero. As the targeted impedances gradually increase, the slope of the phase of the impedances changes sign above a threshold value (above the

physical acoustic impedance at the selected central frequency). Interestingly, the ability to target very low values corresponds to the possibility of creating resonators with almost no residual absorption at resonance, which is key in the development of applications of locally resonant metamaterials.

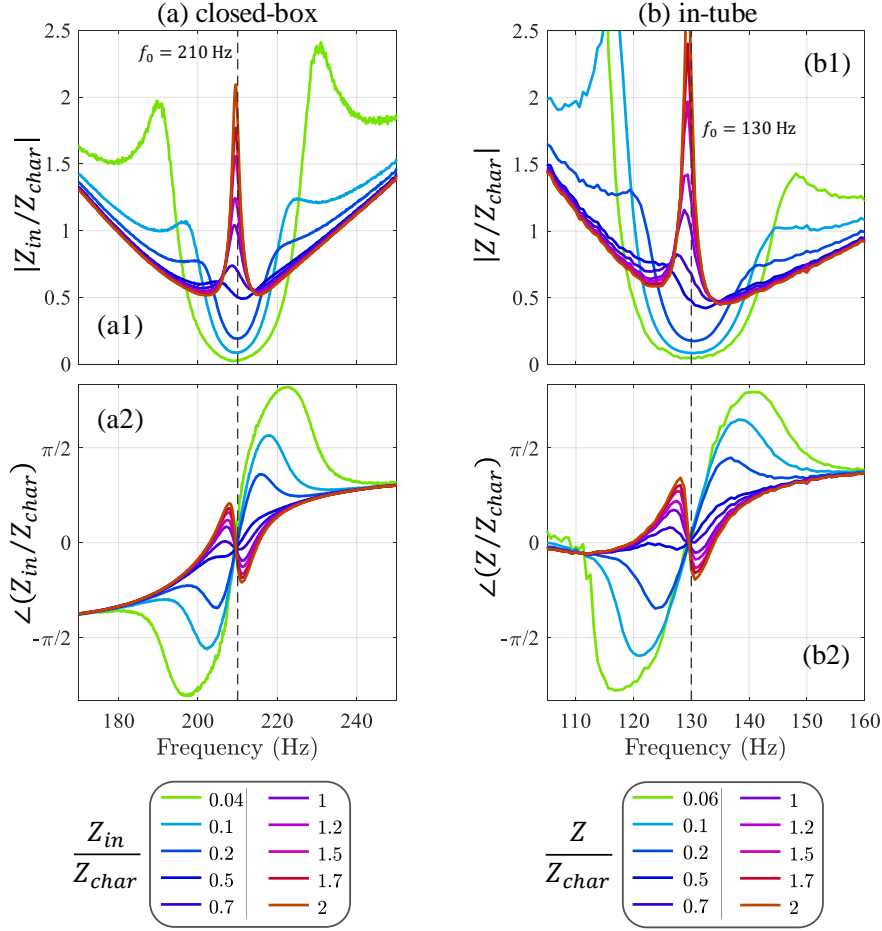


Figure 33: Measured (a) closed-box and (b) in-tube electrodynamic loudspeaker impedance. For the case of the closed-box system: $f_0 = 210$ Hz (dashed line) and Z_{in}/Z_{char} is shifted from 0.04 to 2 with $B = 5$ Hz. For the case of the in-tube system: $f_0 = 130$ Hz (dashed line) and Z/Z_{char} is shifted from 0.06 to 2 with $B = 5$ Hz. (a1), (b1) are graphic presentations of the amplitude and (a2), (b2) of the phase of the acoustic impedance. Figure adapted from [70].

The presented technique and the possibility to reconfigure the resonant responds of electroacoustic elements with this method could enlarge the toolbox of acoustic engineers and applied physicists, not only by building low-loss acoustic metamaterials out of active resonators with calibrated robust resonance frequencies and programmable bandwidth, but also by helping construct a new generation of dynamic acoustic systems, such as fast switches or time-modulated artificial structures with novel physical properties.

Nevertheless, this systematic approach has limitations. The first limit of the approach comes from our approximate knowledge of the system, which is modeled with a linear transfer function. Since this model can only approximate reality (especially due to the presence of nonlinearities), our control strategy has a certain margin of error. This becomes an issue when one wants to assign a value of impedance that is very different from that of the natural impedance of the uncontrolled loudspeaker because the feedback gain depends directly on their ratio. In practice, we note the need to refine our model when this ratio exceeds a factor of 10. The linear model is also expected to fail at high intensities, due to nonlinear phenomena that are not being accounted for. A more practical limitation of the method comes from the delay time of the FPGA, which sets a limit on the maximum operating frequency (around 10 kHz in our case). The 16-bit FPGA inputs also cause problems with very low intensities because they limit the signal-to-noise ratio. Finally, stability generally limits the maximum resonator bandwidth (bandwidth is a measure of the decay rate of the resonance, which is limited by what the scattering environment can provide).

Notably, here, we have not targeted negative values of acoustic resistances (which would correspond to gain) because the experimental system, which only contains a single resonator, would become automatically unstable. However, in more complex systems with a less stringent stability condition, the method has been employed to induce acoustic gain [82]. We can thus envision that our

strategy can be utilized to bridge the theoretical investigations of synthetic acoustic media and non-Hermitian sound-wave structures with pragmatic implementations.

Additionally, this active technique may be used to control the resonance properties of an acoustic device that may be subject to a modulation of its capacitive or inductive elements, setting the foundations for practical wave control in acoustics via time-modulations.

References

- [1] W. C. Chew, *Waves and Fields in Inhomogeneous Media* (Wiley-IEEE Press, NJ, USA, 1995).
- [2] M. Born and E. Wolf, *Principles of Optics: Electromagnetic Theory of Propagation, Interference and Diffraction of Light* (Cambridge University Press, 1999).
- [3] C. M. Bender and S. Boettcher, Phys. Rev. Lett. **80**, 5243 (1998).
- [4] R. El-Ganainy, K. G. Makris, M. Khajavikhan, Z. H. Musslimani, S. Rotter, and D. N. Christodoulides, Nat. Phys. **14**, 11 (2018).
- [5] C. M. Bender, P. E. Dorey, C. Dunning, A. Fring, D. W. Hook, H. F. Jones, S. Kuzhel, G. Lévai, and R. Tateo, *PT Symmetry* (World Scientific, London, 2019).
- [6] R. Fleury, D. L. Sounas, and A. Alù, Nat. Commun. **6**, 5905 (2015).
- [7] P. Y. Chen, M. Sakhdari, M. Hajizadegan, Q. Cui, M. M. C. Cheng, R. El-Ganainy, and A. Alù, Nat. Electron. **1**, 297 (2018).
- [8] H. Hodaei, M. A. Miri, M. Heinrich, D. N. Christodoulides, and M. Khajavikhan, Science (80-.). **346**, 975 (2014).
- [9] B. Qi, H. Chen, L. Ge, P. Berini, and R. Ma, Adv. Opt. Mater. **7**, 1900694 (2019).
- [10] J. R. Zurita-Sánchez, P. Halevi, and J. C. Cervantes-González, Phys. Rev. A **79**, 053821 (2009).
- [11] H. Qu, Z.-L. Deck-Léger, C. Caloz, and M. Skorobogatiy, J. Opt. Soc. Am. B **33**, 1616 (2016).
- [12] N. Engheta, Nanophotonics **10**, 639 (2021).
- [13] V. Pacheco-Peña and N. Engheta, Light Sci. Appl. **9**, 2047 (2020).
- [14] E. Galiffi, P. A. Huidobro, and J. B. Pendry, Phys. Rev. Lett. **123**, 206101 (2019).
- [15] E. Galiffi, Y. T. Wang, Z. Lim, J. B. Pendry, A. Alù, and P. A. Huidobro, Phys. Rev. Lett. **125**, 127403 (2020).
- [16] F. R. Morgenthaler, IRE Trans. Microw. Theory Tech. **6**, 167 (1958).
- [17] T. T. Koutserimpas and R. Fleury, IEEE Trans. Antennas Propag. **68**, 6717 (2020).
- [18] T. T. Koutserimpas and R. Fleury, IEEE Trans. Antennas Propag. **66**, 5300 (2018).

- [19] T. T. Koutserimpas, A. Alù, and R. Fleury, *Phys. Rev. A* **97**, 013839 (2018).
- [20] T. T. Koutserimpas and R. Fleury, *Wave Motion* **89**, 221 (2019).
- [21] T. T. Koutserimpas and R. Fleury, *J. Appl. Phys.* **123**, 091709 (2018).
- [22] T. T. Koutserimpas and R. Fleury, *Phys. Rev. Lett.* **120**, 087401 (2018).
- [23] N. V. Budko, *Phys. Rev. A* **80**, 053817 (2009).
- [24] J. S. Martínez-Romero, O. M. Becerra-Fuentes, and P. Halevi, *Phys. Rev. A* **93**, 063813 (2016).
- [25] Y. Xiao, D. N. Maywar, and G. P. Agrawal, *Opt. Lett.* **39**, 574 (2014).
- [26] J. A. Kong, *Electromagnetic Wave Theory* (Wiley, 1986).
- [27] D. Stefanatos, H. Schaettler, and J. S. Li, *SIAM J. Control Optim.* **49**, 2440 (2011).
- [28] R. Spigler and M. Vianello, in *Adv. Differ. Equations Proc. Second Int. Conf. Differ. Equations Veszprém, Hungary, August 7-11, 1995*, edited by S. Elaydi, I. Györi, and G. E. Ladas (Gordon and Breach Science Publishers, 1997), pp. 567–577.
- [29] S. L. Hahn and K. M. Snopek, *Complex and Hypercomplex Analytic Signals: Theory and Applications* (Artech House, 2017).
- [30] Kittel Charles, *Introduction to Solid State Physics* (Wiley, 1992).
- [31] P. Yeh, A. Yariv, and C.-S. Hong, *J. Opt. Soc. Am.* **67**, 423 (1977).
- [32] A. Yariv and P. Yeh, *J. Opt. Soc. Am.* **67**, 438 (1977).
- [33] L. Brillouin, *Wave Propagation in Periodic Structures: Electric Filters and Crystal Lattices*. (Dover Publications, 1953).
- [34] W. Magnus and S. Winkler, *Hill's Equation* (Dover Publications, 1966).
- [35] C. E. Rüter, K. G. Makris, R. El-Ganainy, D. N. Christodoulides, M. Segev, and D. Kip, *Nat. Phys.* **6**, 192 (2010).
- [36] J. D. Joannopoulos, S. G. Johnson, J. N. Winn, and R. D. Meade, *Photonic Crystals: Molding the Flow of Light*, 2nd ed. (Princeton University Press, 2008).
- [37] G. N. Henderson, T. K. Gaylord, and E. N. Glytsis, *Phys. Rev. B* **45**, 8404 (1992).
- [38] Y. D. Chong, L. Ge, and A. D. Stone, *Phys. Rev. Lett.* **106**, 093902 (2011).
- [39] R. J. Potton, *Reports Prog. Phys.* **67**, 717 (2004).

- [40] H. Schomerus, Phys. Rev. Lett. **104**, 233601 (2010).
- [41] W. D. Heiss, J. Phys. A Math. Theor. **45**, 444016 (2012).
- [42] D. E. Holberg and K. S. Kunz, IEEE Trans. Antennas Propag. **14**, 183 (1966).
- [43] N. W. McLachlan, *Theory and Application of Mathieu Functions* (Oxford University Press, London, 1951).
- [44] S. Longhi, Phys. Rev. A **82**, 031801 (2010).
- [45] L. Ge, Y. D. Chong, and A. D. Stone, Phys. Rev. A **85**, 023802 (2012).
- [46] S. Longhi, Phys. Rev. Lett. **107**, 033901 (2011).
- [47] G. Mur, IEEE Trans. Electromagn. Compat. **EMC-23**, 377 (1981).
- [48] A. Taflove and S. C. Hagness, *Computational Electrodynamics* (Artech House, 2005).
- [49] H. Sambe, Phys. Rev. A **7**, 2203 (1973).
- [50] V. Grigoriev and F. Biancalana, J. Opt. Soc. Am. B **28**, 2165 (2011).
- [51] J. von Neumann, *Mathematical Foundations of Quantum Mechanics* (Princeton University Press, 1955).
- [52] N. Engheta, Science (80-.). **340**, 286 (2013).
- [53] I. Liberal and N. Engheta, Proc. Natl. Acad. Sci. U. S. A. **114**, 822 (2017).
- [54] M. Silveirinha and N. Engheta, Phys. Rev. Lett. **97**, 157403 (2006).
- [55] A. Alù, M. G. Silveirinha, A. Salandrino, and N. Engheta, Phys. Rev. B **75**, 155410 (2007).
- [56] B. Edwards, A. Alù, M. G. Silveirinha, and N. Engheta, J. Appl. Phys. **105**, 044905 (2009).
- [57] X. Huang, Y. Lai, Z. H. Hang, H. Zheng, and C. T. Chan, Nat. Mater. **10**, 582 (2011).
- [58] K. Sakoda, Opt. Express **20**, 3898 (2012).
- [59] K. Sakoda, Opt. Express **20**, 9925 (2012).
- [60] K. Sakoda, J. Opt. Soc. Am. B **29**, 2770 (2012).
- [61] Z. Wang, F. Yang, L. Liu, M. Kang, and F. Liu, J. Appl. Phys. **114**, (2013).
- [62] M. Dubois, C. Shi, X. Zhu, Y. Wang, and X. Zhang, Nat. Commun. **8**, 14871 (2017).

- [63] S. Y. Yu, Q. Wang, L. Y. Zheng, C. He, X. P. Liu, M. H. Lu, and Y. F. Chen, Appl. Phys. Lett. **106**, 151906 (2015).
- [64] Y. Li, Y. Wu, and J. Mei, Appl. Phys. Lett. **105**, 014107 (2014).
- [65] F. Liu, X. Huang, and C. T. Chan, Appl. Phys. Lett. **100**, 071911 (2012).
- [66] R. Liu, Q. Cheng, T. Hand, J. J. Mock, T. J. Cui, S. A. Cummer, and D. R. Smith, Phys. Rev. Lett. **100**, (2008).
- [67] H. Dai, T. Liu, J. Jiao, B. Xia, and D. Yu, J. Appl. Phys. **121**, 135105 (2017).
- [68] R. Fleury, A. B. Khanikaev, and A. Alù, Nat. Commun. **7**, 11744 (2016).
- [69] R. Fleury, D. L. Sounas, and A. Alù, Phys. Rev. B **91**, 174306 (2015).
- [70] T. T. Koutserimpas, E. Rivet, H. Lissek, and R. Fleury, Phys. Rev. Appl. **12**, 054064 (2019).
- [71] X. X. Liu, D. A. Powell, and A. Alù, Phys. Rev. B **84**, 235106 (2011).
- [72] X. Chen, T. M. Grzegorzczuk, B. I. Wu, J. Pacheco, and J. A. Kong, Phys. Rev. E **70**, 016608 (2004).
- [73] M. S. Mirmoosa, T. T. Koutserimpas, G. A. Ptitsyn, S. A. Tretyakov, and R. Fleury, ArXiv:2002.12297 (2020).
- [74] N. Wang, Z. Q. Zhang, and C. T. Chan, Phys. Rev. B **98**, 085142 (2018).
- [75] A. Hessel and A. A. Oliner, IRE Trans. Microw. Theory Tech. **9**, 337 (1961).
- [76] P. A. Huidobro, E. Galiffi, S. Guenneau, R. V. Craster, and J. B. Pendry, Proc. Natl. Acad. Sci. **116**, 24943 (2019).
- [77] L. D. Landau and E. M. Lifshitz, *Electrodynamics of Continuous Media*, 2nd ed. (Pergamon Press, 1984).
- [78] J. D. Jackson, *Classical Electrodynamics* (Wiley, 1999).
- [79] S. G. Ohler, B. E. Gilchrist, and A. D. Gallimore, IEEE Trans. Plasma Sci. **27**, 587 (1999).
- [80] H. Lissek, R. Boulandet, and R. Fleury, J. Acoust. Soc. Am. **129**, 2968 (2011).
- [81] E. Rivet, S. Karkar, and H. Lissek, IEEE Trans. Control Syst. Technol. **25**, 63 (2017).
- [82] E. Rivet, A. Brandstötter, K. G. Makris, H. Lissek, S. Rotter, and R. Fleury, Nat. Phys. **14**, 942 (2018).
- [83] H. Li, T. Kottos, and B. Shapiro, Phys. Rev. Appl. **9**, 044031 (2018).

[84] N. S. Stepanov, Radiophys. Quantum Electron. **19**, 683 (1976).

Theodoros T. Koutserimpas CV

Institute of Electrical Engineering, Swiss Federal Institute of Technology Lausanne (EPFL), Lausanne 1015, Switzerland.
EPFL STI IEL LWE ELB 032, Station 11, Lausanne 1015, Switzerland.

email: theodoros.koutserimpas@epfl.ch

google scholar profile: https://scholar.google.ch/citations?user=G-_kXZ8AAAAJ&hl=en

OrcID: <https://orcid.org/0000-0003-1288-781X>

Education

- **Ph.D.** in Electrical Engineering, Swiss Federal Institute of Technology Lausanne (EPFL), 2021.
Ph.D. Thesis: Electromagnetic waves under nonstationary conditions, the connection with parity-time symmetry and studies on resonant systems (advisor Prof. Romain Fleury).
- **Diploma** in Electrical and Computer Engineering, National Technical University of Athens (NTUA), 2017.
Diploma Thesis: The solution of Maxwell's equations in the frequency domain and the applicability of the Alternating-Direction-Implicit iterative method (advisor Prof. E. N. Glytsis).

Research Interests

Electromagnetic theory, computational electromagnetics, microwaves, optics, acoustics, applied quantum mechanics, numerical and analytical methods dealing with wave phenomena.

Research Experience

- **Ph.D. Student, Swiss Federal Institute of Technology Lausanne (01/11/2017 – 2021)**, under supervision of Prof. Romain Fleury.
- **Research Intern, Swiss Federal Institute of Technology Lausanne (01/05/2017 – 31/10/2017)**, under supervision of Prof. Romain Fleury.
- **Undergraduate Research Assistant, National Technical University of Athens (2016 – 2017)**, under supervision of Prof. Elias N. Glytsis.

Teaching Experience

Graduate Teaching Assistant (EPFL):

- General Physics: Mechanics (Fall 2018-2019).
- Electromagnetics I: Transmission lines and waves (Fall 2019-2020, 2020-2021).
- Science and Technologies of Electricity (Fall 2019-2020).
- Electromagnetics II: Calculation of Fields (Spring 2019-2020, 2020-2021).

Co-advisor of Master Thesis at EPFL:

- Maxime Volery, "Numerical Analysis of Time-Floquet Devices," (2018).

Undergraduate Teaching Assistant (NTUA, 2016 – 2017): I was involved in teaching to peers fundamental concepts of electromagnetism and solving electromagnetic problems at the exercise sessions of the electromagnetic fields courses. (Reference: Prof. Elias N. Glytsis).

Participation in Funded Projects

- Swiss National Science Foundation (SNSF) Grant N° 172487: Nonreciprocal metamaterials for a new degree of wave control.

Publications

- [10] M. S. Mirmoosa, **T. T. Koutserimpas**, G. A. Ptitsyn, S. A. Tretyakov and R. Fleury, “Dipole polarizability of time-varying particles,” *ArXiv:2002.12297* (2020).
- [9] **T. T. Koutserimpas** and R. Fleury, “Electromagnetic Fields in a Time-Varying Medium: Exceptional Points and Operator Symmetries,” *IEEE Trans. Antennas Propag.*, vol. 68, no. 9, pp. 6717–6724, Sept. 2020.
- [8] **T. T. Koutserimpas**, E. Rivet, H. Lissek and R. Fleury, “Active Acoustic Resonators with Reconfigurable Resonance Frequency, Absorption, and Bandwidth,” *Phys. Rev. Appl.*, vol. 12, no. 5, p. 054064, Nov. 2019.
- [7] **T. T. Koutserimpas** and R. Fleury, “Coupled-mode theory for stationary and nonstationary resonant sound propagation,” *Wave Motion*, vol. 89, pp. 221–231, Jun. 2019.
- [6] **T. T. Koutserimpas** and R. Fleury, “Electromagnetic Waves in a Time Periodic Medium With Step-Varying Refractive Index,” *IEEE Trans. Antennas Propag.*, vol. 66, no. 10, pp. 5300–5307, Oct. 2018.
- [5] E. N. Glytsis, A. D. Papadopoulos and **T. T. Koutserimpas**, “Review and accuracy comparison of various permittivity-averaging schemes for material discontinuities in the two-dimensional FDFD method: implementation using efficient computer graphics techniques,” *Appl. Opt.*, vol. 57, no. 25, pp. 7303–7313, Sep. 2018.
- [4] **T. T. Koutserimpas** and R. Fleury, “Zero refractive index in time-Floquet acoustic metamaterials,” *J. Appl. Phys.*, vol. 123, no. 9, p. 091709, Mar. 2018.
- [3] **T. T. Koutserimpas** and R. Fleury, “Nonreciprocal Gain in Non-Hermitian Time-Floquet Systems,” *Phys. Rev. Lett.*, vol. 120, no. 8, p. 087401, Feb. 2018.
- [2] **T. T. Koutserimpas**, A. Alù and R. Fleury, “Parametric amplification and bidirectional invisibility in \mathcal{PT} -symmetric time-Floquet systems,” *Phys. Rev. A*, vol. 97, no. 1, p. 013839, Jan. 2018. **[PRA Editors have selected this paper as Editors’ Suggestion].**
- [1] **T. T. Koutserimpas**, A. D. Papadopoulos and E. N. Glytsis, “Applicability and Optimization of the Alternating-Direction-Implicit Iterative Method for the 2-D Finite-Difference Frequency-Domain Solution of Scattering Problems,” *IEEE Trans. Antennas Propag.*, vol. 65, no. 12, pp. 7166–7173, Dec. 2017.

Conference Presentations

- [2] S. M. Mirmoosa, **T. T. Koutserimpas**, G. A. Ptitsyn, S. A. Tretyakov, and R. Fleury, “From Polarizability to Effective Permittivity of Time-Varying Materials,” *Metamaterials 2020, the 14th International Congress on Artificial Materials for Novel Wave Phenomena*, New York, USA, Sept. 28–Oct. 3, 2020 **(invited talk)**.
- [1] **T. T. Koutserimpas**, and R. Fleury, “Extraordinary wave dynamics in time-Floquet acoustic systems,” *META 2018, the 9th International Conference on Metamaterials, Photonic Crystals and Plasmonics*, Round-Trip Marseille Cruise, June 24–July 1, 2018 **(invited talk)**.